The Evolution and Nucleosynthesis of Thermally Pulsing Asymptotic Giant Branch Stars

Richard James Stancliffe
Churchill College

Institute of Astronomy
University of Cambridge

Thesis submitted for the Degree of Doctor of Philosophy at the University of Cambridge

· 2005 ·

Declaration

I hereby declare that my thesis entitled *The Evolution and Nucleosynthesis of Thermally Pulsing Asymptotic Giant Branch Stars* is not substantially the same as any that I have submitted for a degree or diploma or other qualification at any other University. I further state that no part of my thesis has already been or is being concurrently submitted for any such degree, diploma or other qualification. This dissertation is the result of my own work and includes nothing which is the outcome of work done in collaboration except where specifically indicated in the text. Those parts of this thesis which have been published or accepted for publication are as follows:

- Material from chapters 2 and 3 has been published as:
  Stancliffe R. J., Tout C. A., Pols O. R., 2004, "Deep dredge-up in intermediate-mass thermally pulsing asymptotic giant branch stars", *Monthly Notices of the Royal Astronomical Society*, **352**, 984-992 and was completed in collaboration with these authors.

- Material from chapter 4 has been published as:
  Stancliffe R. J., Izzard R. G., Tout C. A., 2005, "Third dredge-up in low-mass: solving the Large Magellanic Cloud carbon star mystery", *Monthly Notices of the Royal Astronomical Society*, **356**, L1-L5 and was completed in collaboration with these authors.

- Material from chapter 5 has been published as:
  Stancliffe R. J., Lugaro M. A., Ugalde C., Tout C. A., Görres J., Wiescher M., 2005, "The effect of the $^{19}\mathrm{F}(\alpha,\mathrm{p})^{22}\mathrm{Ne}$ reaction rate uncertainty on the yield of fluorine from Wolf-Rayet stars", *Monthly Notices of the Royal Astronomical Society*, **360**, 375-379 and was completed in collaboration with these authors.

This thesis contains fewer than 60,000 words.

R. J. Stancliffe
Cambridge, October 23, 2005

Abstract

The thermally pulsing asymptotic giant branch (TP-AGB) is a computationally demanding phase of evolution. This work presents a set of models that have been computed fully simultaneously – i.e. by solving the equations of stellar structure, nuclear burning and mixing together for each iteration of each timestep. It details the development of a viscous mesh technique in order to deal with some of the numerical problems that occur during the TP-AGB.

Models have been created at solar metallicity ($Z = 0.02$) and metallicities appropriate to the Large and Small Magellanic Clouds ($Z = 0.008$ and $Z = 0.004$). These are evolved without mass loss. The solar metallicity models display important differences from those computed using other codes including deeper third dredge-up. The Large and Small Magellanic Cloud models are used to investigate the problem of the carbon star luminosity function.

TP-AGB stars are also important sites for stellar nucleosynthesis. In order to investigate nucleosynthesis on the TP-AGB a set of subroutines have been developed to track the evolution of isotopes from deuterium to sulphur plus important iron group elements. These have been used to calculate the evolution of minor isotopes in TP-AGB stars of 1.5, 3 and $5\,\mathrm{M}_\odot$ at metallicities of $Z = 0.02,\ 0.008$ and 0.004 evolved with mass loss. The results of these calculations are compared to known constraints from spectroscopic observations and measurements of pre-solar grains.

At the end of the TP-AGB the star makes the transition to a white dwarf. In the course of trying to calculate this evolution it was found that numerical diffusion could substantially affect the evolution and that this phase has to be treated with great care.

Contents

List of Figures

List of Tables

Acknowledgments

This work would not have been possible without the help and support of many people. I would like to take this opportunity to offer my thanks.

First and foremost I would like to thank Chris for supervising me through the past three year. I have learnt much from him in this time, from the details of stellar evolution through the differences between decanters for port and claret to the intricacies of English grammar (though I'm still struggling with the latter, apparently). I may not have been the model student but Chris has been the ideal supervisor. He has been there when I have needed him and yet has given me the space that I needed in order to become (I hope!) a confident, independent researcher. I am indebted to him for his support in my securing a junior research fellowship at Churchill College.

Thanks also to all those that I have had the pleasure and privilege to work with, both here at the IoA and further afield. Without Maria the nucleosynthesis work would have taken much, much longer and probably contain many more bugs. I thank Pierre for the many conversations that have resulted in increased numerical and mental stability. I also thank Rob for teaching me about the joys of Perl. Last, but by no means least, I would like to thank Ross for many useful discussions and for taking on the unenviable task of proof-reading this work. Of my external collaborators, I thank Onno for guidance and inviting me to Utrecht. The Dutch Ph.D. defense is an interesting affair. I also thank Amanda for inviting me to Halifax, helping to undertake the awkward task of doing a code comparison and more importantly, for obtaining Mooseheads tickets.

The IoA would not have been the same without the following: Justyn – my lunchtime companion for the last three years, the denizens of H29 – too many to mention by name and of course, Muon and Klio who have given me a legitimate reason for being at work at weekends.

And finally I will end on a personal note. I would like to thank my parents for their support over the course of my life. Without them, I would never have reached the point that I now find myself at. Last, but by no means least, thanks also to Kristen for her love and encouragement, as well as teaching me how to scull.

R. J. Stancliffe
Cambridge, October 23, 2005

Chapter 1

Introduction

The asymptotic giant branch (AGB) is a fascinating and complex phase of stellar evolution that some stars pass through towards the end of their lives. An unstable arrangement of two thin burning shells, one of helium and one of hydrogen, leads to interesting periodic behaviour and rich nucleosynthesis, making these objects a valuable area of study.

1.1 Stellar Evolution

This work is concerned with stars of between 1 and $8\,M_\odot$. Low-mass stars shall be defined as those stars less massive than $4\,M_\odot$ while those of between 4 and $8\,M_\odot$ will be refered to as intermediate-mass stars. The definition is somewhat arbitrary but is convenient and has been chosen so that intermediate-mass stars undergo hot-bottom burning (see below, section 1.2.2) whilst they are on the thermally pulsing asymptotic giant branch; low-mass stars do not experience this process.

1.1.1 The Main-sequence

Stars form out of clouds of gas in a process that is not well understood. These clouds of gas are about three-quarters hydrogen and one-quarter helium along with smaller quantities of carbon, nitrogen, oxygen and heavier elements. From the point of view of stellar evolution, we may begin our studies from what is referred to as the pre-main sequence. Here we envisage a cloud of gas that has already begun to collapse under its own gravity, but is not hot

enough for nuclear reactions to take place. As the cloud of gas contracts under its own weight, its core begins to heat up until its central temperature has reached around 10^7 K. At this point proton-burning reactions begin to occur. This is the beginning of the main sequence – a long, quiescent phase of evolution that our Sun is currently undergoing.

During its time on the main sequence a star converts hydrogen[1] into helium. There are several pathways by which this may happen. The first are the three pp chains which are the dominant source of energy below 2×10^7 K. The ppI chain involves the sequences of reactions

$$\begin{aligned} \mathrm{p} + \mathrm{p} &\rightarrow \mathrm{D} + e^+ + \nu \\ \mathrm{p} + \mathrm{D} &\rightarrow {}^3\mathrm{He} + \gamma \\ {}^3\mathrm{He} + {}^3\mathrm{He} &\rightarrow {}^4\mathrm{He} + 2\mathrm{p}. \end{aligned} \tag{1.1}$$

For each ^{4}He nucleus produced by this sequence of reactions, 26.7 MeV of energy is liberated. There are two alternate paths for producing ^{4}He other than that outlined above. First, the ppII chain involves the conversion of ^{3}He via the reactions

$$\begin{aligned} {}^3\mathrm{He} + {}^4\mathrm{He} &\rightarrow {}^7\mathrm{Be} + \gamma \\ {}^7\mathrm{Be} + e^- &\rightarrow {}^7\mathrm{Li} + \nu \\ {}^7\mathrm{Li} + \mathrm{p} &\rightarrow 2\,{}^4\mathrm{He} \end{aligned} \tag{1.2}$$

which liberates 19.8 MeV of energy. Second, the ppIII chain produces ^{4}He from ^{7}Be:

$$\begin{aligned} {}^7\mathrm{Be} + \mathrm{p} &\rightarrow {}^8\mathrm{B} \\ {}^8\mathrm{B} &\rightarrow {}^8\mathrm{Be} + e^+ + \nu \\ {}^8\mathrm{Be} &\rightarrow 2\,{}^4\mathrm{He} \end{aligned} \tag{1.3}$$

which produces 18.2 MeV of energy.

Above temperatures of 2×10^7 K, and in the presence of carbon, nitrogen and oxygen, a different set of reactions dominates energy production from hydrogen. This is the CNO bi-cycle which uses carbon, nitrogen and oxygen

[1] Or rather protons, because the temperatures in the core are so high that electrons are no longer bound to their parent atoms.

as catalysts to produce ^{4}He. The CN-cycle involves the reactions

$$\begin{aligned} {}^{12}\mathrm{C} + \mathrm{p} &\rightarrow {}^{13}\mathrm{N} + \gamma \\ {}^{13}\mathrm{N} &\rightarrow {}^{13}\mathrm{C} + e^+ + \nu \\ {}^{13}\mathrm{C} + \mathrm{p} &\rightarrow {}^{14}\mathrm{N} + \gamma \\ {}^{14}\mathrm{N} + \mathrm{p} &\rightarrow {}^{15}\mathrm{O} + \gamma \\ {}^{15}\mathrm{O} &\rightarrow {}^{15}\mathrm{N} + e^+ + \nu \\ {}^{15}\mathrm{N} + \mathrm{p} &\rightarrow {}^{12}\mathrm{C} + {}^{4}\mathrm{He}. \end{aligned} \tag{1.4}$$

At higher temperatures, the NO-cycle becomes active. Here, instead of ^{15}N capturing a proton to form ^{12}C and ^{4}He, the following sequence of reactions takes place

$$\begin{aligned} {}^{15}\mathrm{N} + \mathrm{p} &\rightarrow {}^{16}\mathrm{O} + \gamma \\ {}^{16}\mathrm{O} + \mathrm{p} &\rightarrow {}^{17}\mathrm{F} + \gamma \\ {}^{17}\mathrm{F} &\rightarrow {}^{17}\mathrm{O} + e^+ + \nu \\ {}^{17}\mathrm{O} + \mathrm{p} &\rightarrow {}^{14}\mathrm{N} + {}^{4}\mathrm{He}. \end{aligned} \tag{1.5}$$

The main sequence eventually terminates when all the hydrogen in the core has been processed into helium. As helium burning reactions require much higher temperatures than those for hydrogen burning reactions, nuclear reactions temporarily cease in the core.

1.1.2 The Red Giant Branch

While the core of the star remains inert after hydrogen burning has ceased there, burning reactions continue to occur in a shell around it. It is at this point that the star makes the transition to what is know as the red giant branch (RGB). The envelope of the star begins to expand, eventually reaching radii over one hundred times that of the Sun. The star becomes substantially more luminous and its surface temperature drops as shown in Figure 1.1. The reason for this transition is poorly understood.

As the star ascends the red giant branch the convective envelope deepens, reaching into layers that have been partially processed by hydrogen burning. This pulls material to the surface, altering the surface composition. The

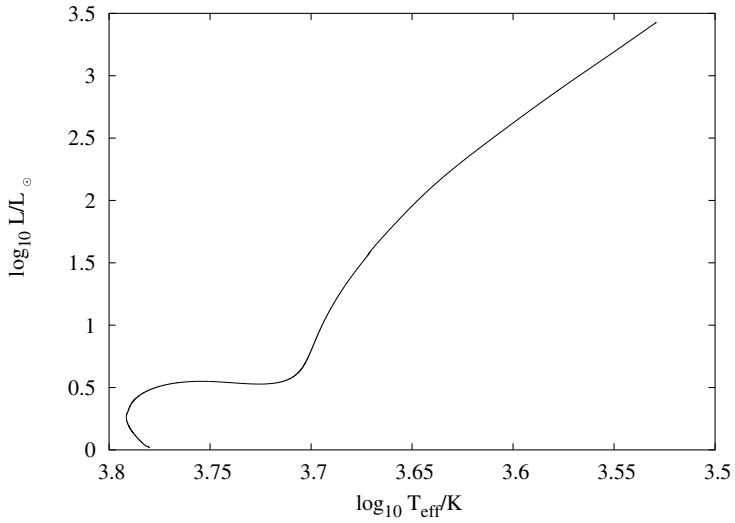

Figure 1.1: Hertzsprung-Russell diagram for a $1\,M_{\odot}$ star of Z=0.008, showing its transition from the main sequence to the red giant branch. This model is evolved without mass loss.

surface becomes enhanced in ^{4}He and ^{14}N while the abundance of carbon drops. Proceeding up the RGB, the core of the star grows in mass and, as it does so, it becomes hotter and denser. In stars of mass greater than about $2.3\,M_{\odot}$ (the exact dividing line depends on metallicity) helium ignites in conditions where the core is supported by pressure owing to thermal motions and the star makes the transition to core helium burning.

In stars less massive than $2.3\,M_{\odot}$ the situation is more complex. For these stars pressure owing to thermal motions is insufficient to prevent the core from collapsing. The core contracts until it is so dense that its electrons are competing for the same space. The core is now said to be degenerate and this degeneracy pressure prevents further collapse. Under such conditions the pressure is no longer dependent on the temperature of the material which is what usually keeps burning steady - if the temperature of the material rises, so does its pressure, causing an expansion which subsequently cools the material. When the helium ignites (at a temperature of around $10^8\,K$) it does so in a violent manner in what is referred to as a helium flash.

Because the core of the star has no thermostatic control as helium burns the temperature rises. Helium burning requires three ^{4}He nuclei (α-particles) to meet for a reaction to occur which is unusual and means that the reaction

has a particularly high temperature dependence. As the core heats up the rate of helium burning, or the triple-α reaction increases rapidly and leads to a further increase in the temperature. During the helium flash luminosities from helium burning can reach over 10^9 times the luminosity of our Sun. Eventually the core becomes hot enough to restore thermal pressure support to the star and quiescent core helium burning can begin.

1.1.3 The Asymptotic Giant Branch

Once helium burning has been established, the star enters the core helium burning phase. This is the helium burning equivalent of the main-sequence and it lasts for about one tenth of the star's life on the main-sequence. As the core of the star runs out of helium it begins to ascend the asymptotic giant branch (AGB), so-called because in low-mass stars it runs almost along the RGB and beyond as can be seen in Figure 1.2. The evolution up the AGB is marked by the solid line, starting from the lower left. There is a very rapid transition from the tip of the RGB (top right of the dashed line) to core helium burning (lower left of the solid line) which is unmarked in this diagram.

As the star ascends the AGB it expands once again and it cools. The effect is even more extreme than on the RGB. The convective envelope deepens in the same way as on the RGB. If the star is more massive than about $4\,\mathrm{M}_\odot$ then the envelope may reach down as far as the hydrogen burning shell, again pulling material to the surface and altering the surface composition of the star. This process is known as second dredge-up. The composition changes are similar to those during first dredge-up except that the envelope reaches even deeper into the star so that the products of complete CNO cycling (as opposed to just partial cycling in the case of the RGB) are brought to the surface.

As the star ascends the AGB, the helium burning shell slowly moves outwards in mass and the region between it and the hydrogen burning shell narrows. Eventually, the star reaches a configuration where the intershell is too narrow to remain stable and thermal pulses may occur. At this point, the star has an inert carbon-oxygen core surrounded by a thin helium burning shell. Above this lies an intershell region, on top of which is a hydrogen burning shell. The bulk of the star's mass rests in a deep convective envelope.

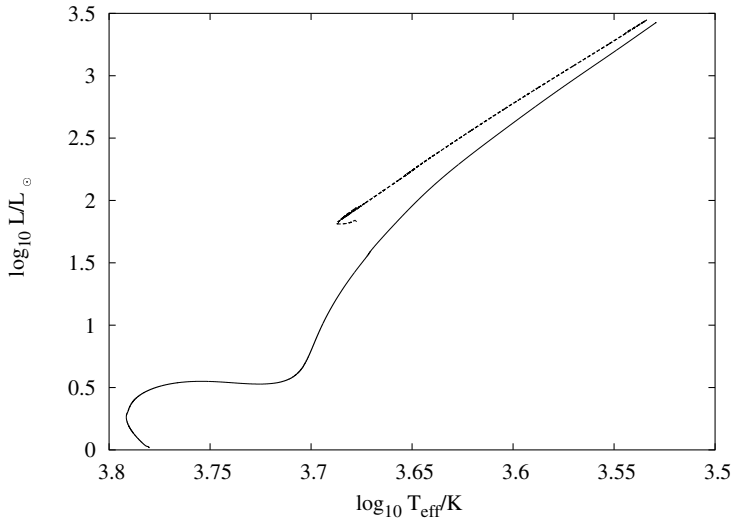

Figure 1.2: Hertzsprung-Russell diagram for a $1\,M_{\odot}$ star of Z=0.008, showing its transition from core helium burning to the AGB. The solid line marks the evolution from core He-burning to the AGB, while the dashed line is the prior evolution up the RGB.

Figure 1.3 shows a schematic diagram of the star's interior. It is this phase of evolution and the occurrence of thermal pulses with which this work is concerned.

1.2 A Brief History of the Thermally Pulsing Asymptotic Giant Branch

1.2.1 The Discovery of Thermal Pulses

Like much of the scientific canon, the story of the discovery of the thermally pulsing asymptotic giant branch (TP-AGB) is one of serendipity. In 1965 Schwarzschild and Härm were attempting to calculate the evolution of a $1\,M_{\odot}$ star when they encountered what they described as "a new type of difficulty" (Schwarzschild & Härm, 1965). Once their helium shell became sufficiently thin, oscillations in the luminosities of the hydrogen and helium burning shells were found. These became progressively more and more violent. Naturally[2] they assumed this to be a numerical instability but

[2]At least for those with experience in computational stellar evolution, that is.

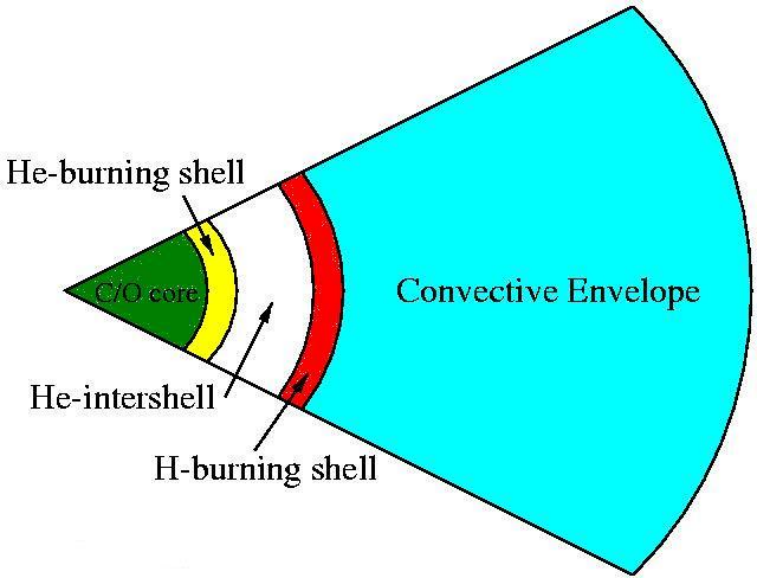

Figure 1.3: The interior structure of a typical AGB star. The figure is not to scale in order to clearly show the intershell region which is of particular interest to this work. The extended convective envelope dominates in both mass and radius.

subsequent analysis showed that it was indeed a true, physical consequence of the star's configuration.

The occurrence of thermal pulses (TPs), or shell flashes as they were called in the early literature, is a consequence of the thinness of the helium burning shell and the high temperature sensitivity of the triple-α reaction. The theory is described, for AGB stars, by Schwarzschild & Härm (1965) and more recently has been generalized to apply to all shell sources by Yoon et al. (2004).

In order for a shell source to become thermally unstable two things must happen. First, if energy from nuclear burning is dumped into the shell, then the temperature must rise. Secondly, the increased radiative loss due to the raising of the shell temperature must not carry energy away from the shell faster than it is being generated. If both these conditions are satisfied then the temperature in the shell continues to build up and a thermonuclear runaway results. The former of these conditions can be expressed by the equation

$$\mathrm{d}q = c^* \mathrm{d}T, \tag{1.6}$$

where dq is change in energy per unit mass, dT the change in temperature of the shell and c^* is the gravothermal specific heat capacity[3], defined by

$$c^* = c_{\rm P}\left(1 - \bigtriangledown_{\rm ad}\frac{\alpha_{\rm s}\alpha_{\rm T}}{\alpha_{\rm s}\alpha_{\rm P} - 1}\right) \tag{1.7}$$

where, for a burning shell of thickness D with its upper boundary at $r_{\rm s}$, we have

$$\alpha_{\rm s} = \frac{4}{3}(3D/r_{\rm s} - 3(D/r_{\rm s})^2 + (D/r_{\rm s})^3), \tag{1.8}$$

$$\alpha_{\rm P} = \left(\frac{\partial \ln \rho}{\partial \ln P}\right)_T, \tag{1.9}$$

$$\alpha_{\rm T} = -\left(\frac{\partial \ln \rho}{\partial \ln T}\right)_P \text{ and} \tag{1.10}$$

$$\bigtriangledown_{\rm ad} = \left(\frac{\partial \ln T}{\partial \ln P}\right)_{\rm ad}. \tag{1.11}$$

In order for a system to favour thermal instability c^* must be positive so that as heat is added to the system, the temperature rises. However, this alone is insufficient to guarantee thermal instability. We must also consider the shell's interaction with its surroundings. The following derivation is taken from Yoon et al. (2004). The equation of energy conservation in a star is given by

$$\frac{\partial L_r}{\partial M_r} = \epsilon_N - \frac{{\rm d}q}{{\rm d}t} \tag{1.12}$$

where ϵ_N is the rate of nuclear energy generation. Integrating over our shell source of thickness D and mass $\Delta M_{\rm s}$, this becomes

$$L_{r_{\rm s}} - L_{r_0} = L_N - L_g \tag{1.13}$$

where $r_{\rm s}$ and r_0 denote the upper and lower boundaries of the shell respectively, $L_N = \int_{\Delta M_{\rm s}} \epsilon_N {\rm d}M_r$ is the luminosity due to nuclear burning and $L_g = \int_{\Delta M_{\rm s}} \frac{{\rm d}q}{{\rm d}t}{\rm d}M_r$. But most of the energy flows out of the upper boundary of the shell and so $L_{r_{\rm s}} \gg L_{r_0}$. Perturbing equation 1.13 gives

$$\delta L_{r_{\rm s}} = \Delta M_{\rm s}\delta\epsilon_N - \Delta M_{\rm s}\frac{{\rm d}\delta q}{{\rm d}t} \tag{1.14}$$

[3]See Appendix A.1 for a derivation.

where δL_{r_s}, $\delta\epsilon_N$ and δq are the perturbations in the luminosity at the top of the shell, the energy generation rate and the energy per unit mass respectively. Combining this with thermodynamic relations and assuming radiative heat transfer,we may arrive[4] at:

$$\tau_{\rm th}\dot{\theta} = \sigma\theta \tag{1.15}$$

where $\theta = \delta T/T$, $\tau_{\rm th} = \Delta M_{\rm s} T c_P / L_{r_s}$ and

$$\sigma = \frac{\nu - 4 - \kappa_T + \frac{\alpha_T}{\alpha_{\rm s}\alpha_P - 1}(\lambda + \alpha_s + \kappa_P)}{c^*/c_P} \tag{1.16}$$

with $\kappa_T = (\partial \ln\kappa/\partial \ln T)_\rho$, $\kappa_\rho = (\partial \ln\kappa/\partial \ln\rho)_T$, $\nu = (\partial \ln\epsilon_N/\partial \ln T)_\rho$ and $\lambda = (\partial \ln\epsilon_N/\partial \ln\rho)_T$. If $\sigma > 0$ then a positive perturbation to the temperature grows and thermal instability results. In an AGB star the relevant burning shell is processing helium via the triple-α reaction which has a very high temperature dependence (ν may be around 40 or more) and so it is possible for thermal instability to occur and lead to a thermal pulse.

With the thermal pulses known to occur in low-mass stars, the confirmation of their occurrence in intermediate-mass stars soon followed (Weigert, 1966). The details of what happens during a thermal pulse were gradually fleshed out. It was found that, over a few pulses, the helium burning luminosity could reach over $10^7\,{\rm L}_\odot$ (Schwarzschild & Härm, 1967).

The effect of a thermal pulse on the structure of a star is dramatic. The runaway helium burning, owing to the phenomenal rate at which energy is generated, drives a convection zone between the helium and hydrogen burning shells, mixing the ashes of helium burning (predominantly carbon-12, but also some oxygen-16) throughout this region (Schwarzschild & Härm, 1967). Eventually conditions in the helium shell force it to expand pushing all the material above it outward and hence forcing it to cool. The hydrogen burning shell cools so much that it is extinguished. In fact, the only thing that an observer would see happen would be a drop in the star's luminosity – the vast amount of energy generated by the helium burning is all used up in driving the expansion of the material above it (Iben, 1975).

Eventually the helium shell cools after burning intensely for tens of years.

[4] See Appendix A.2 for the full derivation.

The star then begins to recover from the trauma. The outer layers contract, heating up as they go. Eventually the hydrogen shell becomes sufficiently hot that it can begin burning hydrogen again. This marks the beginning of the quiescent interpulse period (IP) which lasts for the order of 10^5 years before the helium shell reignites and the star goes into another thermal pulse.

1.2.2 Third Dredge-up

Unsurprisingly the expansion caused by a thermal pulse has important effects on the structure of a star. As the pulses become more and more violent, the convective envelope of the star moves deeper and deeper into the star as it recovers from each thermal pulse. It was initially believed that, under appropriate conditions, the separation between the envelope and the hydrogen-helium discontinuity would tend towards a minimum or asymptotic limit (Sweigart, 1974). However, it was subsequently found, in a $7\,M_\odot$ model of solar metallicity, that the envelope could penetrate into regions where the intershell convection zone had been active (Iben, 1975). This meant that the carbon that had been produced during helium burning was pulled into the envelope. This process is depicted in Figure 1.4 and came to be known as third dredge-up (TDUP). Third dredge-up is an extremely important process as it allows material processed by nuclear reactions in the depths of a star to reach the surface where they can be observed and also returned to the interstellar medium via mass loss. On account of the recurring nature of thermal pulses TDUP can happen many times over and so greatly influence the composition of the star.

The occurrence of TDUP in intermediate-mass stars is intimately connected with another process that affects the surface composition of stars. If the convective envelope can penetrate sufficiently deeply into the star the H-shell will reignite at a temperature high enough for the CN-cycle to operate. The shell continues to burn at the base of the convective envelope during the interpulse period. This converts freshly dredged-up ^{12}C into ^{14}N. This requires a temperature greater than $8 \times 10^7\,K$ (Iben, 1976) and was found to occur when TDUP was discovered (Iben, 1975). The process eventually acquired the label of hot-bottom burning (HBB).

The issue of TDUP proved to be a thorny one for the AGB community. Initially, only the intermediate-mass stars were found to give dredge-up. At-

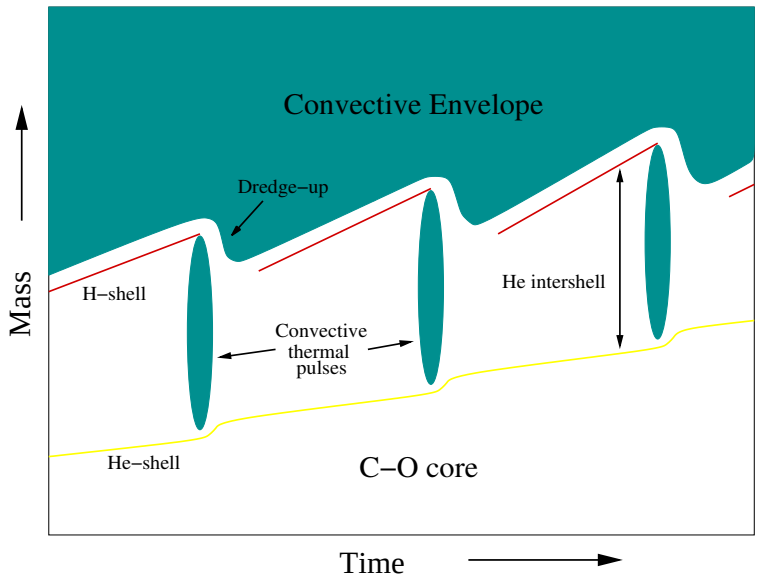

Figure 1.4: Representation of the evolution of the interior of a TP-AGB star, showing thermal pulses and third dredge-up. Convective regions are in green. The hydrogen burning shell is the red line and the helium burning shell is the yellow line.

tempts to find dredge-up at lower core masses were for the most part unsuccessful (e.g. Sackmann, 1980; Wood & Zarro, 1981), though Wood (1981) had succeeded in producing a $2\,M_{\odot}$ model at $Z = 0.001$ with dredge-up. Observations suggested that TDUP should be occurring at lower core masses than the models were predicting (see 1.4 below). In the late 1980's some reconciliations between theory and observations were made, with notable successes being scored by Boothroyd & Sackmann (1988) and Lattanzio (1989) but models could still not be produced with sufficiently low core masses.

It was pointed out that there was a problem with the way in which convective boundaries are formally located. According to the Schwarzschild Criterion (see e.g. Ostlie & Carroll, 1996), a convective boundary is located at the point where the radiative and adiabatic temperature gradients are equal. However, this only states the point at which the acceleration on a moving blob of material goes to zero – it does not necessarily follow that the velocity of the blob at that point is also zero. This led some to propose that convective overshooting could occur. It was envisioned that material could still be in motion after passing through the formal Schwarzschild boundary. Such a mechanism would extend the depth of mixing and could potentially

produce deeper dredge-up.

It was pointed out by Frost & Lattanzio (1996) that some additional form of mixing, such as overshooting, might be necessary to resolve some numerical issues. As TDUP occurs the convective envelope – rich in hydrogen – penetrates into layers of the star that are depleted in hydrogen. The resultant discontinuity in the chemical composition results in a discontinuity in the opacity and produces a discontinuity in the radiative temperature gradient. This inhibits further penetration as large changes in the state variables would need to occur for $\bigtriangledown_{\rm r}/\bigtriangledown_{\rm ad}$ to exceed unity in the radiative region. They pointed out that any additional mixing across this boundary would encourage further penetration. Unless $\bigtriangledown_{\rm r}/\bigtriangledown_{\rm ad}$ approached unity at the convective boundary, the boundary would be unstable. This point was re-iterated by Mowlavi (1999).

Further examination of numerical effects on the occurrence of TDUP were performed by Straniero et al. (1997). They found third dredge-up to occur self-consistently down to masses as low as $1.5\,{\rm M}_{\odot}$ for solar metallicity models, without the need to apply any sort of extra mixing. They found that high spatial and temporal resolution was required in order to find dredge-up in low-mass models. Pols & Tout (2001) subsequently showed that by careful choice of the mixing algorithm $\bigtriangledown_{\rm r}/\bigtriangledown_{\rm ad}$ would approach unity at convective boundaries making them stable and hence circumventing the need for extra mixing.

The issue of TDUP is still a problematic one. Results for the various codes in use at the present day differ quite dramatically. Some people favour the inclusion of convective overshooting (Herwig, 2000), others take a more phenomenological approach to the issue of extra mixing (Frost & Lattanzio, 1996) while others do not include it at all. It is an area of study that still requires some effort to resolve its remaining issues.

1.3 TP-AGB Nucleosynthesis and the *s*-process

Given the occurrence of the TDUP process, AGB stars offer the tantalizing prospect that material synthesized during thermal pulses could be brought to the surface where it might be observed. The existence of complex nucleosynthesis together with the prospect of substantial mass loss makes AGB

stars a valuable area of study from the point of view of galactic chemical evolution.

1.3.1 Light Element Nucleosynthesis

The intershell of an AGB star is a rich site for the nucleosynthesis of light elements. Aside from the production of carbon-12 via the triple-α reaction many other elements can be synthesized there. In the hydrogen burning shell, hydrogen is burned via the CNO cycle which converts some of the dredged-up carbon into ^{14}N. This acts as a seed for the production of several species. For example, ^{22}Ne is produced from this by a double α-capture (Iben, 1975). First, the unstable nucleus ^{18}F is formed via $^{14}\mathrm{N}(\alpha,\gamma)^{18}\mathrm{F}$ and this then rapidly decays to give ^{18}O. This then captures another α particle to produce ^{22}Ne.

Goriely et al. (1989) proposed that AGB stars could be a site for the synthesis of ^{19}F, an element whose origins have long puzzled astronomers. Again, starting with ^{14}N as a seed, the pathway for the production of ^{19}F is:

$$^{14}\mathrm{N}(\alpha,\gamma)^{18}\mathrm{F}(\beta^{+})^{18}\mathrm{O}(\mathrm{p},\alpha)^{15}\mathrm{N}(\alpha,\gamma)^{19}\mathrm{F} \tag{1.17}$$

which requires protons to be present. These can be provided by the reaction $^{14}\mathrm{N}(\mathrm{n},\mathrm{p})^{14}\mathrm{C}$, with the neutrons coming from $^{13}\mathrm{C}(\alpha,\mathrm{n})^{16}\mathrm{O}$. Other alternative sites for ^{19}F production have been proposed including core helium burning in massive stars (Meynet & Arnould, 1993, 2000) and supernova explosions (Woosley & Weaver, 1995). However, AGB stars remain the only confirmed site for fluorine production to date (Jorissen et al., 1992).

In addition to nucleosynthesis in the intershell, the hydrogen burning shell is also a site for nucleosynthesis. As well as converting dredged-up carbon into nitrogen, other proton capture reactions may be in operation. The Ne-Na cycle involves the isotopes ^{20,21,22}Ne and ^{21,22,23}Na and leads to a production of ^{23}Na from ^{22}Ne at temperatures above about 20×10^6 K (Arnould et al., 1999). A second cycle, the Mg-Al cycle, becomes operational at temperatures of about 30×10^6 K and involves the isotopes ^{24,25,26}Mg, ^{25,26,27}Al and also ^{27}Si (Arnould et al., 1999).

Because TDUP brings material from the intershell up through the hydrogen burning shell (while it is inactive), the nucleosynthesis of certain species

can be affected by both regions. For example, ^{19}F is synthesized in the intershell by He burning as outlined above but may also be destroyed in the H-shell via the reaction $^{19}\mathrm{F}(\mathrm{p},\gamma)^{20}\mathrm{Ne}$ (Forestini et al., 1992).

1.3.2 Nucleosynthesis via the *s*-process

In addition to the nucleosynthesis of light elements, TP-AGB stars may also be the site for the production of the *s*-process elements, some isotopes from Sr up to lead. The *s*-process is the capture of neutrons by nuclei in conditions of sufficiently low neutron density that any unstable products have time to decay before another neutron is captured (see e.g. Clayton, 1983). This is in direct contrast to the *r*-process in which additional neutrons are captured before the nucleus has a chance to decay and leads to the production of neutron-rich isotopes.

The earliest calculations suggested that the intershell convection zone could expand so far as to encroach on the tail of the hydrogen burning shell. This would lead to the formation of ^{13}C in the intershell and the reaction $^{13}\mathrm{C}(\alpha,\mathrm{n})^{16}\mathrm{O}$ could then provide the necessary neutrons for *s*-process nucleosynthesis (Sanders, 1967; Schwarzschild & Härm, 1967) to occur. Two mechanisms were proposed as to how protons from the H-burning shell could find their way into the intershell convection zone. The Ulrich-Scalo mechanism proposed that when the intershell convection zone was at its maximum extent, protons could be mixed into it via a non-thermal process (Ulrich & Scalo, 1972). Alternatively, it was thought that the intershell convection zone could merge with the convective envelope (the Smith-Sackmann-Despain mechanism, Smith et al., 1973).

Iben (1975) proposed an alternative means of providing neutrons, the reaction $^{22}\mathrm{Ne}(\alpha,\mathrm{n})^{25}\mathrm{Mg}$. This had the advantage of requiring no additional mixing: ^{22}Ne could be directly synthesized in the intershell. He subsequently went on to show that the intershell convection zone could not reach up to the envelope because the hydrogen burning shell acts as an effective entropy barrier (Iben, 1976). However, in order for this reaction to become effective the temperature in the He-burning shell must reach over 3×10^8 K. Observations of *s*-process elements in red giants suggested that the *s*-process was operational in low-mass stars whose intershell temperatures would not reach that high. In addition, the ^{22}Ne source produces a high-intensity burst of

neutrons for a short time – a pattern that does not reproduce the observed *s*-process distribution.

For these reasons, the search for a means to introduce protons into the carbon rich intershell continued. In 1982, Iben & Renzini proposed that semiconvection could provide the necessary mixing. Cooling caused by the expansion of the star could lead to recombination of ionized carbon. This causes an increase in the opacity of the material and hence a semiconvective zone may develop, mixing carbon and hydrogen to produce ^{13}C (Iben & Renzini, 1982a,b). Unfortunately, this mechanism was not found to occur in many models.

The search for a viable mechanism for introducing protons into the carbon-rich intershell in order to form a ^{13}C pocket is still ongoing. Recent work has centred around the use of convective overshooting (Herwig, 2000), motivated by hydrodynamical simulations (Freytag et al., 1996), rotational mixing (Langer et al., 1999) and internal gravity waves (Denissenkov & Tout, 2003). Each of these mechanisms has its own particular problems and a solution to the problem of the formation of the carbon-13 pocket still eludes us.

1.3.3 Mass Loss

One of the important, and unfortunately poorly understood, aspects of AGB evolution is that of mass loss. The AGB phase is finally terminated when mass loss has removed the envelope of the star and a post-AGB object is formed. Mass loss allows the nucleosynthetic products of AGB evolution to be returned to the interstellar medium and, because low-mass stars are formed far more abundantly than those of higher mass (Kroupa et al., 1993), allows AGB stars to contribute significantly to galactic chemical evolution.

Mass loss also has important effects on the evolution of AGB stars. In the lowest-mass AGB stars it is possible for mass loss to strip the star of its envelope before TDUP has a chance to occur (Karakas et al., 2002). If TDUP does occur its efficiency can still be affected by mass loss. In intermediate-mass AGB stars the occurrence of mass loss can inhibit the occurrence of hot-bottom burning in the later stages of evolution, while still allowing TDUP to occur. This allows the formation of bright carbon stars (Frost et al., 1998).

Of the early calculations of AGB evolution, few used any mass loss. Those

that did (e.g. Schönberner, 1979) employed the Reimers' formula (Reimers, 1975)

$$\dot{M} = -4 \times 10^{-13} \eta \frac{LR}{M} \, \mathrm{M_{\odot} yr^{-1}} \tag{1.18}$$

where L, R and M are the star's luminosity, radius and mass in solar units. The value of the free parameter η is usually taken as 0.4 for red giants. However, it was recognized by Renzini (1981) that the mean mass-loss rate required to produce a typical planetary nebula was around $3 \times 10^{-5} \, \mathrm{M_{\odot} yr^{-1}}$. He coined the term superwind as this value was significantly greater than those given by the Reimers formula. Many calculations still use the Reimers formula, generally with $0.4 < \eta < 3$, although $\eta = 10$ may be used in extreme cases (Straniero et al., 1997, 2003).

In an attempt to produce a more physically consistent picture, Vassiliadis & Wood (1993) produced a mass-loss relation based on observations of OH/IR stars and other pulsating, dust-enshrouded AGB stars. They linked the mass-loss rate, $\dot{M}$ in $\mathrm{M_{\odot} yr^{-1}}$, of an object to its Mira pulsational period, P (in days), via the relations:

$$\log \dot{M} = -11.4 + 0.0123P \tag{1.19}$$

and

$$\dot{M} = \frac{L}{c v_{\mathrm{exp}}}, \tag{1.20}$$

where $v_{\mathrm{exp}} = -13.5 + 0.056P$ is the expansion velocity of the wind far from the star in $\mathrm{km\,s^{-1}}$ and c is the speed of light. The mass loss is taken to be the smaller of the two values calculated with the above expressions. This law has the advantage of providing for a superwind phase which can remove a star's envelope over the course of a few pulses. This mass loss law has been used in recent computations by Karakas et al. (2002).

One other mass-loss relation has also been used in current calculations, that of Blöcker (1995). It is grounded in theory, rather than empirically determined, based as it is on simulations of shock-driven winds in the atmospheres of Mira-like stars (Bowen, 1988). It was developed to reflect the strong increase of mass loss during the AGB and to be applicable to stellar evolution calculations (Blöcker, 1995). It is similar to the Reimers prescription but with a steeper dependence on luminosity and a shallower dependence

on mass. The formula is expressed as:

$$\dot{M} = 4.83 \times 10^{-9} \left(\frac{M}{\mathrm{M}_{\odot}} \right)^{-2.1} \left(\frac{L}{\mathrm{L}_{\odot}} \right)^{2.7} \dot{M}_{\mathrm{Reimers}}. \tag{1.21}$$

Because of its use of the Reimers formula, this law also suffers from the problem of having a free parameter that must be determined (or worse, guessed). Recent calculations using Blöcker's relation include those of Herwig & Austin (2004) and Ventura (2004).

1.4 Observational Constraints

Owing to the long timescales involved for a full thermal pulse cycle, no direct observation of an AGB star undergoing a thermal pulse has ever been made. It is theoretically possible given modern day survey techniques that the dip in a star's luminosity following the peak of a thermal pulse could be detected but it seems unlikely (and perhaps not particularly valuable) that such efforts will be made. The question, "what evidence do we have for the real, physical existence of TP-AGB stars?" must be asked. It would be a serious embarrassment for the author if these stars only existed in theory!

1.4.1 Direct Observations

There exist various observations that seem to be well explained if we believe the objects to be TP-AGB stars. From an observational point of view, AGB stars can be divided into groups based on low-resolution optical spectra. Those stars in which TiO bands dominate are classified as M stars; if C_2 or CN bands dominate then the star is a C (carbon) star (Lattanzio & Wood, 2004). This equates to the star having a surface C/O ratio less than unity for M stars in order that molecules like TiO can form. For C stars C/O must be greater than unity so that there are excess C atoms to form molecules like CN. The progression from an M star to a C star can be readily explained in terms of AGB evolution. The repeated operation of TDUP brings newly synthesized carbon to the surface, converting a star that was once oxygen-rich to one that is carbon rich.

The existence of carbon stars provides us with a test for theoretical models. Owing to the molecular bands described above, carbon stars can be easily

detected in photometric surveys (see Cook & Aaronson, 1989, for a description of the method). In a population at a known distance it is possible to create a luminosity function for the observed carbon stars. The Large and Small Magellanic Clouds have well-determined distances and hence we have luminosity functions for them (Groenewegen, 2004). AGB models must be able to reproduce these in order to be considered correct. In fact, it was the existence of low-luminosity carbon stars in these populations that led Iben to formulate the carbon star mystery (Iben, 1981). At the time models were unable to produce low-luminosity carbon stars and the intermediate-mass models produced luminous carbon stars that were not observed. The latter problem was solved once it was realized that hot-bottom burning would convert the dredged-up carbon into nitrogen and prevent intermediate mass objects forming carbon stars. The formation of low-luminosity carbon stars is still problematic today (see Chapter 4).

The broad categories of M and C stars can be further subdivided into the types MS, S and SC. These classifications are again based on low-resolution optical spectra, this time based on molecular bands involving the *s*-process element zirconium. If molecular features associated with ZrO are found together with TiO bands the star is of type MS. As the C/O ratio tends to unity and all the available oxygen atoms are locked up in CO, TiO bands will disappear and ZrO will dominate. The star is then of type S (Keenan & Boeshaar, 1980). For a star to be of type SC it must display strong sodium D lines and no ZrO lines. Again, these properties are readily explicable by the theory of TP-AGB stars as they form a sequence from oxygen-rich to carbon-rich objects that is readily explained by the dredge-up of carbon in TP-AGB stars.

The existence of *s*-process elements also seems to require the existence of AGB stars. The strongest supporting evidence for this comes from the detection of technetium in some stars. Merrill (1952) was the first person to detect technetium in S-stars. Technetium has no stable isotopes but the element ^{99}Tc is produced via the *s*-process and has a half-life of 2×10^5 years. In order to observe Tc, it must have been produced within a few half-lives of the isotope observed. *If* we assume that the isotope observed is ^{99}Tc – which is by no means certain as it is only the third longest lived of the Tc isotopes – then its presence can readily be explained by TP-AGB stars. The *s*-process

elements are formed in the intershell of an AGB star and then brought to the surface by TDUP. Recent survey work has been carried out to search for Tc in AGB stars (Lebzelter & Hron, 2003). Comparing the luminosity of stars that do or do not show Tc in their spectra with theoretical models allows us to determine in which stars the *s*-process and TDUP are active.

1.4.2 Pre-solar Grains

In the last 20 years it has become possible to study individual interstellar grains brought to Earth in meteorites. These grains are generally believed to have formed as material was returned from stars to the interstellar medium. A wide variety of such grains have been discovered. The first to be recovered from meteorites were carbon-rich grains including silicon carbide (SiC), graphite and diamond (see e.g. Bernatowicz et al., 1987; Lewis et al., 1987). Grains containing oxygen compounds, for example corundum (Al_2O_3), proved more difficult to isolate. The first oxygen-rich grain in which an isotopic ratio significantly different from the solar system value was measured was Orgueil B (Huss et al., 1992). By measuring the isotopic composition of these grains, we can hope to gain an insight into the environments in which they might have formed.

In the case of the carbon-rich grains, they must have formed in environments where the C/O ratio exceeds unity. In the case of SiC grains, they are found to be carriers of enhanced levels of ^{128}Xe and ^{130}Xe (Srinivasan & Anders, 1978), which are isotopes associated with the *s*-processes. Further measurements of trace heavy elements such as Kr, Ba, Nd and Sm also show clear evidence of an *s*-processes signature (Lewis et al., 1990; Ott & Begemann, 1990; Zinner et al., 1991). These features suggest that these grains are formed in the envelopes of low-mass TP-AGB stars which should be rich in carbon and *s*-process elements due to the action of TDUP. Measurements of isotopic ratios of both light and heavy elements in these grains allows us to constrain the nature of theoretical models.

In addition, the distribution of *s*-process elements allows us to probe the conditions in the interior of AGB stars. Certain *s*-process elements, such as ^{85}Kr, form isomeric states when they are produced by neutron capture. In the case of ^{85}Kr one state decays more rapidly that the other. In conditions of low neutron exposure such as those found in the ^{13}C pocket only the longer-

lived ground state is able to capture neutrons to feed the formation of ^{86,87}Sr (Lugaro et al., 2003). If the neutron exposure is of higher intensity, i.e. if the ^{22}Ne source is activated during a thermal pulse, then the isomeric state can also capture neutrons. This allows the formation of ^{86,87}Sr to be partly bypassed (Lugaro et al., 2003). By comparing models of the *s*-process in AGB stars with observed *s*-process element ratios we can hope to constrain which neutron sources are activated and hence the temperatures reached in thermal pulses.

Measurements of pre-solar grains have also suggested the requirement for additional physics not included in standard stellar evolution codes. Some pre-solar grains have isotopic ratios for ^{18}O/^{16}O and ^{17}O/^{16}O that cannot be explained by the action of first/second dredge-up, nor can the operation of hot-bottom burning in intermediate-mass stars account for them (Boothroyd et al., 1995). Boothroyd, Sackmann & Wasserburg found that data from grains coming from low-mass S and C stars required that material be transported from the cool convective stellar envelope to hotter layers of the star where ^{18}O could be depleted. They dubbed this mechanism cool bottom processing (Boothroyd et al., 1995). It should be noted that an extra mixing mechanism is also believed to be necessary in order to generate a ^{13}C pocket to provide a neutron source necessary for the *s*-process.

Chapter 2

STARS: a Stellar Evolution Code

The calculations made in this work were done using a derivative of the evolution code developed by Eggleton (1971, 1972). The code and its derivatives are unique in that they are the only stellar evolution code to solve the equations of stellar structure and evolution in a fully simultaneous manner. The code has been extensively modified over the last 35 years (Eggleton et al., 1973; Han et al., 1994; Pols et al., 1995). The current incarnation has come to be known as STARS. In this section, the input physics, details of the code and the modifications necessary to allow the code to be used on the TP-AGB are reviewed.

2.1 Input Physics

Stellar evolution calculations are based on a set of four equations which govern the structure of a star. For a spherically symmetric star that is non-rotating, these are

- the equation of hydrostatic equilibrium,

$$\frac{\mathrm{d}P}{\mathrm{d}m} = -\frac{Gm}{4\pi r^4}, \tag{2.1}$$

  where P, r and m are pressure, radius and the mass contained within a spherical shell of radius r respectively.

- The equation of mass conservation,

$$\frac{\mathrm{d}r}{\mathrm{d}m} = \frac{1}{4\pi r^2 \rho}, \tag{2.2}$$

  where ρ is density.

- The equation of energy generation,

$$\frac{\mathrm{d}L}{\mathrm{d}m} = \epsilon, \tag{2.3}$$

  where L is luminosity and ϵ is the energy generation rate including nuclear energy generation, energy from gravitational sources and energy losses from neutrino emission.

- The equation of energy transport, which may be expressed as

$$\frac{\mathrm{d}\ln T}{\mathrm{d}m} = - \bigtriangledown \frac{\mathrm{d}\ln P}{\mathrm{d}m} \tag{2.4}$$

  where $\bigtriangledown$ depends on whether the region of the star is radiative or convective.

In regions of the star that are radiative all the energy is transported by radiation and

$$\bigtriangledown = \bigtriangledown_{\mathrm{r}} = \frac{3\kappa P L}{16\pi a c g r^2 T^4} \tag{2.5}$$

where κ is the opacity, a is the radiation-density constant and $g = Gm/r^2$. In convective regions the situation is more complex with part of the energy flux being carried by convection and part by radiation. In such a situation the energy flux F is described by $F = F_{\mathrm{rad}} + F_{\mathrm{con}}$ where the subscripts denote the radiative and convective components. The actual temperature gradient of the star is determined by the radiative flux via

$$F_{\mathrm{rad}} = \frac{4acgT^4}{3\kappa P} \bigtriangledown . \tag{2.6}$$

In order to determine $\bigtriangledown$ it is necessary to describe how energy is transported by convection. This is done using mixing length theory (MLT)(Böhm-Vitense, 1958) which envisages convection as the motion of blobs of material that travel a characteristic distance, the mixing length l, before losing their

identity and mixing with the surrounding material. The mixing length is a free parameter of the theory and is normally expressed in terms of the pressure scale height, $H_{\rm P}$, as

$$l = \alpha H_{\rm p}, \tag{2.7}$$

where α is a dimensionless constant that is conventionally set by calibration to a solar model. The convective flux according to MLT[1] is given by

$$F_{\rm con} = \rho v c_{\rm P} \delta T, \tag{2.8}$$

where $c_{\rm P}$ is the specific heat capacity at constant pressure, v is the speed of the convective blob and δT is the difference in temperature between the blob and the surrounding medium. This latter quantity is given by

$$\frac{\delta T}{T} = (\bigtriangledown - \bigtriangledown_e)\frac{l}{2H_{\rm P}}, \tag{2.9}$$

where $\bigtriangledown_e$ is the temperature gradient for the moving element and $H_{\rm P}$ is the pressure scale height.

Work is done on the moving blob by buoyancy forces and, assuming that half of this goes into the kinetic energy of the blob, the final speed of the blob may be expressed as

$$v^2 = g\delta(\bigtriangledown - \bigtriangledown_e)\frac{l^2}{8H_{\rm P}}, \tag{2.10}$$

where $\delta = -(\partial \ln \rho / \partial \ln T)_{\rm P}$ and an equation for the convective flux in terms of temperature gradients arrived at. It is also possible to compute a fictitious temperature gradient $\bigtriangledown_{\rm r}$ assuming that all the flux is carried by radiation. The three expressions for the total, radiative and convective fluxes relate $\bigtriangledown$ to quantities that can readily be calculated and by obtaining $\bigtriangledown_e$ from the adiabatic temperature gradient (which is also straightforward to calculate) the actual temperature gradient in the star can be computed.

Equations 2.1-2.4 determine the (static) structure of the star. Henceforth we shall refer to them as the *structure equations*. In order to model the star's evolution we also need to track the composition of the star. The composition is altered by nuclear reactions and also by material being mixed throughout

[1]The derivation that follows is a brief outline of that in Kippenhahn & Weigert (1990) to which the interested reader is referred to for the full details.

Reaction	Source
^{1}H(p,$\beta^{+}\nu$)^{2}H	REACLIB
^{12}C(p, γ)^{13}N	CF88
^{14}N(p, γ)^{15}O	CF88
^{16}O(p, γ)^{17}F	CF88
^{4}He($\alpha\alpha, \gamma$)^{12}C	CF88
^{12}C(α, γ)^{16}O	CF88
^{14}N(α, γ)^{18}F	G00
^{16}O(α, γ)^{20}Ne	CF88
^{20}Ne(α, γ)^{24}Mg	CF88
^{12}C(^{12}C,γ)^{24}Mg	CF88
^{16}O(^{12}C,γ)^{30}Si	CF88
^{16}O(^{16}O,γ)^{32}S	CF88

Table 2.1: Reaction rates used by the code. Key: CF88, (Caughlan & Fowler, 1988); G00, (Görres et al., 2000) and REACLIB, 1991 updated version of Thielemann et al. (1986).

the star by convection. If mixing is assumed to be modelled as a diffusive process, the change in mass fraction X of the element i is governed by the equation

$$\frac{\mathrm{d}}{\mathrm{d}m}\left(\sigma\frac{\mathrm{d}X_i}{\mathrm{d}m}\right) = \frac{\mathrm{d}X_i}{\mathrm{d}t} + R_i - S_i, \tag{2.11}$$

where σ is the diffusion coefficient, R_i is the rate at which the species i is being burnt by nuclear reactions and S_i is the rate at which it is being produced by nuclear reactions (Eggleton, 1972).

The remaining physical inputs include the equation of state for the material, data covering reaction rates, neutrino losses and opacity of the material. The equation of state is described in Eggleton et al. (1973) and was enhanced and updated by Pols et al. (1995) to include the effects of Coulomb interactions and pressure ionization. The reactions used in the code and the sources from which they were obtained are listed in Table 2.1. The data on neutrino losses is taken from Itoh & Kohyama (1983), Munataka et al. (1987), Itoh et al. (1989) and Itoh et al. (1992). Opacities are taken from Alexander & Ferguson (1994), Rogers & Iglesias (1992) and Itoh et al. (1983).

2.2 Implementation

In order to implement the structure and composition equations, the stellar model is first divided up into a set of mesh points. The number of mesh points used depends on the complexity of the evolutionary phase being considered and the desired resolution of the model. Typically a main-sequence model is evolved with 199 mesh points while a TP-AGB model requires 999. Once a model is started the number of mesh points remains fixed. Mesh points are distributed at equal intervals of a mesh spacing function, Q, which is a function of the pressure P, temperature T, mass m and radius r throughout the star (Eggleton, 1971). This function is designed to push more mesh points into regions where they are needed such as burning shells and ionization zones. The mesh is adaptive so that as the star evolves, the mesh points move around to stay with physically important regions. This is different to the way most codes operate. In these codes, if additional resolution is required extra mesh points are added. For problematic phases of evolution, this can lead to models having thousands of mesh points in them making it slower to calculate models. The STARS mesh does not suffer from this problem.

The form of the mesh spacing function used by the code is

$$\begin{aligned} Q = \; & \ln\left(\frac{(m/M)^{2/3}}{c_1}+1\right) \; + \; c_2 \ln\left(\frac{r^2}{c_3}+1\right) \; - \; c_4 \ln\frac{T}{T+c_5} - \; c_6 \ln P \\ & - c_7 \ln\frac{P+0.1P_{\rm H}}{P+3P_{\rm He}} \; - \; c_8 \ln\frac{P+0.3P_{\rm He}}{P+3P_{\rm He}} \end{aligned} \tag{2.12}$$

where $c_1 \ldots c_8$ are appropriately chosen constants, M is the total mass and $P_{\rm H}$ and $P_{\rm He}$ are the values of P at the position of the boundary of the H- and He-exhausted cores respectively. The code uses units of 10^{30} kg for the mass, 10^9 m for the radius, Kelvin for the temperature and dynes for the pressure. The last two terms are included only during the TP-AGB phase. Typical choices for the coefficients on the TP-AGB are given in Table 2.2. They concentrate a large part of the mesh, about three-fifths, in the intershell region (between $0.1P_{\rm H}$ and $3P_{\rm He}$) while at the same time ensuring that during a TP, when T and P undergo rapid changes, the mesh does not move around too much in the intershell region so that numerical diffusion is suppressed.

Within the code the structure and composition equations, and the mesh spacing function, are written as implicit, finite difference equations. The

c_1	c_2	c_3	c_4	c_5	c_6	c_7	c_8
3.00	3.00	0.05	0.01	0.60	0.35	0.05	10^{-4}

Table 2.2: Typical coefficients used in the mesh spacing function on the TP-AGB.

code then solves these equations using the Henyey method (Henyey et al., 1959). Briefly, this involves taking a given model with a set of changes to each of the variables at each mesh point and then relaxing that solution until a new model is converged.

2.2.1 Convective Mixing and the Choice of σ

The issue of convection and convective mixing in evolution codes is a sensitive one and particularly so on the TP-AGB. It is therefore necessary to detail some important points on this subject. Convective mixing is is treated in the framework of the mixing-length theory (Böhm-Vitense, 1958). Equation 2.11 is approximated by an implicit second-order difference equation of the form

$$\sigma_{k+\frac{1}{2}} \frac{X_{k+1} - X_k}{\delta m_{k+\frac{1}{2}}} - \sigma_{k-\frac{1}{2}} \frac{X_k - X_{k-1}}{\delta m_{k-\frac{1}{2}}} = \left(\frac{X_k - X_k^0}{\Delta t} + R_{X,k} \right) \delta m_k, \qquad (2.13)$$

where X_k and X_k^0 are the abundances at mesh point k at the present and previous timestep, Δt is the timestep, $\delta m_{k\pm\frac{1}{2}}$ are the masses contained in the zones above and below mesh point k, $R_{X,k}$ is the net consumption rate of X by nuclear reactions, and $\sigma_{k\pm\frac{1}{2}}$ are the diffusion coefficients corresponding to these zones. The linear diffusion coefficient D is related to σ by $\sigma = (4\pi r^2 \rho)^2 D$, where r and ρ are radius and density. The calculation of D is discussed in further detail in section 2.4.1.

All the quantities including σ are defined only at each mesh point k so it is not a priori obvious how $\sigma_{k\pm\frac{1}{2}}$ should be calculated. In the standard calculations made with this code, $\sigma_{k+\frac{1}{2}} = \frac{1}{2}(\sigma_k + \sigma_{k+1})$ is used, following Eggleton (1972). Pols & Tout (2001) investigated the effect of taking a geometric mean $\sigma_{k+\frac{1}{2}} = \sqrt{\sigma_k \cdot \sigma_{k+1}}$ rather than an arithmetic mean. These schemes effectively differ only in zones where the Schwarzschild boundary is located between mesh points k and $k+1$. The arithmetic mean in effect allows the radiative mesh point adjacent to a convective boundary to be mixed while

the geometric mean does not. The choice is usually inconsequential but becomes important in the presence of a composition discontinuity that leads to a discontinuity in $\bigtriangledown_{\rm r}$ through the opacity dependence. Such discontinuities arise during core-helium burning at the edge of the convective core and at the bottom of the convective envelope during TDUP (Paczyński, 1977). The standard arithmetic mean ensures that $\bigtriangledown_{\rm r} - \bigtriangledown_{\rm ad}$ always approaches zero from the convective side of a boundary, even in the case of a discontinuity, so a convective boundary always corresponds to a *stable* Schwarzschild boundary ($\bigtriangledown_{\rm r} = \bigtriangledown_{\rm ad}$). However when there is a discontinuity in $\bigtriangledown_{\rm r}$ at the boundary even the slightest extra mixing makes it unstable and physically it is expected that mixing will occur until $\bigtriangledown_{\rm r} \leq \bigtriangledown_{\rm ad}$ when material can mix across the boundary. Pols and Tout demonstrated that use of the geometric mean for $\sigma_{k\pm\frac{1}{2}}$ suppresses this physical behaviour and prevents third dredge-up (see also the discussion in Mowlavi 1999 and Herwig 2000) so the arithmetic mean is always employed here.

2.3 Overview of the STARS Code Structure

The STARS code is a very compact program consisting of around 1500 lines of Fortran (from various decades). It consists of a series of subroutines which are outlined here and their inter-connections are displayed in Figure 2.1. The `main.f` routine controls passes to two separate loops of the program. The most used is the structure and evolution part of code. The physics is encompassed in `funcs1.f` and the difference equations are in `equns1.f`. This section of the code currently tracks the evolution of ^{1}H, ^{4}He, ^{12}C, ^{14}N, ^{16}O and ^{20}Ne, in addition to the variables relevant to the structure, namely $\ln f, \ln T, \ln m, \ln r$ and L. These routines make passes to the equation of state routine (`statef.f` via `statel.f` which filters out any unnecessary passes), the routine dealing with pressure ionization (`pressi.f`), the routine dealing with nuclear reaction rates (`nucrat.f`) and the opacity calculator (`opacty.f` which calls the spline fitting routine `opspln.f`). The second loop of the code, which comprises of a second package of physics (`funcs2.f`) and difference equations (`equns2.f`), is designed to track the evolution of minor composition elements – i.e. those whose energy contribution is not significant to the structure of the star. This part of the code has been left derelict for many

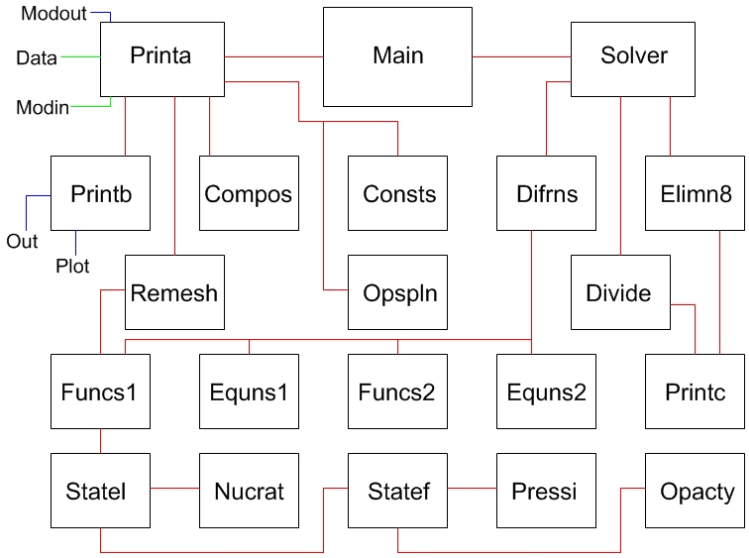

Figure 2.1: Schematic depiction of the connections of the various subroutines in the STARS code. Input files are connected in green; output files are connected in blue.

years but has now been resurrected. Its details are given in Chapter 5.

Both the structural evolution and minor element composition loops of the code utilize a common set of routines for solving for the changes at a given timestep. These routines are `difrns.f`, `solver.f`, `elimn8.f` and `divide.f`. The first sets up the matrix of the difference equations that needs to be inverted in order to determine the changes required at that timestep. The routine `solver.f` has several functions. It controls the inversion of the matrix created by `difrns.f`, which is solved by Gaussian elimination, with `divide.f` and `elimn8.f` being called as appropriate. It also controls the Newton-Raphson iteration process used to converge the desired solution, and tests whether the new solution is within acceptable error limits.

In addition to these a set of routines for writing output from the code exists. These are `printa.f`, `printb.f` and `printc.f`. The first reads in model and physics input data as well as the instructions for the given model run and writes out full models for subsequent use. This routine is also responsible for controlling the timestep used when converging each model (see 2.4.3 below). The routine `printb.f` outputs detailed, human-readable physical models and data useful for plotting purposes. The last routine is used for debugging purposes. There is also a routine `remesh.f` that is called at the

beginning of each new run to set the given model up on the desired mesh.

2.4 Numerical Instability

The bane of the existence of anyone involved in calculating models of stellar evolution is numerical instability. It is a catch-all term used to describe why models fail to work for whatever reason[2]. The TP-AGB is a particularly unforgiving place to be working and some modifications to deal with numerical problems are necessary.

2.4.1 Mixing

During a thermal pulse a star has two separate convective zones active. Strong convection and convective mixing takes place in the intershell due to the intense burning taking place in the He-shell. In the envelope much weaker convection and convective mixing takes place. In order to get accurate results the mixing should be as close to the value predicted by mixing-length theory (Böhm-Vitense, 1958) as possible. However, it is also important that the model being calculated converges! In a trade-off between these two goals, a value of the mixing coefficient that gives a uniform composition in fully convective regions of the star is chosen.

Because the intershell convection is so much stronger, it is possible to choose a smaller value for the mixing diffusion coefficient than is used in the envelope and still satisfy the requirement that the composition be uniform across the convective region. The use of a smaller mixing diffusion coefficient greatly aids numerical stability. Pols & Tout (2001) found it useful to express the mixing diffusion coefficient D as

$$D = D_{\rm MLT}\frac{\beta W}{1-(1-\beta)W} \tag{2.14}$$

with

$$W \equiv \frac{\bigtriangledown_{\rm r} - \bigtriangledown_{\rm ad}}{\bigtriangledown_{\rm r}},$$

and $D_{\rm MLT} = \frac{1}{3}vl$ with v and l the mean velocity and mean free path of convective eddies. The value of β was treated as a free parameter and allowed

[2]The term does have a precise mathematical meaning other than that used here.

to take on different values in the H-rich envelope and in the H-free intershell region and core. A value of $\beta \gg 1$ gives the full mixing length diffusion coefficient. In this work, $\beta = 1$ is used in the H-rich envelope while $\beta = 5 \times 10^{-5}$ in the H-exhausted regions. The H-rich region is defined as the region in which the hydrogen mass fraction exceeds 10^{-6}.

2.4.2 Viscous Mesh

At short timesteps, such as those required to resolve the peak helium luminosity of a thermal pulse, there is a numerical instability associated with the luminosity equation

$$L_{k+1} - L_k = (m'E_1)_{k+\frac{1}{2}} + (m'E_2)_k[\dot{m}_k] - (m'E_2)_{k+1}[-\dot{m}_{k+1}] \qquad (2.15)$$

where L_k is the luminosity at mesh point number k. The change in mass with mesh point is denoted $m' = dm/dk$. Square brackets signify a term only included when it is positive. The first term containing E_1 is related to the usual energy generation terms but evaluated at constant mesh point and the terms containing E_2 are an upstream approximation for the advection term owing to the adaptation of the mesh. When the timestep becomes small these terms become large and this leads to numerical instability when two large numbers are subtracted to give a small result.

To deal with this the mesh can be fixed in mass and so eliminate the last two terms of the above equation. However, it is not desirable to fix the entire mesh because the outer regions do not cause the same problems as the inner ones and the mesh need only be fixed at small timesteps. This causes a second problem – how can the fully adaptive behaviour be recovered after using the fixed mesh? The mesh cannot just be instantaneously returned to a fully adaptive state because, during the fixed phase, mesh points drift away from where the mesh spacing function would place them. Rather, the mesh must be returned to a fully adaptive state gradually and so the idea of a viscous mesh has been developed.

The viscous mesh combines fixed and adaptive behaviours. A weighting coefficient γ, a function of mesh point number and the timestep size, is used to determine the nature of the mesh. In problematic areas the mesh is gradually fixed by increasing the value of γ. If $\gamma = 1$ a mesh point is fully

fixed in mass while if $\gamma = 0$ the point is fully adaptive. This is implemented by solving

$$\left(\left(\frac{dQ}{dk}\right)_{k+1} - \left(\frac{dQ}{dk}\right)_{k}\right)(1-\gamma) + \gamma\left(\frac{dm}{dt}\right)_{k} = 0 \tag{2.16}$$

alongside the equations of stellar structure and composition. The weighting coefficient γ is chosen to be a function of the timestep with γ becoming unity for timesteps of 10^{-4} yr and below for the central mesh points. First it is necessary to evaluate the expression

$$\chi = \frac{3}{4}\left(\frac{\Delta t}{10^{-4}} - 1\right), \tag{2.17}$$

where Δt is the timestep in years. If this is greater than zero, this value is taken; otherwise $\chi = 0$ is used. The next step is to evaluate

$$\psi = \exp(-\sqrt{\chi}) \tag{2.18}$$

and thus obtain a number between 0 and 1 that can be used as the weighting coefficient γ.

It is also necessary that the mesh vary smoothly with mesh point number. If the mesh is fixed with a sharp edge it is possible that the adaptive part of the mesh can move mesh points (in terms of their location in mass) into the region that is fixed. This means that the mass co-ordinate ceases to be a monotonically decreasing function of the mesh point number – something that is assumed in the set-up of the code's equations. With a mesh that has a smooth transition between fixed and adaptive regions the points in the transition region act as a buffer and prevent this from occurring. This is implemented in the code as

$$\gamma = \psi\left[\frac{1}{2} + \frac{1}{2}\tanh\left(\frac{k - k_{\rm trans}}{1.5}\right)\right], \tag{2.19}$$

where k is the mesh point number and $k_{\rm trans}$ is the mesh point number up to which fixed behaviour is desired. With such a form for γ the viscous mesh has the desired properties. Typically $k_{\rm trans} = 900$ in the 999 mesh point models calculated in this work.

2.4.3 Timestep Control

The STARS code attempts to choose the most appropriate timestep size based on the changes to the variables of the previous model required to produce the current model. This is done within the routine `printa.f`. A sum of the absolute values of these changes (excluding those made to the luminosity) is made over all variables and over all mesh points producing a single numerical value

$$d = \Sigma_i \Sigma_k |x_{i,k}|,$$

where $x_{i,k}$ are the values of the changes made to each variable i at a given mesh point k. Usually the value of d is dominated by the temperature and the degeneracy. This is then compared to a preset optimum value $d_{\rm opt}$. If $d_{\rm opt}/d$ is greater than one the timestep is increased by this fraction or 1.2, whichever is smaller. If $d_{\rm opt}/d$ is less than one the timestep is reduced by this fraction or 0.8, whichever is larger. In this way an appropriate timestep is chosen for the next model.

The value chosen for $d_{\rm opt}$ depends on the number of mesh points in the model. For a 999 mesh point model, a value of 5 is typically chosen. However, if it is desirable to have smaller timesteps, lower values are used. In order to deal with the range of timescales involved in TP-AGB evolution it may become necessary to change the value of $d_{\rm opt}$ at certain stages of the evolution.

As the helium burning luminosity begins to rise $d_{\rm opt}$ is set to 0.5. This gives the code opportunity to respond to the changes that occur at the onset of a thermal pulse. As the peak of a thermal pulse is approached the timestep drops to about 2×10^{-5} yr. To avoid numerical problems inherent at lower timesteps the timestep is prevented from dropping below 10^{-5} yr. When the helium luminosity begins to decline after the peak of the thermal pulse the intershell convection zone (ICZ) shuts down and the convective envelope of the star moves inward. During this phase $d_{\rm opt}$ is returned to 5. As the envelope reaches down into the region where the ICZ was active it begins to dredge-up the products of helium burning. At this point it is necessary to limit the size of the changes being made to the variables to avoid numerical instability.

An algorithm has been written that records the position of the boundary of the ICZ at its maximum outward extent. This is then compared to the location of the boundary of the convective envelope. When the envelope

reaches into the region where the ICZ was active the value of $d_{\rm opt}$ is set to 1. This limits the timestep to the order of a few days. When the helium luminosity reaches as low as $3 \times 10^3\,{\rm L}_\odot$ and TDUP is over $d_{\rm opt}$ is restored to 5.

2.5 Making Stellar Models

In all cases models are started on the pre-main sequence with a gas cloud that has a temperature of less than $10^6\,{\rm K}$ throughout. This is because the STARS code does not consider any nuclear burning to occur below this temperature. Initially, 199 mesh points are used and throughout the evolution the mixing length parameter is set to $\alpha = 1.925$ based on a calibration to a solar model. Unless otherwise stated, no mass loss has been considered in these models. The model is evolved through the main sequence, up the red giant branch and on to the core helium burning phase. At core helium burning, the resolution is enhanced to 499 mesh points. This is done to facilitate the transition to the higher resolution required on the TP-AGB. At the end of the early AGB (E-AGB) the model is remeshed with 999 mesh points. The full form of the mesh spacing function, as given in Equation 2.12, is used and the above modifications to deal with numerical instability are activated at this point.

This method can be used for stars of above around $2.3\,{\rm M}_\odot$ because these stars do not undergo a core helium flash at the tip of the red giant branch. The core helium flash is a numerically demanding phase of evolution and the STARS code is currently not suitable for a calculation of the evolution through it[3]. Instead a model of the desired mass is run from the pre-main sequence up to the helium flash. The hydrogen exhausted core mass and the envelope composition are recorded. A $3\,{\rm M}_\odot$ model is then evolved from the pre-main sequence up to the point where helium ignites in the core. During this evolution helium burning reactions are allowed to produce energy but not consume helium. Once helium has ignited under non-degenerate conditions mass is stripped from the envelope and the core is allowed to grow until the model has the desired envelope mass and core mass. The envelope composition is then set to that of the pre-flash model. It is therefore

[3]The author spent much of the first year of his Ph.D. trying to get through the He-flash but to no avail.

being assumed that the helium flash proceeds so rapidly that the core mass doesn't change and that there is no change in the envelope composition. These are both standard assumptions. Because the helium flash is bypassed, the possibility that the post-flash models are not consistent must be accepted and these models should be treated with a degree of caution. This method has been used to create the models presented in the following chapters.

Chapter 3

TP-AGB Stars of Solar Metallicity

In this chapter the results of evolution calculations of TP-AGB stars of between 1 and 7 $\mathrm{M}_{\odot}$ of initially solar metallicity (i.e. $Z = 0.02$) and composition are presented. The initial abundances of the elements required for starting these calculations are taken from Anders & Grevesse (1989). The absence of mass loss in these calculations means that the sequences have no natural termination point[1] and in each case some insurmountable numerical difficulty brings the evolution to a halt. In all but one case the evolution has been followed far enough that further calculations are unnecessary.

3.1 Initial Attempt – a 5 $\mathrm{M}_{\odot}$ star

The first run with the new code was done on a $5\,\mathrm{M}_{\odot}$ star as it was this mass of star that Pols & Tout (2001) did their work on. The evolution was followed through a total of 60 thermal pulses. Full details of the model can be found in Appendix B. The sequence was terminated at this point because, without mass-loss, it would not reach a natural end-point. The evolution of the helium luminosity is shown in Figure 3.1. The model reaches a maximum thermal pulse strength of $\log L_{\mathrm{He}}/\,\mathrm{L}_{\odot} = 9.356$ at pulse 20. The interpulse helium luminosity initially decreases but after around 10^5 years it begins to

[1] Presumably evolution would continue until the H-shell can no longer sustain burning or a degenerate core exceeding the Chandrasekhar mass is obtained. Both cases would take hundreds of pulses and it is not feasible to follow this evolution within the timescale of a standard Ph.D.

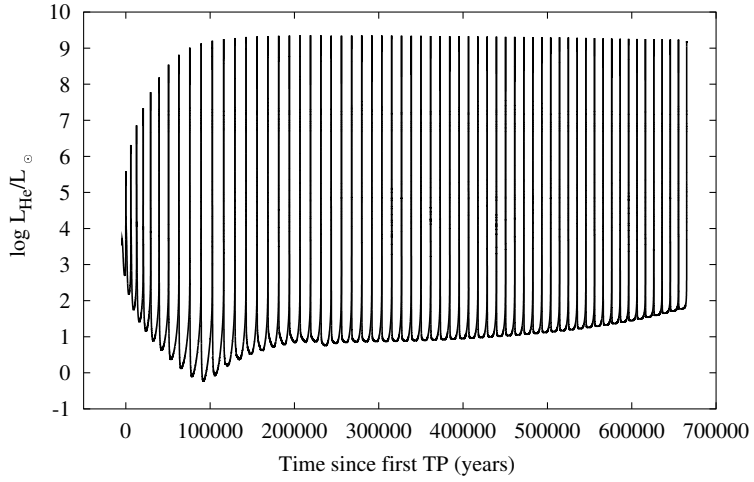

Figure 3.1: Plot of the evolution of the helium luminosity of the $5\,M_{\odot}$ model.

increase again.

The evolution of the H- and He-exhausted core masses are displayed in Figure 3.2 and the evolution of the surface CNO abundances are displayed in Figure 3.3. TDUP starts to occur by the second pulse and rapidly becomes very efficient with λ[2] exceeding unity by pulse 5. It remains so for 5 pulses. The efficiency of TDUP then drops slightly and the core begins to grow in mass. The initial episodes of TDUP slightly enhance the surface carbon abundance, but the efficient TDUP means that HBB begins to occur after only about five pulses and this rapidly depletes the carbon abundance, whilst significantly boosting that of nitrogen. HBB is sufficiently hot to cause a noticeable depletion in the oxygen abundance.

The calculations presented here go significantly further than those of Pols & Tout (2001) who calculated a total of six thermal pulses for their $5\,M_{\odot}$ $Z = 0.02$ model. The early pulses of the model presented here display the same behaviour as those of this earlier work. This, together with the length of the run, demonstrates that the new code works and so it may be applied to other stellar masses with confidence. The results of these calculations are detailed below.

[2]The efficiency of third dredge-up is defined by $\lambda = \Delta M_{\rm TDUP}/\Delta M_{\rm c}$, where $\Delta M_{\rm c}$ is the amount by which the H-exhausted core grows in the preceding interpulse phase and $\Delta M_{\rm TDUP}$ is the amount of material dredged up.

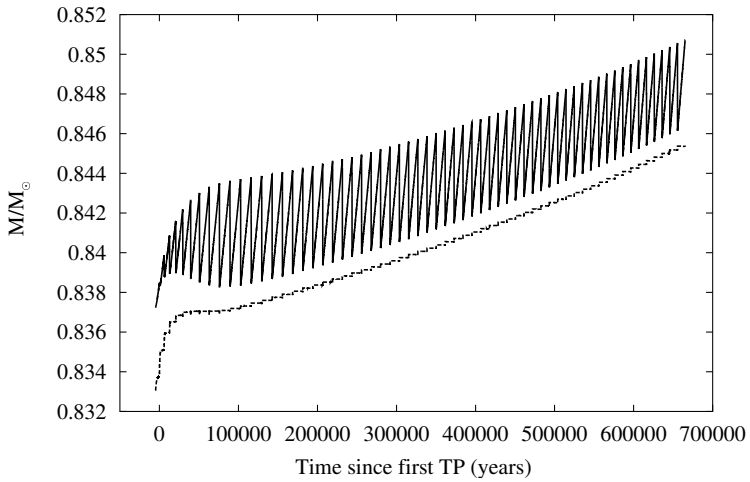

Figure 3.2: Plot of the evolution of the H-exhausted (solid line) and He-exhausted (dotted line) core masses of the 5 $M_\odot$ model.

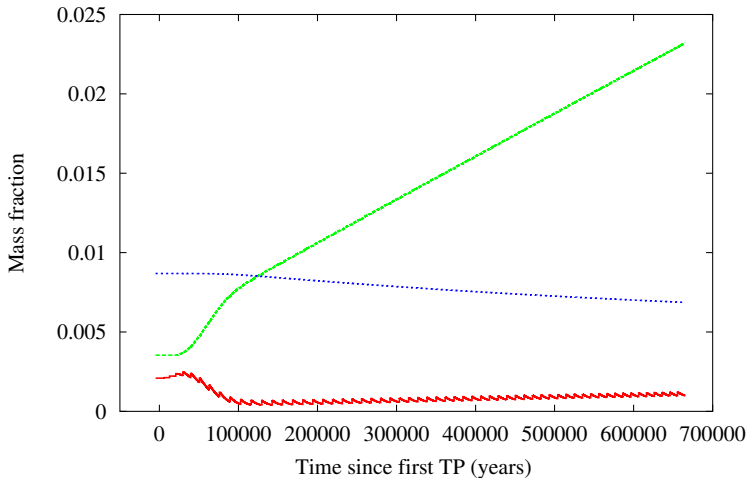

Figure 3.3: Plot of the evolution of the surface abundances of carbon (solid red line), nitrogen (dashed green line) and oxygen (dotted blue line) for the 5 $M_\odot$ model.

Mass ($M_\odot$)	No. TPs	M_{1TP}($M_\odot$)	TDUP?	M_{TDUP} ($M_\odot$)	λ_{max}	HBB?
1	6	0.54166	No	-	-	No
1.5	13	0.55666	Yes	0.58335	0.427	No
2	16	0.56786	Yes	0.57605	0.791	No
3	20	0.56351	Yes	0.57862	0.902	No
4	21	0.75332	Yes	0.75960	1.034	Yes
5	60	0.83723	Yes	0.83723	1.048	Yes
6	40	0.89346	Yes	0.89665	1.036	Yes
7	23	0.99440	Yes	0.99470	1.005	Yes

Table 3.1: General properties of the $Z = 0.02$ models. The mass of the H-exhausted core at which a thermal pulse first occurs is M_{1TP}. The mass of the H-exhausted core at which TDUP first occurs is M_{TDUP}. The maximum efficiency of TDUP (see main text for a definition of dredge-up efficiency) is λ_{max}. The final column lists whether the star experiences hot-bottom burning (HBB) or not.

3.2 General Properties

The general properties of the models are first reviewed. An overview of these characteristics is presented in Table 3.1. Of all the models only the $1\,M_\odot$ does not show third dredge-up. Only 6 pulses were calculated so the question of whether this model should undergo TDUP or not cannot be assessed. Defining the efficiency of third dredge-up as $\lambda = \Delta M_{TDUP}/\Delta M_c$, where ΔM_c is the amount by which the H-exhausted core grows in the preceding interpulse phase and ΔM_{TDUP} is the amount of material dredged up, it should be noted that TDUP is very efficient in most of the models and exceeds unity for stars of $4\,M_\odot$ or heavier. It should be noted that because the sequences are all terminated due to numerical issues, in the low-mass cases the value of λ_{max} quoted in Table 3.1 may not represent the actual maximum efficiency that the model could reach if it were evolved far enough. Hot-bottom burning is found to occur in all the models of $4\,M_\odot$ and above.

3.3 Model-by-model

A detailed look at the models of different mass that have been generated is presented, focusing on the evolution of the helium luminosity, H- and He-exhausted core masses and evolution of the abundances of the CNO elements

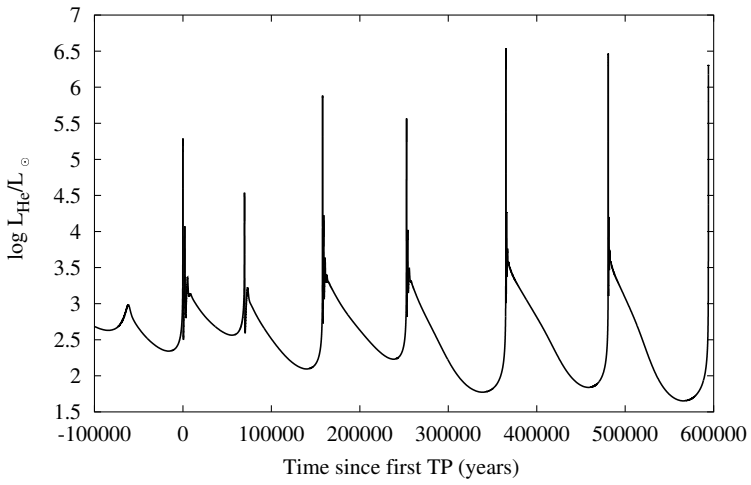

Figure 3.4: Plot of the evolution of the helium luminosity of the $1\,\mathrm{M}_\odot$ model.

at the surface of the star. Further details are presented in Appendix B.

3.3.1 $1\,\mathrm{M}_\odot$

In many respects this is the most disappointing model of all those created in this work. At a solar mass it represents a prediction of what will happen to our own Sun. It is therefore unfortunate that only 6 thermal pulses could be calculated before the model broke down. The reason for the breakdown is unclear but it appears that the code has difficulty converging changes that are occurring in the envelope of the star as it approaches the peak of a thermal pulse. It is also unfortunate that the model breaks down before there is any sign of third dredge-up. To date, no-one has found TDUP in such a model and it would have been interesting to see if the STARS code would have confirmed or contradicted this result.

Figure 3.4 shows the evolution of the helium luminosity. With only a few thermal pulses calculated the model has evidently not reached any sort of equilibrium. Note also that there is variation in the strength from pulse-to-pulse in the first few pulses. The pulse strength is not monotonically increasing. In addition the helium luminosity during the interpulse phase is also much higher prior to the weaker pulses. The strongest pulse has a helium luminosity of $\log L_{\mathrm{He}}/\,\mathrm{L}_\odot = 6.5$. A plot of the evolution of the H-

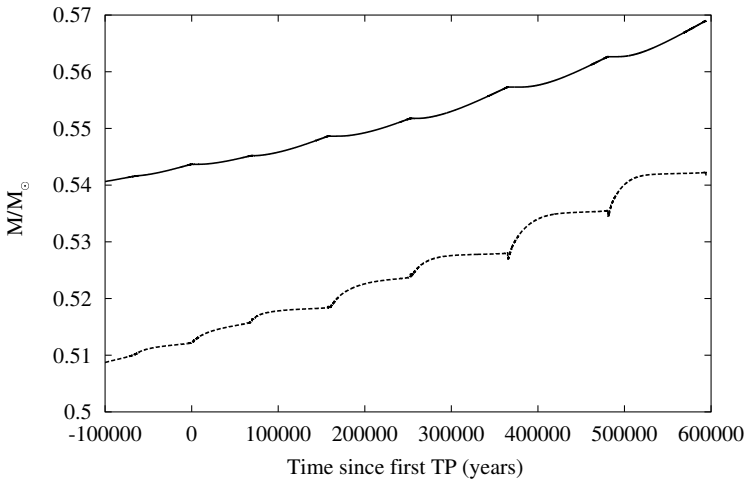

Figure 3.5: Plot of the evolution of the H-exhausted (solid line) and He-exhausted (dotted line) core masses of the $1\,M_\odot$ model.

and He-exhausted core masses is shown in Figure 3.5. The H-exhausted core mass starts out at around $0.54\,M_\odot$ and steadily grows to around $0.57\,M_\odot$ after the last calculated pulse. The He-exhausted core mass starts off at around $0.51\,M_\odot$ and grows to around $0.54\,M_\odot$ with its growth becoming more rapid in the later stages. Because no dredge-up occurs during the calculated phase the surface composition is unchanged from when the star first began its thermal pulses and retains the abundances it obtained during first dredge-up. The mass fractions of carbon, nitrogen and oxygen at the surface are $2.18 \times 10^{-3}, 2.98 \times 10^{-3}$ and 9.21×10^{-3} respectively.

3.3.2 1.5 $M_\odot$

A total of 13 thermal pulses have been evolved for this model. The evolution of the helium luminosity as a function of time since the first thermal pulse is shown in Figure 3.6. The peak luminosity at each pulse increases monotonically and has reached a value of $\log L_{\rm He}/\,L_\odot = 7.67$ at the last full pulse calculated. The model run does not appear to have reached an equilibrium phase by the time the model suffered insurmountable numerical difficulty as the peak helium luminosities seem to be increasing with each pulse. In addition the helium luminosity in the interpulse phase seems to be continually decreasing with each pulse.

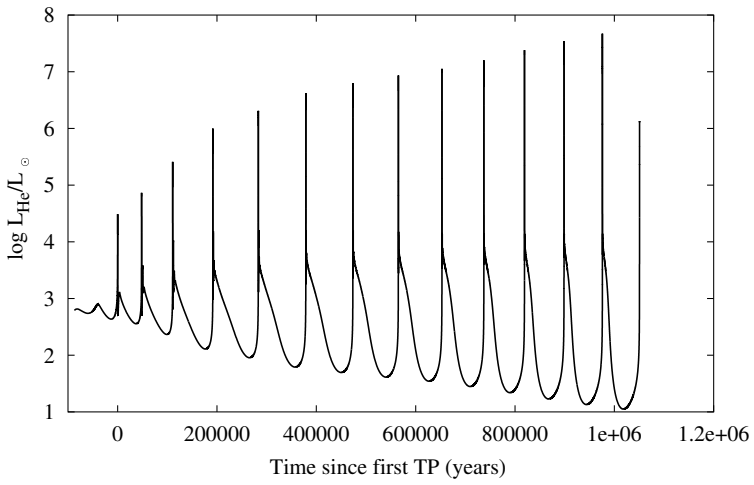

Figure 3.6: Plot of the evolution of the helium luminosity of the $1.5\,M_\odot$ model.

A plot of the evolution of the H- and He-exhausted core masses is shown in Figure 3.7. The H-exhausted core mass starts off at around $0.56\,M_\odot$ but its rate of growth is retarded by the onset of third dredge-up after the 9^{th} thermal pulse after around 6×10^5 years since the first pulse. The effect of the onset of TDUP is manifested in the surface abundances, shown in Figure 3.8. The abundance of carbon begins to increase rapidly and the increase becomes more rapid as the dredge-up becomes deeper with each subsequent pulse. There is also a slight increase in the oxygen abundance. Both of these are expected because the helium intershell is rich in the products of He-burning. This model would be expected to continue dredging up and would eventually become a carbon star, with a surface C/O ratio (by number, not mass fraction) greater than unity.

3.3.3 2 $M_\odot$

A total of 16 thermal pulses have been evolved for this model. The evolution of the helium luminosity is shown in Figure 3.9. In a similar way to the $1.5\,M_\odot$ model, the peak luminosity increases from pulse to pulse whilst the interpulse helium luminosity steadily declines. The core of this model is more massive than that of the $1.5\,M_\odot$ model and so the helium luminosity peaks at a much higher value. By the time the model sequence breaks down the

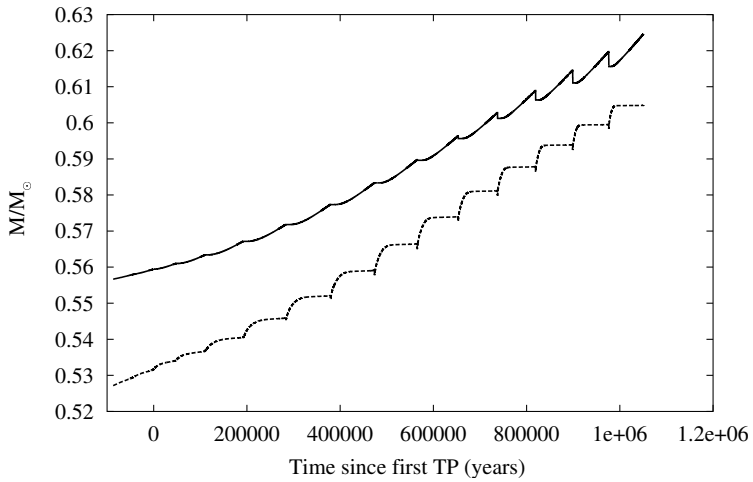

Figure 3.7: Plot of the evolution of the H-exhausted (solid line) and He-exhausted (dotted line) core masses of the $1.5\,M_{\odot}$ model.

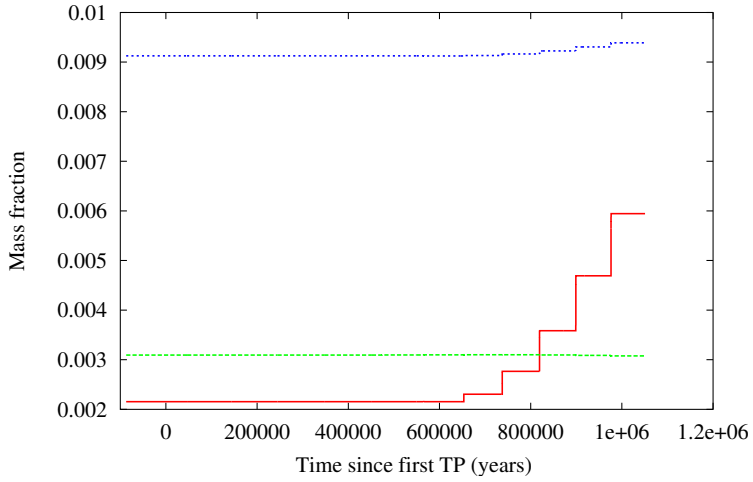

Figure 3.8: Plot of the evolution of the surface abundances of carbon (solid red line), nitrogen (dashed green line) and oxygen (dotted blue line) for the $1.5\,M_{\odot}$ model. The model breaks down before a carbon star is formed.

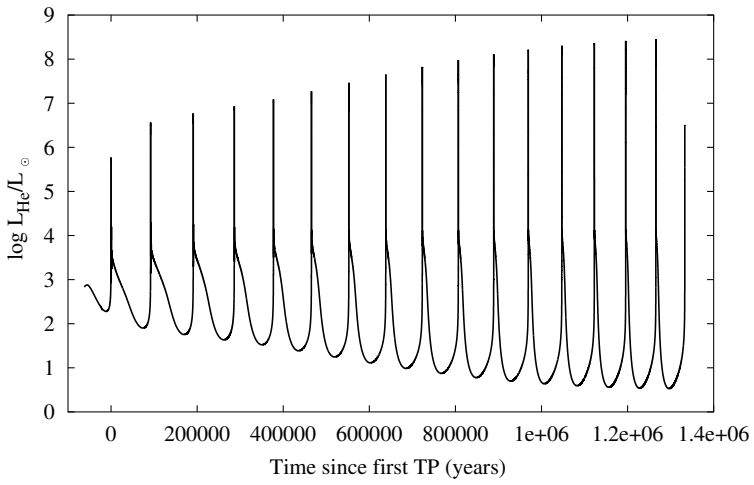

Figure 3.9: Plot of the evolution of the helium luminosity of the $2\,M_{\odot}$ model.

rate of increase of the peak helium luminosity seems to be slowing down.

Another consequence of the larger core mass of this model is that TDUP occurs much sooner. The first instance of dredge-up occurs at around 3×10^5 yrs, as can be seen in Figure 3.10. Unlike the $1.5\,M_{\odot}$ model, dredge-up deepens dramatically with the dredge-up efficiency reaching $\lambda = 0.791$ on the last calculated pulse. This deep dredge-up prevents the H-exhausted core from growing much over the course of the calculation.

The occurrence of TDUP once again causes enrichment of the envelope and enhances the surface abundances of carbon and oxygen. Whilst the dredge-up is deeper in this model than in the $1.5\,M_{\odot}$ case, the surface abundances do not change as rapidly. This is because this model has a much larger envelope than the previous one and the dredged-up material is mixed with the whole envelope. The repeated action of TDUP leads to the formation of a carbon star at a time of approximately 9×10^5 yrs after the first thermal pulse.

3.3.4 $3\,M_{\odot}$

The $3\,M_{\odot}$ model displays the same trends as the $2\,M_{\odot}$. A total of 20 pulses have been evolved and by the later phases it appears as if the pulse strength is reaching a limiting value as shown in Figure 3.12. The last pulse calculated

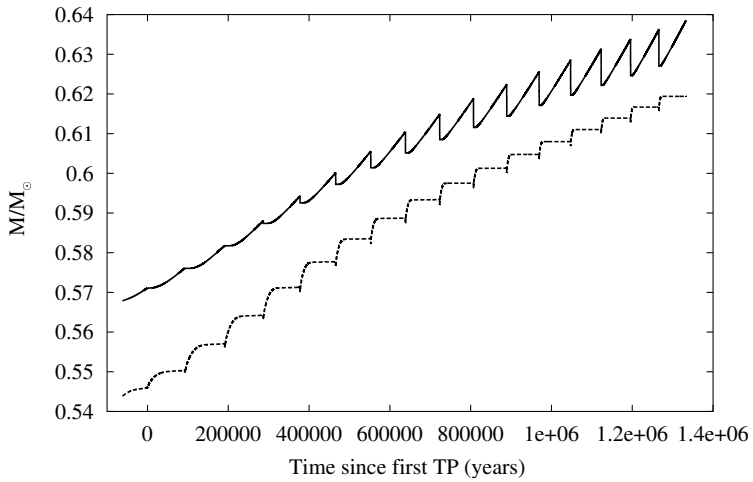

Figure 3.10: Plot of the evolution of the H-exhausted (solid line) and He-exhausted (dotted line) core masses of the $2\,M_{\odot}$ model.

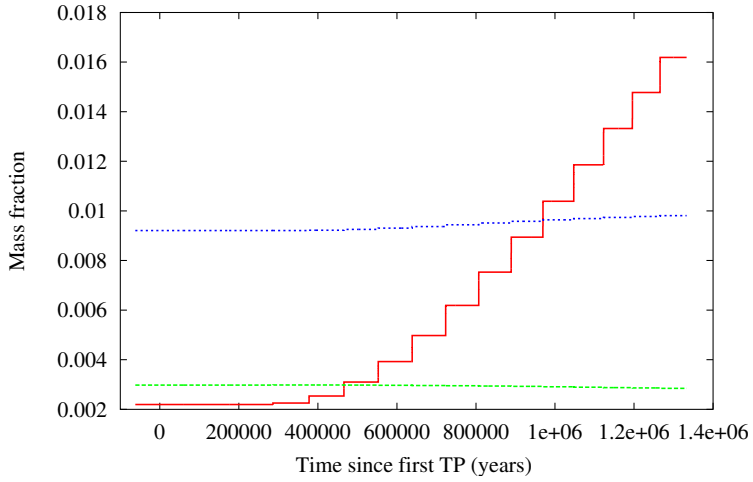

Figure 3.11: Plot of the evolution of the surface abundances of carbon (solid red line), nitrogen (dashed green line) and oxygen (dotted blue line) for the $2\,M_{\odot}$ model.

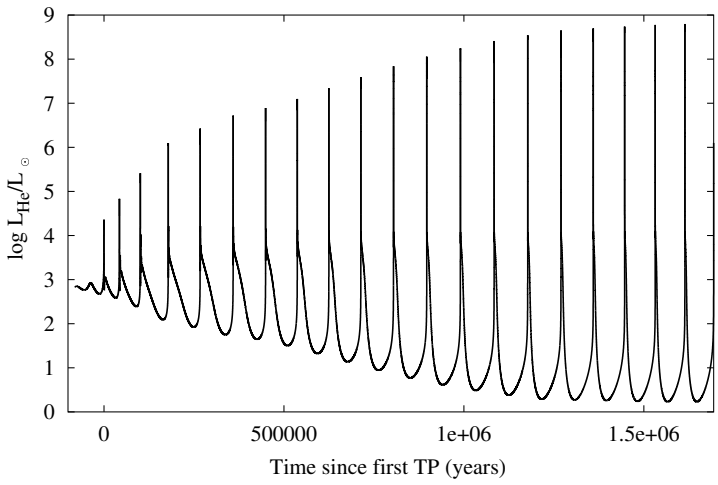

Figure 3.12: Plot of the evolution of the helium luminosity of the $3\,\mathrm{M}_\odot$ model.

reaches $\log L_{\mathrm{He}}/\,\mathrm{L}_\odot = 8.80$. Also the interpulse helium luminosities seem to be reaching a minimum value as well.

This model also displays TDUP which begins to occur at a little before 5×10^5 years as can be seen in Figure 3.13. Dredge-up is more efficient than in the case of the $2\,\mathrm{M}_\odot$ model, reaches a maximum efficiency of $\lambda = 0.902$, and sets in at a slightly higher core mass. The effect of TDUP on the surface composition can be seen in Figure 3.14. A carbon star is finally formed at around 1.2×10^6 years after the first thermal pulse. The additional mass in the envelope slows down the formation of a carbon star because even more material needs to be dredged-up to enrich the envelope.

3.3.5 $4\,\mathrm{M}_\odot$

The $4\,\mathrm{M}_\odot$ model displays different behaviour to the lower masses. The evolution of its helium luminosity is shown in Figure 3.15. Like the lower-mass models it appears to have reached a limiting strength for the peaks of its pulses, namely $\log L_{\mathrm{He}}/\,\mathrm{L}_\odot = 9.56$. Like the lower-mass models the interpulse helium luminosity is first seen to decrease and then after about 3×10^5 years it slowly begins to increase again. This behaviour is not seen in the lower mass models.

A plot of the evolution of the H- and He-exhausted core mass for this

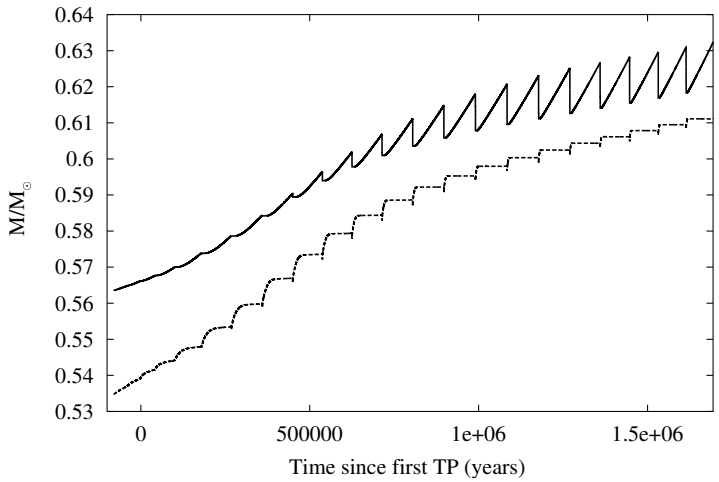

Figure 3.13: Plot of the evolution of the H-exhausted (solid line) and He-exhausted (dotted line) core masses of the $3\,M_{\odot}$ model.

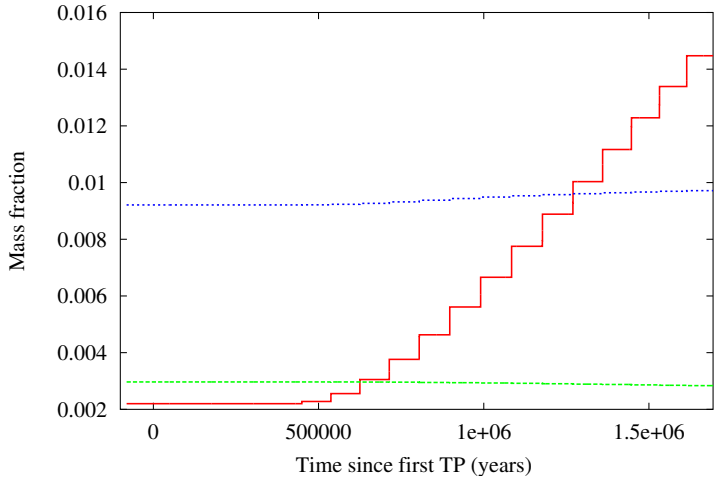

Figure 3.14: Plot of the evolution of the surface abundances of carbon (solid red line), nitrogen (dashed green line) and oxygen (dotted blue line) for the $3\,M_{\odot}$ model.

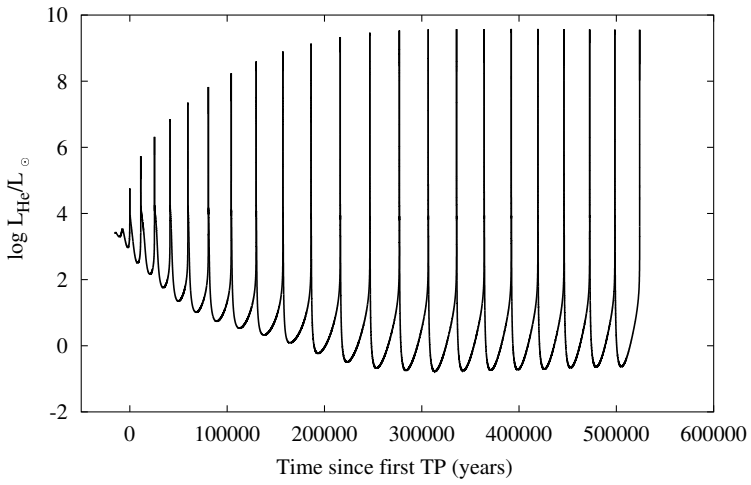

Figure 3.15: Plot of the evolution of the helium luminosity of the $4\,M_{\odot}$ model.

model is shown in Figure 3.16. Note that TDUP sets in very quickly, starting by just the third pulse. TDUP also becomes very efficient with λ exceeding unity. This has the effect of inhibiting the growth of the He-exhausted core. Between 10^5 and 2.5×10^5 years, when TDUP is at its most efficient, the He-exhausted core mass barely grows.

The evolution of the surface abundance of the CNO elements (Figure 3.17) also displays behaviour not seen in the lower mass models. Initially the action of TDUP is seen to increase the abundance of carbon at the surface of the model, just as it does in all the low-mass models. However, by the 10^{th} pulse with TDUP, the carbon abundance begins to decline in the interpulse period. The decline increases in severity with each subsequent pulse and by the time the model breaks down more carbon is being destroyed in the interpulse than is brought to the surface by TDUP. At the same time the nitrogen abundance is steadily being enhanced. This is a clear signature that HBB is active in this model. It has become a carbon star (i.e. its C/O ratio *by number* is greater than unity) but the action of HBB means it does not remain that way.

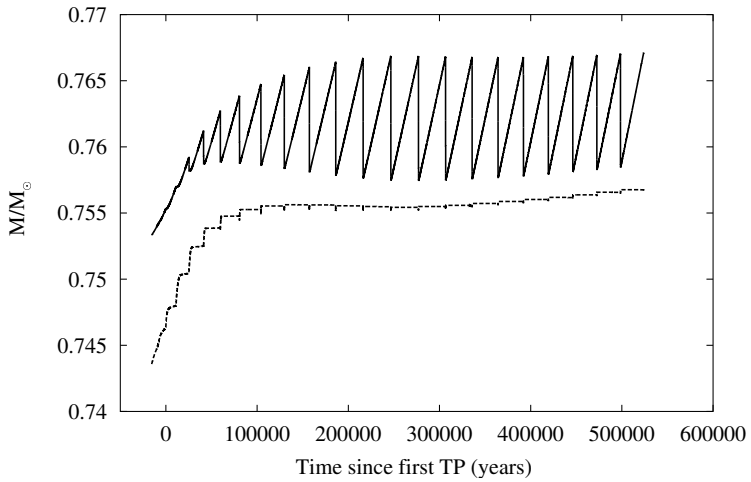

Figure 3.16: Plot of the evolution of the H-exhausted (solid line) and He-exhausted (dotted line) core masses of the $4\,M_{\odot}$ model.

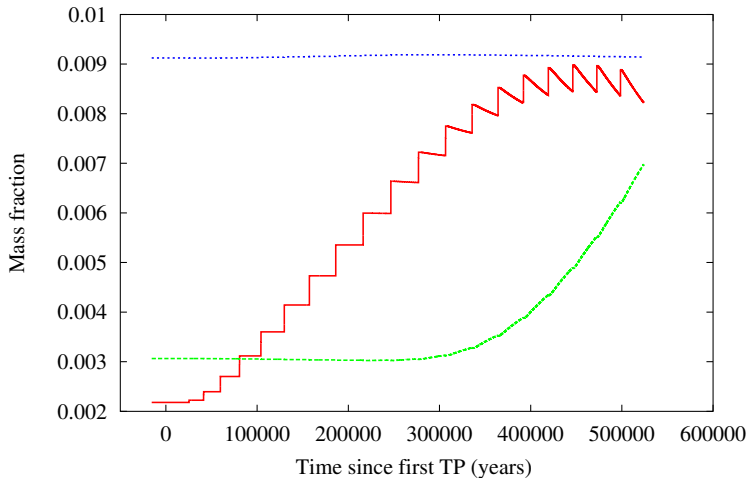

Figure 3.17: Plot of the evolution of the surface abundances of carbon (solid red line), nitrogen (dashed green line) and oxygen (dotted blue line) for the $4\,M_{\odot}$ model.

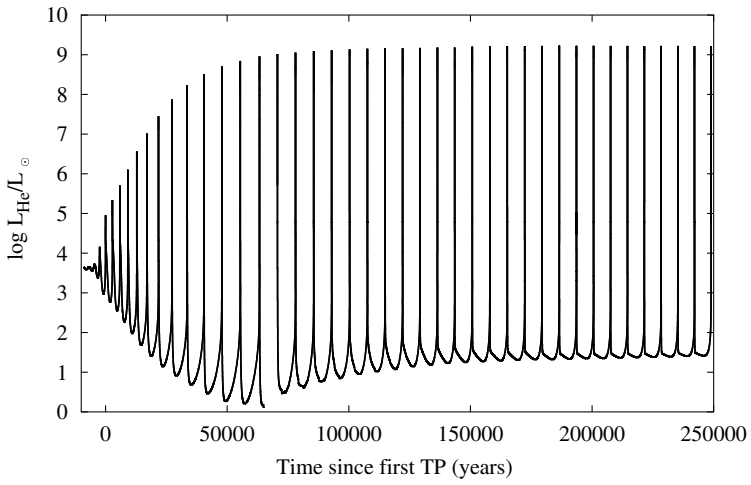

Figure 3.18: Plot of the evolution of the helium luminosity of the $6\,M_{\odot}$ model. Note that the break just after 5×10^5 years is due to a corrupted datafile.

3.3.6 6 $M_{\odot}$

The properties of the $6\,M_{\odot}$ model are very similar to those of the $5\,M_{\odot}$ one. However, the evolution of the helium luminosity of the $6\,M_{\odot}$ model (shown in Figure 3.18) shows slightly less intense thermal pulses and the build-up to maximum intensity takes more pulses. The model displays the same pattern of behaviour for the interpulse luminosity, namely a decrease towards some minimum followed by an increase.

In terms of the behaviour of the core masses (Figure 3.19) and surface CNO abundances (Figure 3.20), the model is almost identical to the $5\,M_{\odot}$ one. TDUP occurs after the second pulse and becomes extremely efficient just as it did in the $5\,M_{\odot}$ case. The efficiency then reduces slightly and the core begins to grow. As with the $5\,M_{\odot}$ model, HBB sets in very quickly due to the efficient dredge-up and the model is soon nitrogen-enhanced and carbon poor. HBB occurs at a higher temperature in this model and the oxygen abundance is depleted more rapidly.

3.3.7 7 $M_{\odot}$

The $7\,M_{\odot}$ model continues the trends observed in the $6\,M_{\odot}$ model. The helium luminosity (Figure 3.21) evolves towards a lower peak intensity than

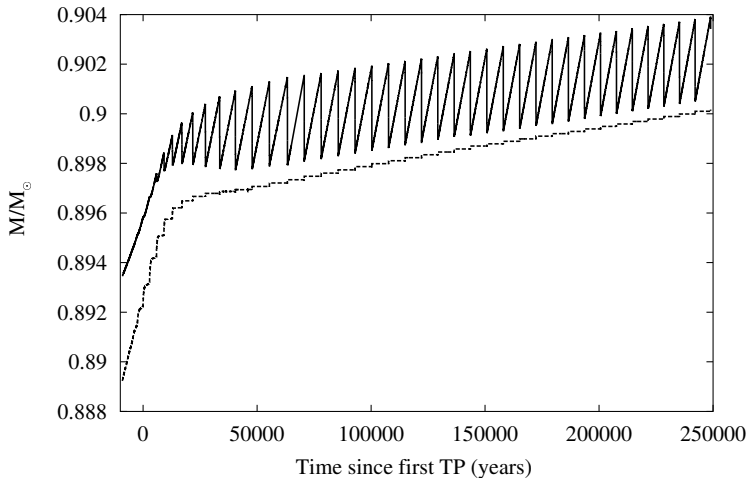

Figure 3.19: Plot of the evolution of the H-exhausted (solid line) and He-exhausted (dotted line) core masses of the $6\,M_{\odot}$ model.

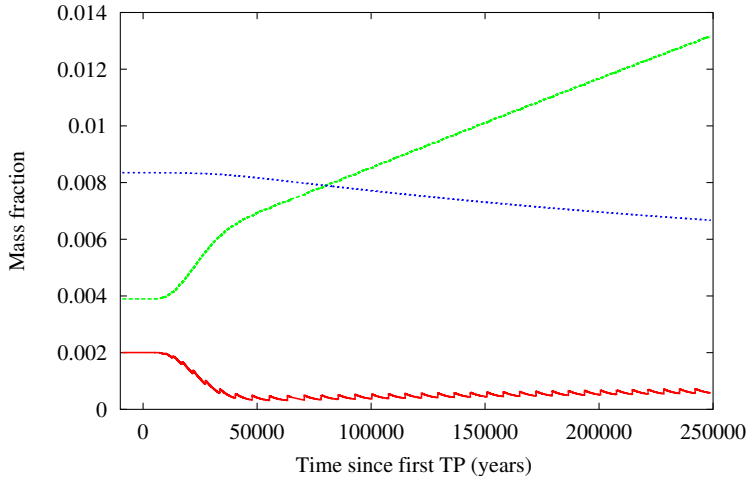

Figure 3.20: Plot of the evolution of the surface abundances of carbon (solid red line), nitrogen (dashed green line) and oxygen (dotted blue line) for the $6\,M_{\odot}$ model.

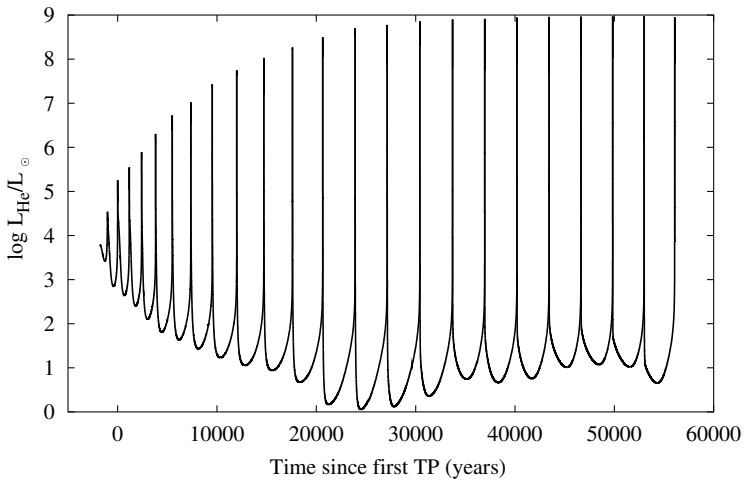

Figure 3.21: Plot of the evolution of the helium luminosity of the 7 $M_{\odot}$ model.

the 6 $M_{\odot}$ model and its evolution towards this peak also takes more pulses. The behaviour of the core masses (Figure 3.22) is comparable to that found in the 5 and 6 $M_{\odot}$ models. The abundance of the surface CNO elements displays a slightly different behaviour as can be seen in Figure 3.23. Unlike the 5 and 6 $M_{\odot}$ models, where HBB sets in after a few thermal pulses, the carbon abundance is already decreasing and the nitrogen abundance is increasing before thermal pulses start to occur. Second dredge-up is sufficiently deep to permit CNO-cycling to occur before thermal pulses start.

3.4 Model Comparisons

Many models of TP-AGB stars have been presented in the literature. It is therefore possible to make a detailed comparison of the models presented here with those made with other codes.

Karakas et al. (2002) have calculated a grid of stellar models at solar metallicity for the mass range investigated above. These calculations were made with the Mount Stromlo Stellar Structure Program (MSSSP). Details are presented in Table 3.2. Comparing this data with that presented in Table 3.1 we find similar trends. In both cases the efficiency of TDUP initially increases with increasing mass before reaching a maximum value and then it decreases again. In the case of the MSSSP models, this turnover occurs at

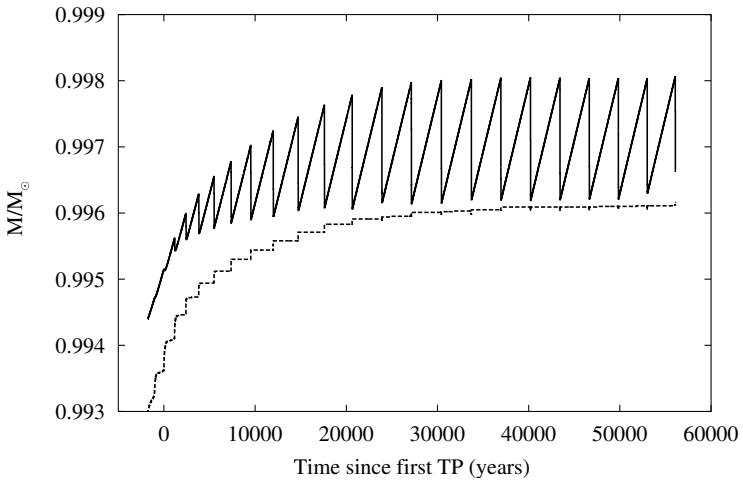

Figure 3.22: Plot of the evolution of the H-exhausted (solid line) and He-exhausted (dotted line) core masses of the $7\,M_{\odot}$ model.

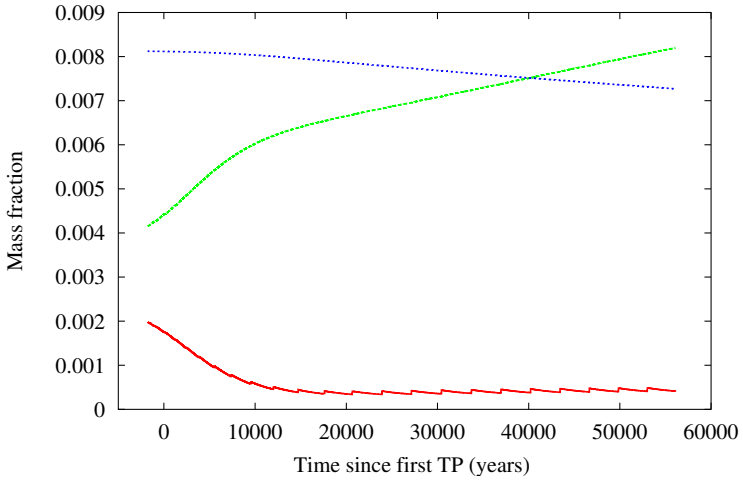

Figure 3.23: Plot of the evolution of the surface abundances of carbon (solid red line), nitrogen (dashed green line) and oxygen (dotted blue line) for the $7\,M_{\odot}$ model.

Mass ($M_\odot$)	M_{1TP} ($M_\odot$)	M_{TDUP} ($M_\odot$)	λ_{max}
1.5	0.560	0.658	0.0486
2.0	0.554	0.632	0.457
3.0	0.595	0.635	0.790
4.0	0.793	0.799	0.977
5.0	0.862	0.866	0.955
6.0	0.915	0.918	0.922

Table 3.2: Models of metallicity $Z = 0.02$ calculated using the Mount Stromlo Stellar Structure Program, taken from Table 2 of Karakas et al. (2002). M_{1TP} is the mass of the H-exhausted core at the first thermal pulse, M_{TDUP} is the H-exhausted core mass at which TDUP first occurs and λ_{max} is the maximum efficiency of TDUP.

$4\,M_\odot$ whereas the models of this work display a turnover at $5\,M_\odot$. The two sets of models display similar H-exhausted core masses at the first thermal pulse. However, it should be noted that in the case of the low-mass models TDUP begins to occur at a much lower core mass for the models computed with STARS than it does for those computed with MSSSP. This is an interesting result – it has been noted that in order to solve the carbon star mystery (see Section 1.4) dredge-up must occur at lower core masses than has been seen in previous calculations. This issue is discussed in more depth in Chapter 4.

Models of solar metallicity AGB stars have also been computed by Straniero et al. (1997, 2000) using the Frascati Raphson-Newton Evolutionary Code, FRANEC (Chieffi & Straniero, 1989). Models of 1-, 1.5- and $3\,M_\odot$ stars without mass loss are presented in Straniero et al. (1997). The $1\,M_\odot$ model has an H-exhausted core mass of $0.555\,M_\odot$ at the first thermal pulse, which is consistent with the model presented in this work. No TDUP is found to occur and a total of 20 pulses have been calculated. For the $1.5\,M_\odot$ model the core mass at first thermal pulse is $0.562\,M_\odot$ and TDUP occurs when the core mass is $0.625\,M_\odot$. This is significantly higher than the results of this work, but somewhat lower than the MSSSP calculations predict. TDUP reaches a maximum efficiency of $\lambda = 0.3404$ and the maximum luminosity from helium burning is $\log L_{He}/L_\odot = 7.848$. TDUP is less efficient in the FRANEC model, even though the helium luminosity reaches a higher value than in the STARS model. It should be noted, however, that the STARS model

evolution has been terminated prematurely due to numerical instability. In the case of the $3\,M_\odot$ FRANEC model, the core mass at first thermal pulse is $0.572\,M_\odot$ and TDUP begins to occur when the core mass reaches $0.611\,M_\odot$. Again, the former is comparable to the STARS model but dredge-up occurs at a much higher core mass. The FRANEC model gives a maximum dredge-up efficiency of $\lambda = 0.461$ which is significantly less efficient that the STARS model. The STARS model also produces more intense pulses.

The phenomena of deep dredge-up and high peak luminosities are related, as was also found by Straniero et al. (2000). On the one hand, stronger shell flashes cause greater expansion during the power-down phase and thereby allow the convective envelope to reach deeper layers. Conversely, deeper dredge-up leads to a longer interpulse period and greater values of ΔM_H as found in these models (see the tables in Appendix B). Hence a larger reservoir of helium is built up which may cause a larger peak helium luminosity. Another factor that contributes to the more powerful shell flashes is that the longer interpulse period gives the inactive He-burning shell more time to cool and be compressed. Therefore the next shell flash occurs at higher density and more work has to be done to expand the intershell region, i.e. a higher peak luminosity is required. The upshot is that deep dredge-up and powerful shell flashes mutually reinforce each other.

Straniero et al. (2000) have also made models of intermediate mass stars at solar metallicity using the FRANEC code. These have not been presented to the same degree of detail as the lower-mass models but a useful comparison can still be made. Their $5\,M_\odot$ model evolved without mass loss gives dredge-up and reaches a final C/O ratio of 0.9. The maximum temperature at the base of the convective envelope is $4.6 \times 10^7\,K$ which is not hot enough for HBB to occur. In contrast the $5\,M_\odot$ STARS model reaches a temperature of $7.9 \times 10^7\,K$ at the base of the convective envelope and hence a depletion of C via CNO cycling is observed. In the $6\,M_\odot$ model of Straniero et al. (2000), they find a slightly hotter temperature at the base of the convective envelope, namely $6.9 \times 10^7\,K$ which is hot enough for a limited amount of CNO cycling and hence the final C/O ratio of there model is 0.52. In contrast, the STARS $6\,M_\odot$ model experiences very efficient CNO cycling to the extent that the C/O ratio is very low.

3.4.1 Models with Convective Overshooting

It is generally agreed that models produced using only convective mixing do not produce the correct abundance profiles for *s*-process nucleosynthesis to occur. They do not produce a pocket of ^{13}C in the intershell region which is required to provide a neutron source via the reaction ^{13}C(α,n)^{16}O. An additional mixing mechanism is required and no *physical* origin has yet been established. One of the mechanisms that has been proposed is convective overshooting, where blobs of material penetrate into convectively stable regions leading to partial mixing of protons and carbon-rich material.

TP-AGB models with convective overshooting have been published by Herwig (2000). He has calculated the evolution of both 3 and 4 $M_\odot$ stars in which he allows convective elements to penetrate the convectively stable regime with an exponentially decaying velocity. This overshooting is applied at all convective boundaries. These models are evolved with a Reimers' mass-loss law with $\eta = 1$.

Selected details of Herwig's models, taken from Tables 1 and 2 of Herwig (2000), are listed in Tables 3.3 and 3.4. Note that for the $3\,M_\odot$ model the values of λ obtained are similar to the STARS calculations even though overshooting is not included in these models. However, the STARS models dredge-up efficiencies do not exceed unity. Dredge-up in Herwig's $4\,M_\odot$ model is significantly more efficient.

Both models naturally start off with higher core masses than the respective STARS models. This reflects the fact that evolution prior to the AGB with convective overshooting produces larger cores. According to Herwig the large dredge-up efficiency in his models is the result of overshooting below the pulse-driven intershell convection zone. This leads to a higher temperature at the bottom of this zone and a larger peak luminosity than without overshooting. Stronger shell flashes give rise to deeper dredge-up, as discussed above. For the $3\,M_\odot$ models, the STARS model produces similarly high peak helium luminosities and similarly deep dredge-up to Herwig's model even though overshooting is not included. For the $4\,M_\odot$ model, similar peak helium luminosities are reached in both models but Herwig's model produces significantly deeper dredge-up. Herwig's model also shows no sign of HBB occurring.

It should be noted that Herwig's models produce a ^{13}C pocket (albeit one

TP	$L_{He}/10^6\ L_\odot$	λ	$M_H/\ M_\odot$	C/O
1	0.46	-	0.63087	0.29
2	1.17	-	0.63288	0.29
3	2.13	-	0.63593	0.29
4	2.63	0.10	0.63962	0.30
5	3.18	0.23	0.64352	0.32
6	4.63	0.44	0.64726	0.38
7	6.71	0.53	0.65030	0.45
8	8.80	0.71	0.65289	0.54
9	13.9	0.82	0.65482	0.64
10	19.0	0.91	0.65616	0.74
11	29.4	0.98	0.65717	0.86
12	42.9	1.02	0.65773	0.97
13	59.9	1.04	0.65804	1.08

Table 3.3: Selected details of a $3\,M_\odot$ star evolved with convective overshooting and mass-loss taken from Table 1 of Herwig (2000). The data are TP – the thermal pulse number, L_{He} – the peak luminosity from helium burning, λ – the dredge-up efficiency parameter, M_H – the hydrogen free core mass and C/O – the surface carbon-to-oxygen ratio.

TP	$L_{He}/10^6\ L_\odot$	λ	$M_H/\ M_\odot$	C/O
1	2.26	-	0.78259	0.31
2	3.70	1.63	0.78211	0.34
3	6.21	1.51	0.78160	0.42
4	11.5	1.51	0.78083	0.51
5	21.0	1.51	0.77962	0.62
6	38.1	1.43	0.77814	0.72
7	59.8	1.42	0.77667	0.82
8	92.6	1.33	0.77522	0.91
9	123.3	1.33	0.77389	0.99
10	142.6	1.37	0.77253	1.06
11	195.5	1.32	0.77102	1.13

Table 3.4: Selected details of a $4\,M_\odot$ star evolved with convective overshooting and mass-loss taken from Table 2 of Herwig (2000). The data are TP – the thermal pulse number, L_{He} – the peak luminosity from helium burning, λ – the dredge-up efficiency parameter, M_H – the hydrogen free core mass and C/O – the surface carbon-to-oxygen ratio.

that is too narrow - see Denissenkov & Tout 2003) whereas the STARS ones require another mechanism.

3.5 Summary

In this chapter, the results of computations of TP-AGB stars in the mass range 1-7 $M_\odot$ have been presented. These are the first fully simultaneous calculations to be made of TP-AGB evolution. Whilst numerical instability remains a problem extended calculations are now possible without too much difficulty. Efficient third dredge-up is found in all the models barring the $1\,M_\odot$ and hot-bottom burning is found to occur in stars of $4\,M_\odot$ and above.

Comparison of the above results with calculations made with other evolution codes yields some interesting differences. While the STARS results produce similar trends across the mass range to those obtained by other codes, there is a general tendency for the STARS code to produce more efficient dredge-up at lower core masses. This efficient dredge-up is not related to the inclusion of convective overshooting. It is not clear why the STARS code should give more efficient dredge-up than other codes. It could be related to the simultaneous solution of the equations of stellar structure and evolution but this hypothesis has not been tested. The author has attempted to produce a decoupled version of the code that would have solved for the mixing after structural calculations had been made but severe numerical problems were encountered. Another possible explanation for the differences between the codes is their treatment of mixing. This also needs to be thoroughly investigated.

The fact that the STARS code produces efficient dredge-up at lower core masses than other codes could potentially be useful in attempting to solving the carbon star mystery (Iben, 1981). Current models of AGB stars are too luminous to reproduce the observed luminosity functions of carbon stars in the Large and Small Magellanic Clouds, i.e. dredge-up begins at too high a core mass and is not efficient enough. If the trends of the STARS models extend to lower metallicity then it may be possible to reproduce the LMC and SMC carbon star luminosity functions for the first time.

Chapter 4

TP-AGB Stars of Low Metallicity

In this chapter TP-AGB models of $Z = 0.008$ and $Z = 0.004$ (the metallicities of the Large and Small Magellanic Clouds) are presented. These models cover stars in the mass range 1 to 6 $M_\odot$[1] and, as with the solar metallicity models, they are computed without mass loss. In addition, the relevance of these models to the problem of the carbon star luminosity function (CSLF) is discussed. A detailed comparison of models computed with two different evolution codes is also performed.

4.1 The Z = 0.008 Models – TP-AGB Stars in the LMC

Table 4.1 presents the general properties of the models of metallicity $Z = 0.008$. Third dredge-up is found to occur in all the models. Numerical problems led to the early termination of the 1 $M_\odot$ model and it is unlikely that its maximum dredge-up efficiency represents the true value for this star. As with the solar metallicity models, hot-bottom burning is found to occur in stars of 4 $M_\odot$ and above. In comparison with the solar metallicity models, the $Z = 0.008$ models generally begin thermally pulsing with more massive cores reflecting the differences in their pre-AGB evolution. Lower-metallicity objects tend to have more massive cores for the same total mass. While the

[1] No 7 $M_\odot$ models are evolved for these metallicities because they would ignite carbon in their cores.

Mass ($M_\odot$)	No. TPs	M_{1TP}($M_\odot$)	TDUP?	M_{TDUP} ($M_\odot$)	λ_{max}	HBB?
1	8	0.54803	Yes	0.57981	0.278	No
1.5	40	0.56610	Yes	0.57735	0.752	No
2	15	0.56419	Yes	0.57866	0.880	No
3	7	0.63039	Yes	0.64135	0.992	No
4	9	0.81403	Yes	0.81676	1.100	Yes
5	17	0.87293	Yes	0.87602	1.085	Yes
6	11	0.95462	Yes	0.95696	1.098	Yes

Table 4.1: General properties of the $Z = 0.008$ models. The mass of the H-exhausted core at which a thermal pulse first occurs is M_{1TP}. The mass of the H-exhausted core at which TDUP first occurs is M_{TDUP}. The maximum efficiency of TDUP is λ_{max}. The final column lists whether the star experiences hot-bottom burning (HBB) or not.

difference is minimal for the low-mass objects (being as little as $0.007\,M_\odot$ for the $1\,M_\odot$ models), it becomes more pronounced for the intermediate mass models. The difference is greatest between the $3\,M_\odot$ models where the core mass at first thermal pulse is $0.08\,M_\odot$ greater for the $Z = 0.008$ model.

Unlike the solar metallicity models, the $Z = 0.008$ $1\,M_\odot$ model does experience third dredge-up. This is shown in Figure 4.1. Owing to the low envelope mass and also the low metallicity of this object the effect of a fairly modest amount of TDUP is quite dramatic. Figure 4.2 shows the evolution of CNO at the surface for this model. TDUP begins (barely!) at around 6×10^5 years and the third episode of TDUP is sufficient to make a carbon star. From the beginning of the TP-AGB to this point only 8 thermal pulses have happened. This model has significantly deeper dredge-up which begins at a much smaller core mass than the corresponding model of Karakas et al. (2002). This is seen to occur in models of 1 to $2\,M_\odot$. Its relevance to the problem of the carbon star luminosity function will be discussed in section 4.3.

Of all the $Z = 0.008$ models the $1.5\,M_\odot$ model was evolved for the longest before insurmountable numerical difficulties terminated the run. A total of 40 thermal pulses were evolved through. A plot of the evolution of the helium luminosity is shown in Figure 4.3. Note how the peak helium burning luminosity increases with each pulse, reaching a peak value of $\log L_{He}/L_\odot = 8.42$ by pulse 14, before declining again. The model starts off with an initial interpulse period of 1.3×10^5 yrs which steadily declines to around 2×10^4 yrs

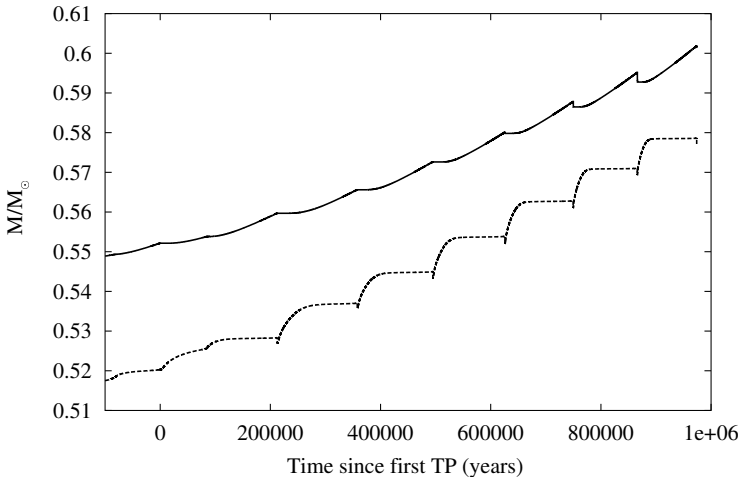

Figure 4.1: Evolution of the core masses for the $Z = 0.008$ 1 $M_\odot$ model. The H-exhausted core mass is the solid line; the dashed line represents the He-exhausted core mass. Note the occurrence of TDUP – the sudden reduction in the H-exhausted core mass – in the last 3 pulses.

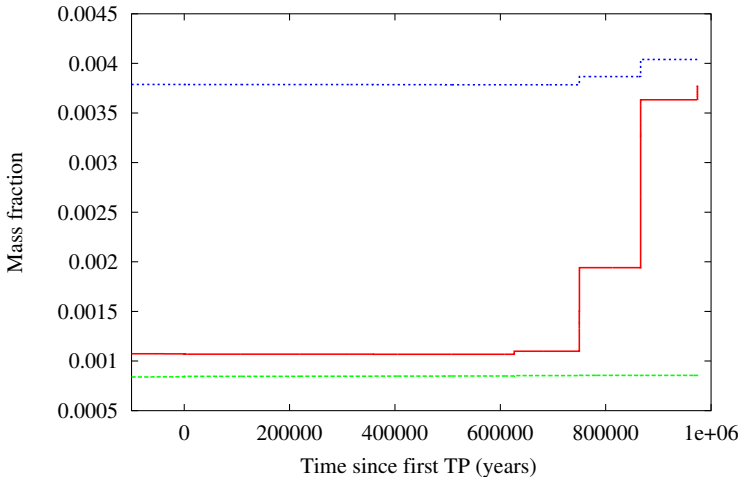

Figure 4.2: Evolution of the CNO abundances for the $Z = 0.008$ 1 $M_\odot$ model. Carbon is displayed in red, nitrogen in green and oxygen in blue.

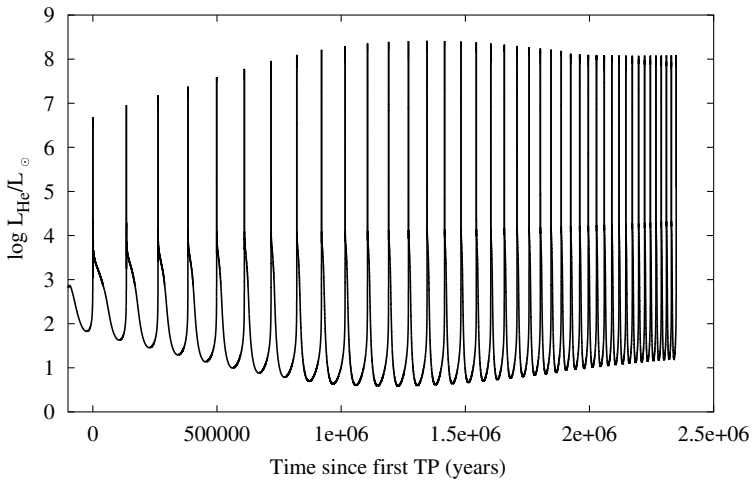

Figure 4.3: Evolution of the helium luminosity of the $1.5\,M_{\odot}$ model. The evolution covers a total of 40 thermal pulses.

by the end of the calculation. The behaviour of the efficiency of TDUP shows a steady increase over the first few pulses and reaches a maximum value of 0.752 by pulse 12. After this the dredge-up efficiency shows a steady but persistent decline.

Carbon stars are formed for all models of between 1 and $3\,M_{\odot}$. Above this mass, HBB sets in and the dredged-up carbon is rapidly converted into nitrogen. The $4\,M_{\odot}$ model is particularly interesting. Figure 4.4 displays the evolution of the surface CNO abundances. HBB starts to occur at around 7×10^4 yrs and it is possible to see its severity increase over the subsequent interpulse periods. Once it has begun, the nitrogen abundance rapidly increases and the rate of that increase steepens with each pulse while the carbon becomes more rapidly depleted. After just two pulses with HBB more carbon is depleted in the interpulse period than is brought to the surface by third dredge-up. Above this mass HBB sets in very quickly and the behaviour observed is similar to that seen in solar metallicity stars.

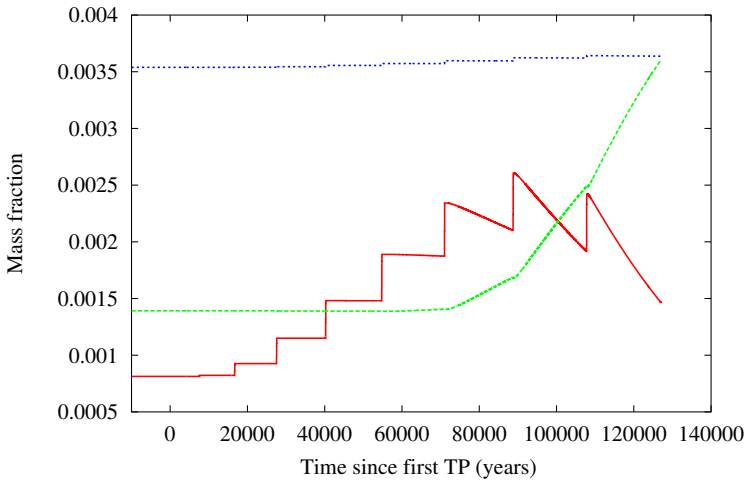

Figure 4.4: Evolution of the CNO abundances for the $Z = 0.008$ $4\,M_{\odot}$ model. Carbon is displayed in red, nitrogen in green and oxygen in blue. Note the onset of HBB at around 7×10^4 years and the increase in its severity over the subsequent interpulse periods.

4.2 The Z = 0.004 Models – TP-AGB Stars in the SMC

Table 4.2 presents the general properties of the models of metallicity $Z = 0.004$. As with the LMC metallicity models, TDUP is found to occur in all the models and hot-bottom burning occurs for stars of $4\,M_{\odot}$ and above. Once again, insurmountable numerical difficulties prevented further evolution of these models. In the case of the $1\,M_{\odot}$ object, this occurred during the second episode of TDUP just after, but probably not related to, the formation of a carbon star. Hence the value of $\lambda_{\rm max}$ obtained for this model is probably not a good indication of the maximum value that this object would actually reach. Comparison of the core mass at first thermal pulse for a given initial mass shows that lower metallicity objects tend to have more massive cores, reflecting the differences in their evolution prior to the TP-AGB (see Figure 4.5).

The trends observed at higher metallicity are again displayed in these models. The models of between 1 and $3\,M_{\odot}$ all form carbon stars. In the case of the $1\,M_{\odot}$ model it takes just two episodes of third dredge-up to do

Mass ($M_\odot$)	No. TPs	M_{1TP}($M_\odot$)	TDUP?	M_{TDUP} ($M_\odot$)	λ_{max}	HBB?
1	4	0.56326	Yes	0.58048	0.127	No
1.5	12	0.57680	Yes	0.58849	0.774	No
2	11	0.60032	Yes	0.60275	0.916	No
3	9	0.71385	Yes	0.71421	1.048	No
4	8	0.83004	Yes	0.83166	1.097	Yes
5	14	0.90159	Yes	0.90292	1.068	Yes
6	7	0.97297	Yes	0.97383	0.954	Yes

Table 4.2: General properties of the $Z = 0.004$ models. The mass of the H-exhausted core at which a thermal pulse first occurs is M_{1TP}. The mass of the H-exhausted core at which TDUP first occurs is M_{TDUP}. The maximum efficiency of TDUP is λ_{max}. The final column lists whether the star experiences hot-bottom burning (HBB) or not.

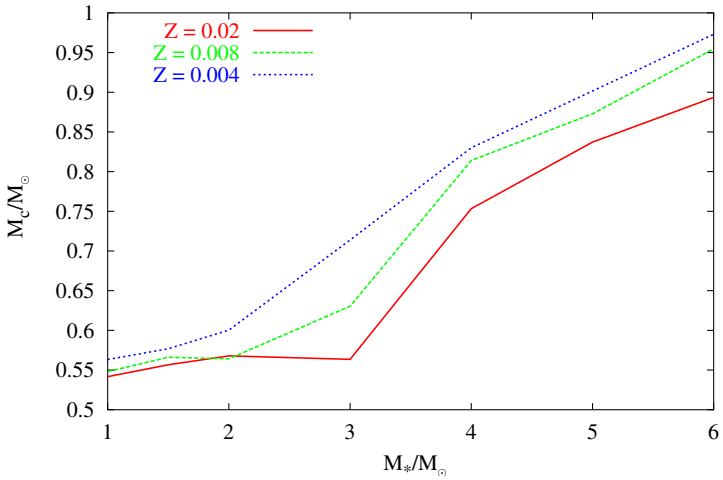

Figure 4.5: Comparison of the hydrogen-exhausted core mass (M_c) at first thermal pulse across the range of initial masses (M_*) for all three metallicities present so far. Note that in nearly all cases, the lower metallicity objects have larger core masses than the higher metallicity ones.

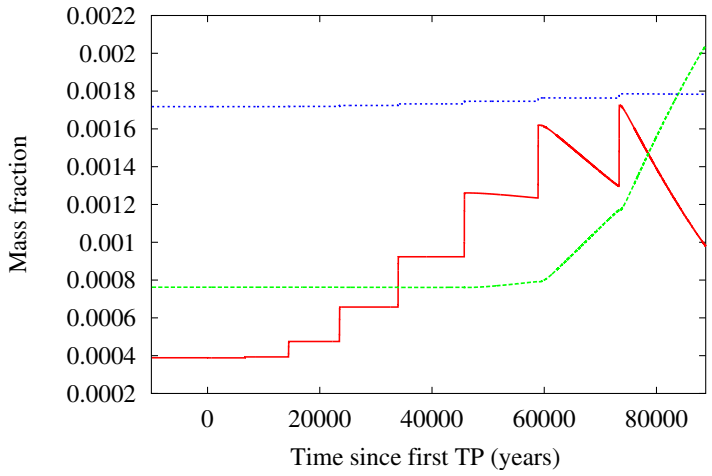

Figure 4.6: Evolution of the surface CNO abundances for the $Z = 0.004$ $4\,M_\odot$ model. Carbon is in red, nitrogen in green and oxygen in blue.

this. Models more massive than around $4\,M_\odot$ are seen to display hot-bottom burning. The $4\,M_\odot$ model spends a short amount of time as a carbon star before HBB becomes sufficiently strong to cause depletion of carbon. As with the $Z = 0.008$ $4\,M_\odot$ model, the severity of HBB can be seen to increase with each subsequent pulse.

Problems with HBB led to the early termination of the 5 and $6\,M_\odot$ models. It was found that, during TDUP as the H-rich envelope penetrates into the hot H-exhausted core regions, numerical instabilities set in. These are linked to the movement of the mesh. If a mesh point that is rich in hydrogen moves inward during TDUP (which it is likely to do given the form of the mesh spacing function) it carries some of the hydrogen down with it. This is numerical diffusion, an undesirable and (to a large degree) unavoidable consequence of the adaptive mesh used by the STARS code. In the present case it also has an undesirable effect. The hydrogen finds itself suddenly at a higher temperature which increases the energy generation and feeds back to the structure with unfortunate consequences for the stability. This problem must be solved if the higher mass objects are to be investigated further. The viscous mesh could be employed here and used to prevent movement of the mesh. This may alleviate the problem.

4.3 The Carbon Star Luminosity Function

As a set of models of TP-AGB stars at the metallicities of the Large Magellanic Cloud (LMC) and Small Magellanic Cloud (SMC) have been produced, the luminosity function of carbon stars in these populations can be investigated. Carbon stars are stars which show the features of carbon rich molecules such as C_2 and CN in their spectra, rather than oxides such as TiO, indicating they have a surface carbon-to-oxygen ratio (by number) greater than unity. They are typically identified in photometric surveys using the colours from narrow band filters centred near 7800Å and 8100Å (Cook & Aaronson, 1989). The first filter focuses on a TiO absorption feature whilst the latter centres on a CN absorption feature. A census of carbon stars has been performed in the LMC and SMC. In the LMC a total of 7750 carbon stars have been found; in the SMC 1707 are known (Groenewegen, 2004). The distances to the LMC and SMC are well determined and so we are able to construct luminosity functions for the carbon stars in both these locations. It is therefore possible to test models of stellar evolution.

It is believed that two populations of carbon stars exist. These reflect two different formation routes. They are referred to as *intrinsic* and *extrinsic*. The intrinsic carbon stars are believed to be thermally pulsing asymptotic giant branch stars. As seen above, in low-mass stars repeated occurrence of TDUP gives rise to carbon stars because the products of helium burning are carbon plus a little oxygen. The extrinsic carbon stars are believed to be formed by the accretion of carbon-rich material from a more evolved donor (Van Eck et al., 1998).

There is a long-standing problem with forming intrinsic carbon stars. Detailed stellar evolution models have so far proved unable to produce dredge-up at low enough core masses and hence at low enough luminosities. When Iben formulated the carbon star mystery (Iben, 1981) calculations showed that dredge-up did not occur for core masses below about $0.6\,M_\odot$ (e.g. Sackmann, 1980; Wood & Zarro, 1981). This is also borne out by more recent calculations and leads to problems in reproducing the observed luminosity functions of the LMC and the SMC as described below.

The STARS code has been able to produce more efficient TDUP and in some cases at lower core masses than other codes, so it is important to investigate the impact that the LMC and SMC metallicity models have on

the problem of the carbon star luminosity function (CSLF).

4.3.1 LMC Models

For the LMC models carbon stars are formed in all models of $3\,M_\odot$ and below. The formation of carbon stars in these models is extremely rapid. It requires only two or three thermal pulses with TDUP. This is because of the low abundance of oxygen: only a small amount of carbon needs to be dredged up for it to become more abundant than oxygen. The maximum λ value of the $1\,M_\odot$ model quoted in Table 4.1 is unlikely to be a true representation of the maximum efficiency reached because numerical instabilities prevent the model from being evolved to a steady state.

For models of $2\,M_\odot$ or below the core masses at which the first episode of dredge-up occurs are lower than those in other models. For example, Karakas et al. (2002) find their $1\,M_\odot$ model without mass loss does not begin dredge-up until its core mass is $0.657\,M_\odot$. This is $0.084\,M_\odot$ more massive than the model presented here. This is important because it is expected that the lower mass stars become the lower luminosity carbon stars. More efficient third dredge-up is also found in these stars.

With the results of Karakas et al. (2002), Izzard & Tout (2004) used a synthetic evolution code to fit the observed CSLF. They found that the minimum core mass for third dredge-up to occur would have to be lower by $0.07\,M_\odot$ and the minimum dredge-up efficiency would have to be 0.5 to get a good fit. The results of this chapter are in very good agreement with these predictions. They show deeper and earlier dredge-up. These models are also consistent with the requirement of a minimum temperature at the base of the convective envelope of $2.5 \times 10^6\,K$ for third dredge-up to occur as used by Marigo, Girardi & Bressan (1999) in their synthetic code.

Figure 4.7 shows the evolution of the surface C/O abundance by number with absolute bolometric magnitude. The data points are taken at the minimum luminosity occurring during the interpulse as this is what determines the lowest luminosity carbon star that forms. The results are encouraging. It is found that the two lowest-mass models are able to form carbon stars at an absolute bolometric magnitude of about -4.2 well below the LMC CSLF peak at $M_{bol} = -4.9$.

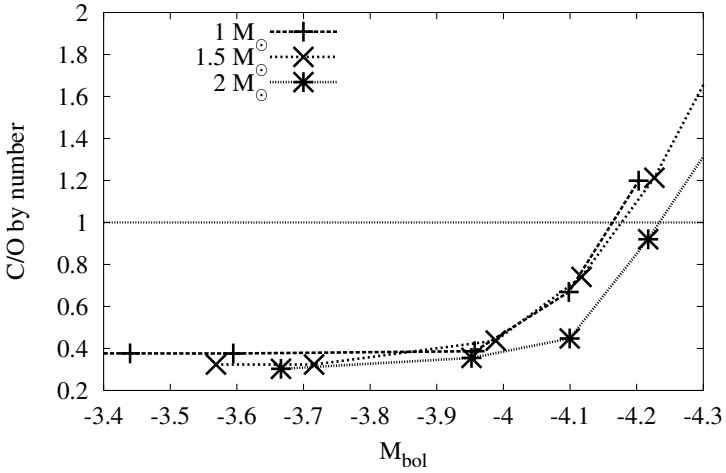

Figure 4.7: The evolution of surface C/O with absolute bolometric magnitude, measured at the time of minimum luminosity in the interpulse, for models of 1, 1.5 and 2 $M_\odot$. The LMC carbon star luminosity function peaks at $M_{bol} = -4.9$.

4.3.2 SMC models

As with the LMC models, carbon stars are formed in all models below $3\,M_\odot$. Again, carbon star formation follows rapidly once TDUP is established and occurs even more readily due to the lower oxygen abundance. For the same reasons as with the LMC model, λ_{max} is unlikely to be truly representative of the maximum efficiency reached.

The results of the SMC model runs are less encouraging from the point of view of reproducing the SMC carbon star luminosity function. The low-mass models give minimum core masses for third dredge-up similar to those of Karakas et al. (2002). The only advantage is the occurrence of TDUP in the $1\,M_\odot$ model. Figure 4.8 shows the evolution of the C/O abundance with absolute bolometric magnitude. The lowest mass models become carbon stars with $M_{bol} = -4.2$. This is only just below the peak of the SMC CSLF.

4.3.3 Population Synthesis

In order to see if these new models can reproduce the LMC and SMC CSLF a population of stars based on these detailed models needs to be created. The synthetic TP-AGB evolution code of Izzard et al. (2004) is utilized. The

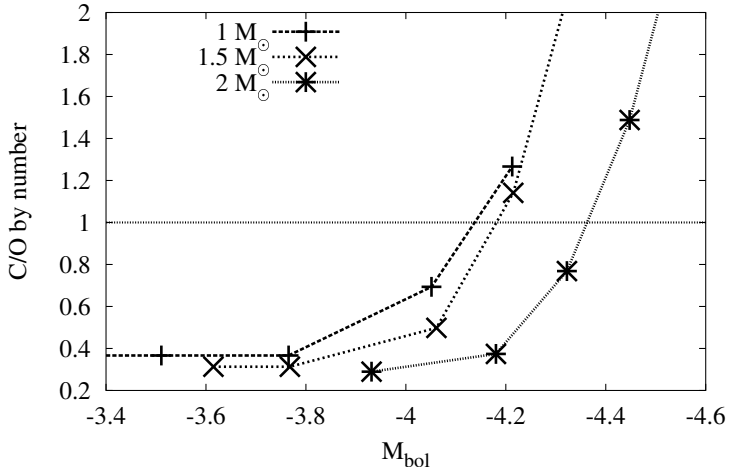

Figure 4.8: The evolution of surface C/O with absolute bolometric magnitude, measured at the time of minimum luminosity in the interpulse, for models of 1, 1.5 and 2 $M_\odot$. The SMC carbon star luminosity function peaks at $M_{bol} = -4.5$.

luminosity core-mass relation therein, is found to fit the new data well and so does not need to be refitted. If the core mass, M_c, is greater than $0.58\,M_\odot$ at the first thermal pulse then the luminosity is given by

$$L = 3.7311 \times 10^4 \times \max[(\frac{M_c}{M_\odot} - 0.52629)(2.7812 - \frac{M_c}{M_\odot}), 1.2(\frac{M_c}{M_\odot} - 0.48)] \tag{4.1}$$

otherwise it is given by

$$L = \max[4(18160 + 3980Z)(M_c - 0.4468) - 4000, 10]. \tag{4.2}$$

As in Izzard & Tout (2004), the luminosity dip after each thermal pulse (see Iben & Renzini 1983) is modelled by a factor of the form

$$f_L = 1 - 0.5 \times \min\left[1, \exp(-3\frac{\tau}{\tau_{ip}})\right], \tag{4.3}$$

where τ is the time from the beginning of the current pulse and τ_{ip} is the interpulse period. In this form the luminosity dip found in the detailed models can be reproduced (see Figure 4.9). It is necessary to include this dip in order to reproduce the low-luminosity side of the CSLFs. The core masses

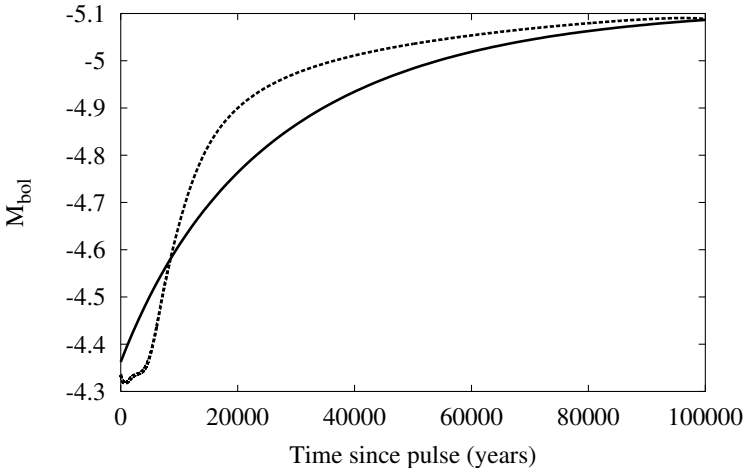

Figure 4.9: Plot of the exponential fit (solid line) to the post-flash luminosity dip of the 4th pulse of the $2\,M_\odot$ Z= 0.008 model (dashed line). The fit leads to an underestimate of the bolometric magnitude of about 0.1 mag.

at the first thermal pulse, $M_{1\mathrm{TP}}$, minimum core mass for third dredge-up to occur, $M_{\mathrm{c,min}}$, and λ values used by the synthetic code are fitted to the above detailed models[2]. Additional models of 1.25, 1.75 and $2.25\,M_\odot$ were made for the LMC in order to better model the behaviour of the core mass. The fits are

$$M_{1\mathrm{TP}} = 0.9557 + 0.31741 \exp\left[-\frac{(M_* - 1.164)^2}{1.1192}\right] - \frac{0.82352}{1 + 0.31831^{2.7546 - M_*}} \tag{4.4}$$

for the LMC and

$$M_{1\mathrm{TP}} = 0.56633 + \frac{0.067603 M_*}{1 + 0.096788^{M_* - 2.6354}} \tag{4.5}$$

for the SMC, where M_* is the mass of the star at the beginning of the TP-AGB. Third dredge-up begins in the models when the core mass reaches a minimum value, $M_{\mathrm{c,min}}$ defined by

$$M_{\mathrm{c,min}} = 0.9659 + 0.26309 \exp\left[-\frac{(M_* - 1.0724)^2}{1.2629}\right]$$

[2]The fits were calculated by Dr. R. G. Izzard.

$$-\frac{0.73763}{1+0.3344^{2.86280-M_*}} \tag{4.6}$$

for the LMC and

$$M_{\rm c,min} = 0.58042 + \frac{0.065376 M_*}{1+0.098049^{M_*-2.6691}} \tag{4.7}$$

for the SMC.

The behaviour of λ once TDUP has commenced is modelled by

$$\lambda = a[1-(1-0.42n)\mathrm{e}^{-\frac{n}{b}}], \tag{4.8}$$

$$\begin{aligned} a = \max(0, 2.0369 + 15Z - 2.8775M_* + 1.6206M_*^2 \\ -0.335270M_*^3 + 0.023211M_*^4), \end{aligned} \tag{4.9}$$

$$b = 6.835 - \frac{4.44870}{1+0.002^{M_*-2.5}}, \tag{4.10}$$

where Z is the metallicity and n is the pulse number counting the first pulse where dredge-up occurred as 1. The last factor in Equation 4.8 allows λ to rise to a maximum over several pulses and then begin to fall off as is seen in the detailed models. The low number of thermal pulses calculated in the $1\,\mathrm{M}_\odot$ models makes a reliable estimate for λ difficult and so for stars of between 1 and $1.5\,\mathrm{M}_\odot$ the values as computed for the $1.5\,\mathrm{M}_\odot$ case are used. This makes dredge-up slightly more efficient but as carbon stars form rapidly at such low masses this will not significantly affect the results.

A population of 10,000 stars was evolved for 16 Gyr. A Kroupa, Tout & Gilmore (1993) initial mass function and a constant star formation rate were assumed. Mass loss was included by the Vassiliadis & Wood (1993) type prescription used by Karakas et al. (2002). The superwind phase is turned on when the Mira pulsation period of the star reaches 500 d. The synthetic code has been fitted to results from detailed models without mass loss. Because the Vassiliadis & Wood formalism causes significant mass loss only in the later pulses and the models form carbon stars rapidly, the impact of this approximation on the results should be limited.

The results of the population synthesis runs are shown in Figures 4.10 and 4.11. The models are normalized such that the peak of a model matches the peak of the corresponding observations. The model fits the observations

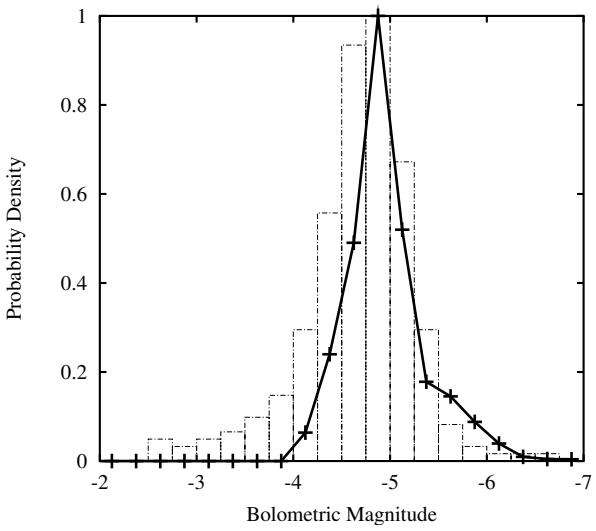

Figure 4.10: The theoretical fit (solid line) to the LMC CSLF. The histogram is observational data taken from Groenewegen (2004). The CSLF is reasonably well reproduced by the theoretical models.

of the LMC CSLF very well except for a slight underabundance of carbon stars between $M_{bol} = -4$ and $M_{bol} = -4.75$. Note that the model does not fit the very low-luminosity carbon stars. These are likely to be extrinsic, rather than intrinsic, carbon stars (see Izzard & Tout, 2004).

The fit to the SMC CSLF is somewhat disappointing. The peak in the model luminosity function is almost 1 magnitude too bright. If the minimum core mass for dredge-up is reduced by 0.06 $M_{\odot}$ as in Izzard & Tout (2004) then the SMC CSLF can be reproduced (see Figure 4.11). Again, the very low luminosity tail is expected to be due to extrinsic carbon stars.

It should be noted that these models of the LMC and SMC CSLFs consist only of a single metallicity and do not account for the finite size of the clouds. Both these effects would broaden the luminosity function slightly. The work of Harries, Hilditch & Howarth (2003) gives examples of systems with distance moduli that can be as much as 0.2 magnitudes from the quoted distance to the SMC. This is unlikely to have a great effect on the luminosity function, given the binning is of this order but it may improve the LMC model. The effect of metallicity variations is much more difficult to quantify, though it should be noted that varying the metallicity by a factor of 2 (i.e. going from Z= 0.008 for the LMC to Z= 0.004 for the SMC) does produce

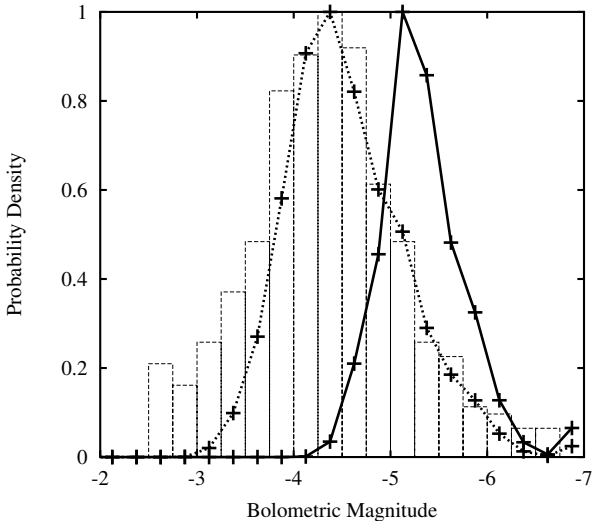

Figure 4.11: Theoretical fits to the SMC CSLF. The histogram is observational data taken from Groenewegen (2004). The unadjusted theoretical model (solid line) reproduces the shape of the luminosity function well, but it is too bright by almost 1 magnitude. If the minimum core mass required for TDUP is reduced by $0.06\,M_{\odot}$ (dashed line) then the CSLF is well reproduced.

noticeably different results.

4.4 Detailed Model Comparison

It is not obvious why the models generated by the STARS code should give lower core masses than those produced by the Monash version of the Mount Stromlo Stellar Structure Program (MSSSP) as used by Karakas et al. (2002). In order to better understand these differences a set of detailed comparisons were carried out. Models calculated with the MSSSP were provided by Dr. Amanda Karakas and are used here with her kind permission. Models of 1, 3 and $5\,M_{\odot}$ at a metallicity of $Z = 0.008$ were evolved without the use of mass loss or convective overshooting. Each code used a value for the mixing length parameter, α, appropriate for that code based on calibration to a solar model. Initial abundances were solar-scaled based on the values in Anders & Grevesse (1989).

Before commencing a comparison of the models it is important to point out some inherent problems. To make the discussion as meaningful as possible it would be desirable to have two codes that only differed in, for example,

their treatment of mixing. In reality, a great many differences exist between two separate codes. Everyone employs slightly different reaction rates, has their own equation of state, treats semiconvection differently, couples their equations differently and so on. Unfortunately, this makes it exceptionally difficult to determine why code A's models are different from code B's and tends to leave one describing *how* the models differ rather than *why*.

4.4.1 Evolutionary Properties

Figure 4.12 shows the evolution of the helium luminosity for the first few pulses of a $1\,M_\odot$ model computed with both codes. At the beginning of the TP-AGB the STARS model has a H-exhausted core mass that is about $0.01\,M_\odot$ larger than the MSSSP model. It suffers more violent TPs than the MSSSP model and the helium luminosity during the interpulse is much lower. This is reflected in the temperature of the helium burning shell. The STARS code produces higher temperatures during thermal pulses (for example the first pulse has a He-shell temperature about 14% higher than the first pulse in the MSSSP model), while during the interpulse period these temperatures are somewhat lower (see Figure 4.13). This behaviour is to be expected. A more massive core binds the He-shell to itself more tightly. It therefore takes a stronger pulse (i.e. a higher helium shell temperature during the pulse) to overcome this effect.

Rather than looking at the evolution from the first thermal pulse, it is perhaps more desirable to compare two pulses which take place at approximately equal core mass. If it is assumed that the core mass controls the characteristics of the pulse then any differences visible should be down to differences in the codes as opposed to comparing physical situations that are not alike. The 5^{th} pulse of the STARS sequence and the 9^{th} pulse of the MSSSP sequence have core masses within $0.001\,M_\odot$ of one another. Despite the similarity of the core masses and the almost identical temperatures in the preceding interpulse phase, the STARS code gives a more violent pulse (by a factor of about 3 in terms of the peak helium luminosity reached).

The situation is similar in the $3\,M_\odot$ models. While the two models enter the TP-AGB with very similar helium luminosities (see Figure 4.14), the STARS model generates a slightly more violent first pulse and its pulses grow in strength at a faster rate than the MSSSP one. As with the $1\,M_\odot$ model

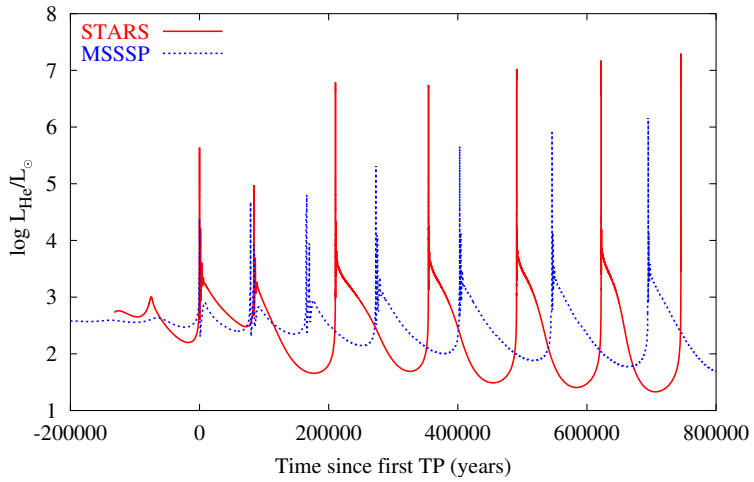

Figure 4.12: Comparison of the evolution of the helium luminosity for a $1\,M_{\odot}$ model computed using the STARS and MSSSP codes.

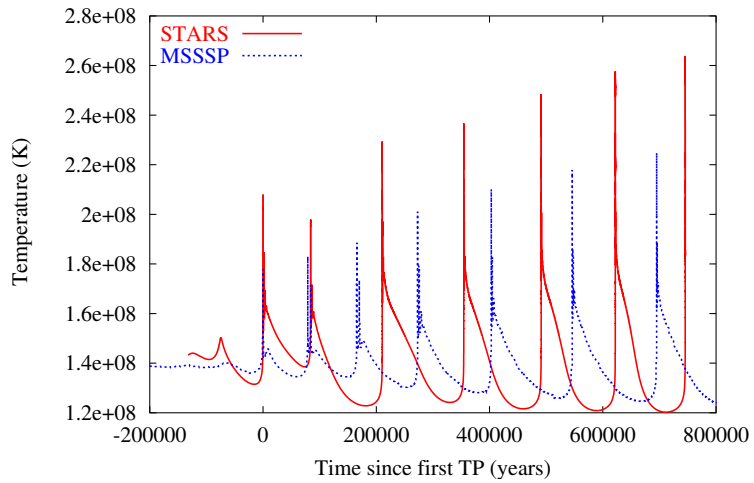

Figure 4.13: Comparison of the evolution of the helium shell temperature for a $1\,M_{\odot}$ model computed using the STARS and MSSSP codes.

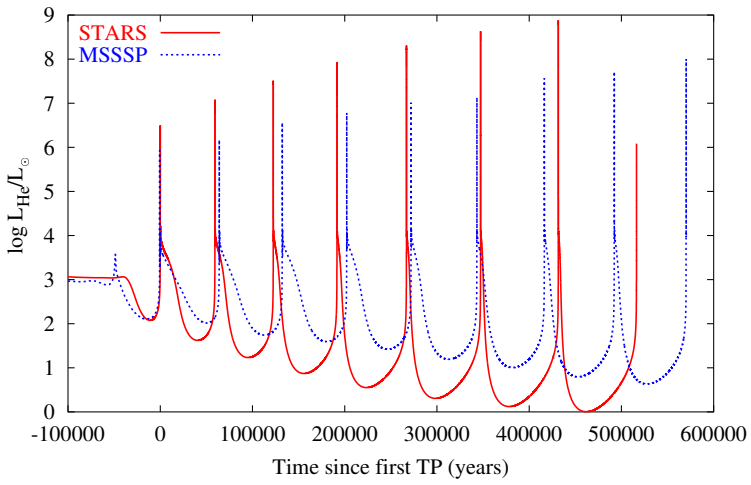

Figure 4.14: Comparison of the evolution of the helium luminosities for $3\,M_\odot$ models computed using the STARS and MSSSP codes.

the STARS model gives lower helium luminosities during the interpulse. At the first thermal pulse the MSSSP model has a core mass which is lower than the STARS model's by $0.01\,M_\odot$. The evolution of the core masses is shown in Figure 4.15. It should be noted that dredge-up begins in both models when the core mass grows above around $0.644\,M_\odot$. This happens on the second pulse in the STARS model and on the fourth pulse in the MSSSP model. In both models, the peak helium luminosity of the pulse preceding the first episode of dredge-up is approximately the same.

The $5\,M_\odot$ models start off with very similar helium luminosities. In fact, the peak helium luminosity reached in the first thermal pulse is identical in the two models (see Figure 4.16) despite the MSSSP model having a core mass that is lighter than the STARS model by about $0.008\,M_\odot$. This suggests that the pulse strength does not just depend on the core mass. The subsequent evolution is the same as in the lower mass cases. The strength of the pulses grows more rapidly in the STARS model than it does in the MSSSP model. The STARS model may give deeper dredge-up because its pulses are stronger than the MSSSP model's. Note that the interpulse period of the STARS model is shorter. This is due to the model having a higher H-burning shell temperature which enables H to be processed to He via the CNO cycle more rapidly. A higher H-shell temperature is to be expected from a star

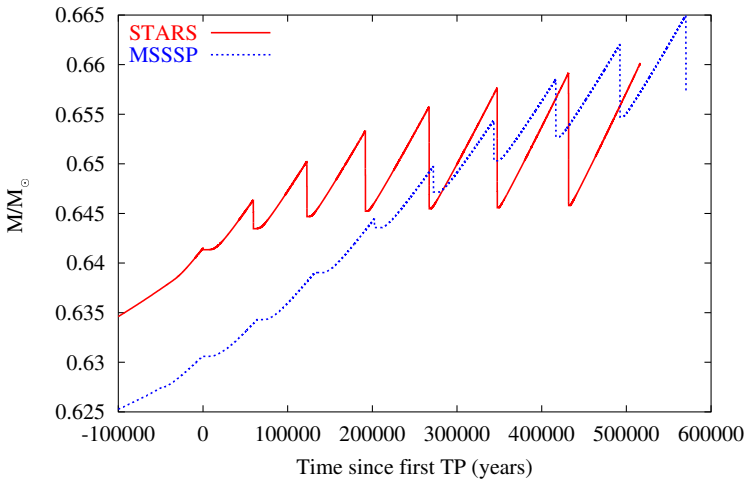

Figure 4.15: Comparison of the evolution of the H-exhausted core masses of $3\,M_{\odot}$ models computed using the STARS and MSSSP codes.

with a more massive core.

In all the comparisons it is noted that the models start off with different core masses at the first thermal pulse. This difference is related to the evolution prior to the AGB, specifically the evolution during core helium burning which is sensitive to the treatment of semiconvection (see the discussion in Straniero et al., 2003, for example). Apart from the differences in the core masses, there is no obvious indication as to why the models evolve differently. To search for possible sources of this divergence it is useful to focus on a particular pulse and examine the changes that occur in the interior as the pulse progresses.

4.4.2 Focusing on a Pulse

Considering the similarity in strength of the first thermal pulse of the $5\,M_{\odot}$ models and their subsequent divergence, examining in detail what happens during the pulse is a useful exercise. To this end detailed interior models were produced at three points during this pulse. By examining details such as the thermodynamic variables as a function of mass it may be possible to detect why the models begin to diverge. The points chosen were at the peak of the pulse and also at 500 and 1000 years after the peak of the pulse. It should be noted that the points used in this comparison are not exactly

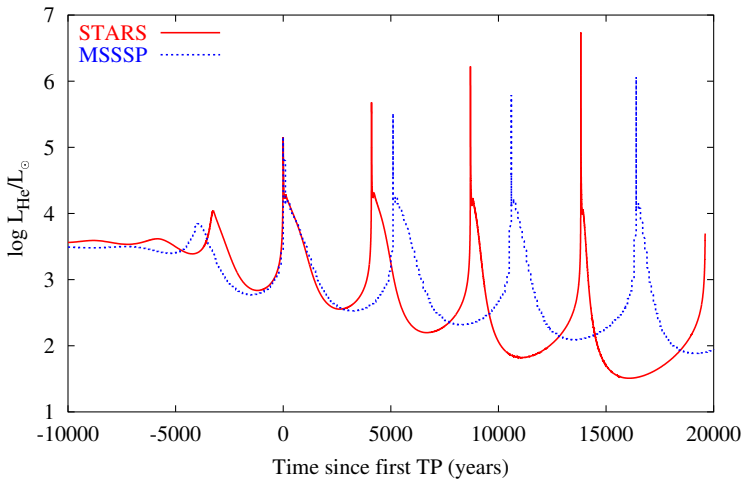

Figure 4.16: Comparison of the evolution of the helium luminosity for $5\,M_{\odot}$ models computed with the STARS and MSSSP codes.

coincident in time but as close as the output of the codes allows.

Profiles of the pressure, density, temperature, degeneracy parameter (ψ), opacity and thermal energy as functions of mass across the intershell region are shown in Figures 4.17, 4.18 and 4.19. These are taken from the peak of the pulse, 500 and 1000 years after the peak of the pulse, respectively. At first glance, it looks like there may be some significant differences between the two models. However this proves to be an artifact of the plots, owing to the fact that the two models have different core masses. If one model is shifted by about $0.008\,M_{\odot}$ the pressure, density and ψ plots are virtually identical at each of the three times considered.

Looking at the profiles at the peak of the thermal pulse (Figure 4.17) there are some minor differences in the plots of the temperature and thermal energy profiles. The spike in the temperature profile is slightly higher in the STARS model and the thermal energy reaches more negative values (i.e. more energy is being used up in expanding regions of the star). These differences are likely to be due to their being a slight difference in the times at which the two models were taken. Evolution around the peak of the pulse is extremely rapid so a slight difference in time between the two models can lead to a large difference in their internal structures. The core of the STARS model also appears to be slightly hotter than that of the MSSSP model. However

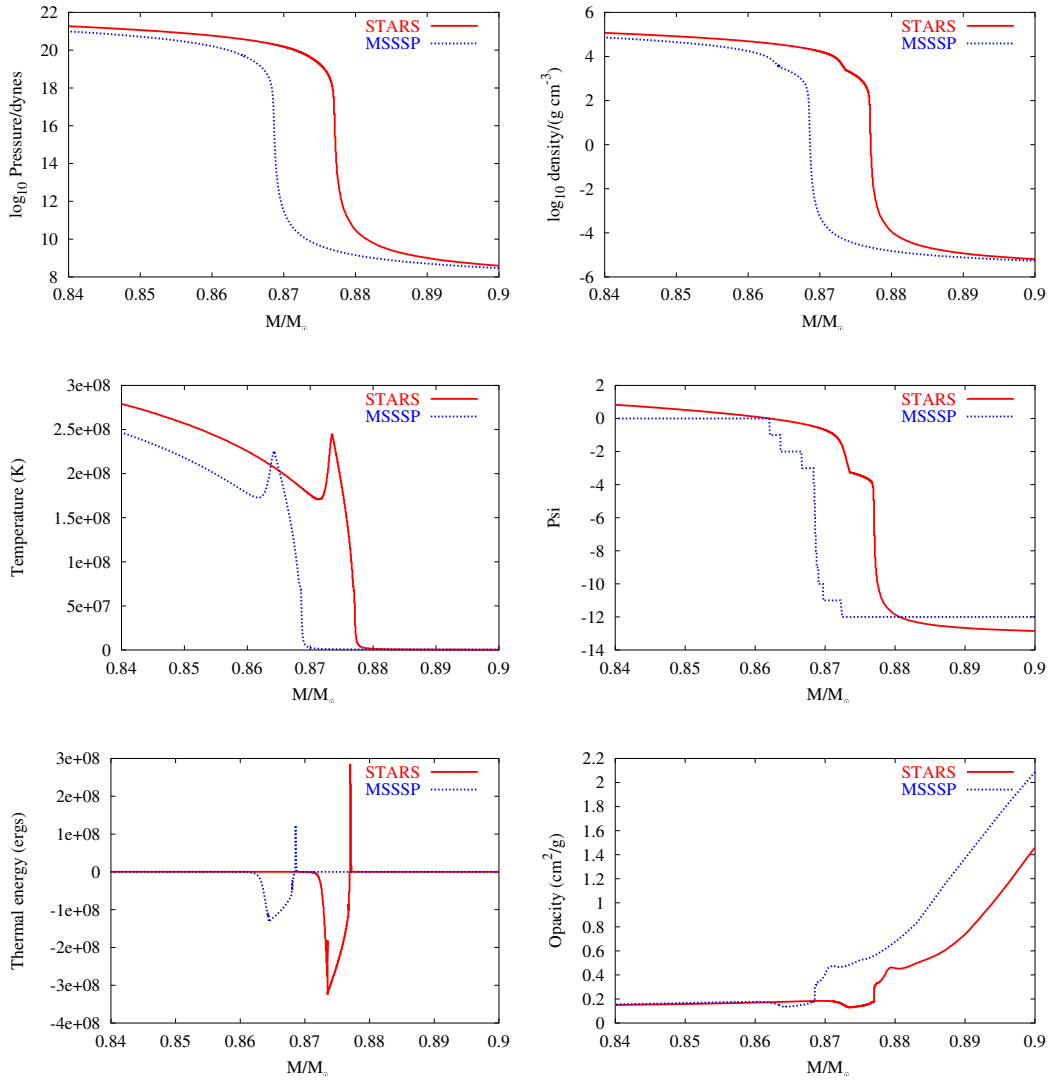

Figure 4.17: Thermodynamically important variables as a function of mass across the intershell at the peak of the first thermal pulse of the $5\,M_{\odot}$ model. Note that the blocky profile for the degeneracy parameter ψ in the MSSSP model is due to the low accuracy that this variable is stored to in the output files.

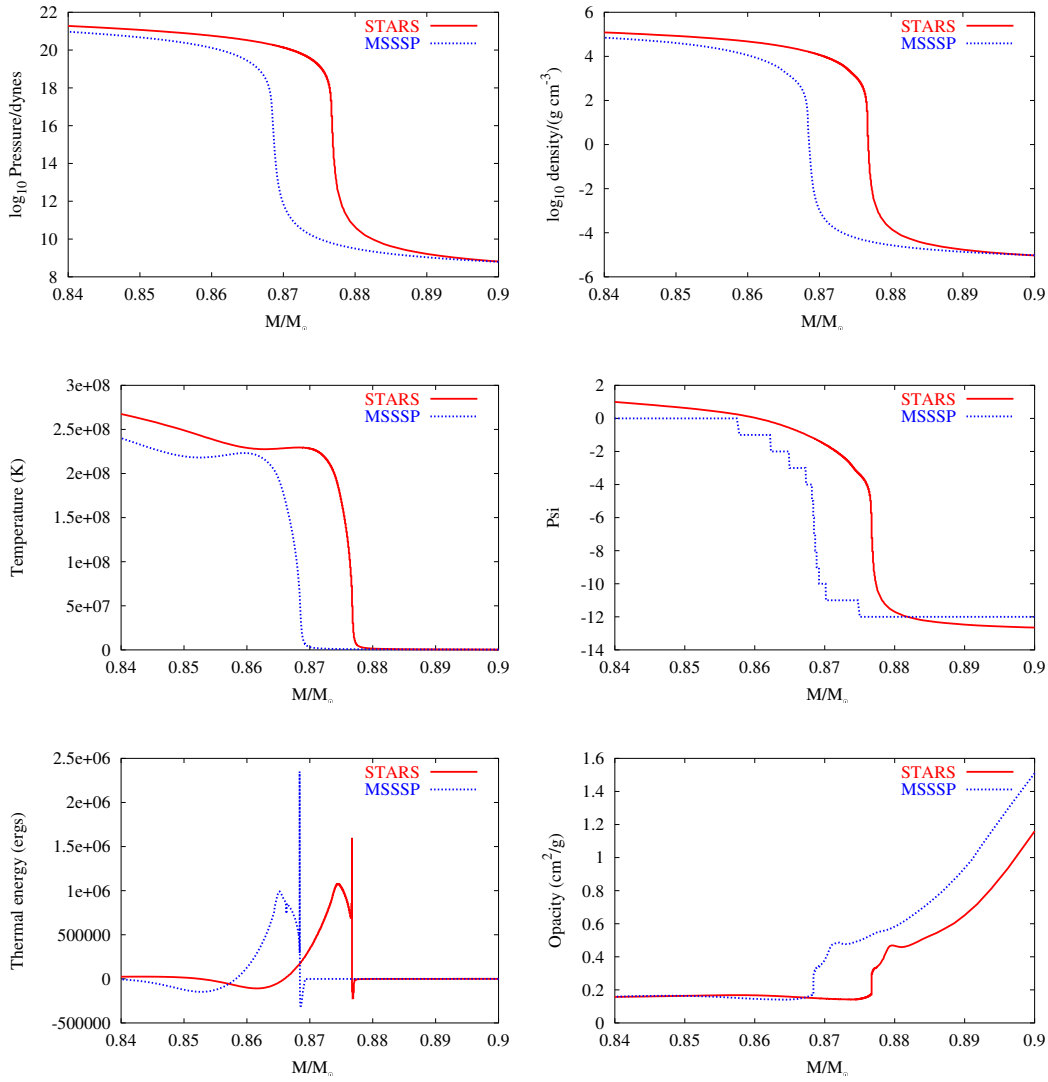

Figure 4.18: Thermodynamically important variables as a function of mass across the intershell 500 years after the peak of the first thermal pulse of the $5\,M_{\odot}$ model. Note that the blocky profile for the degeneracy parameter ψ in the MSSSP model is due to the low accuracy that this variable is stored to in the output files.

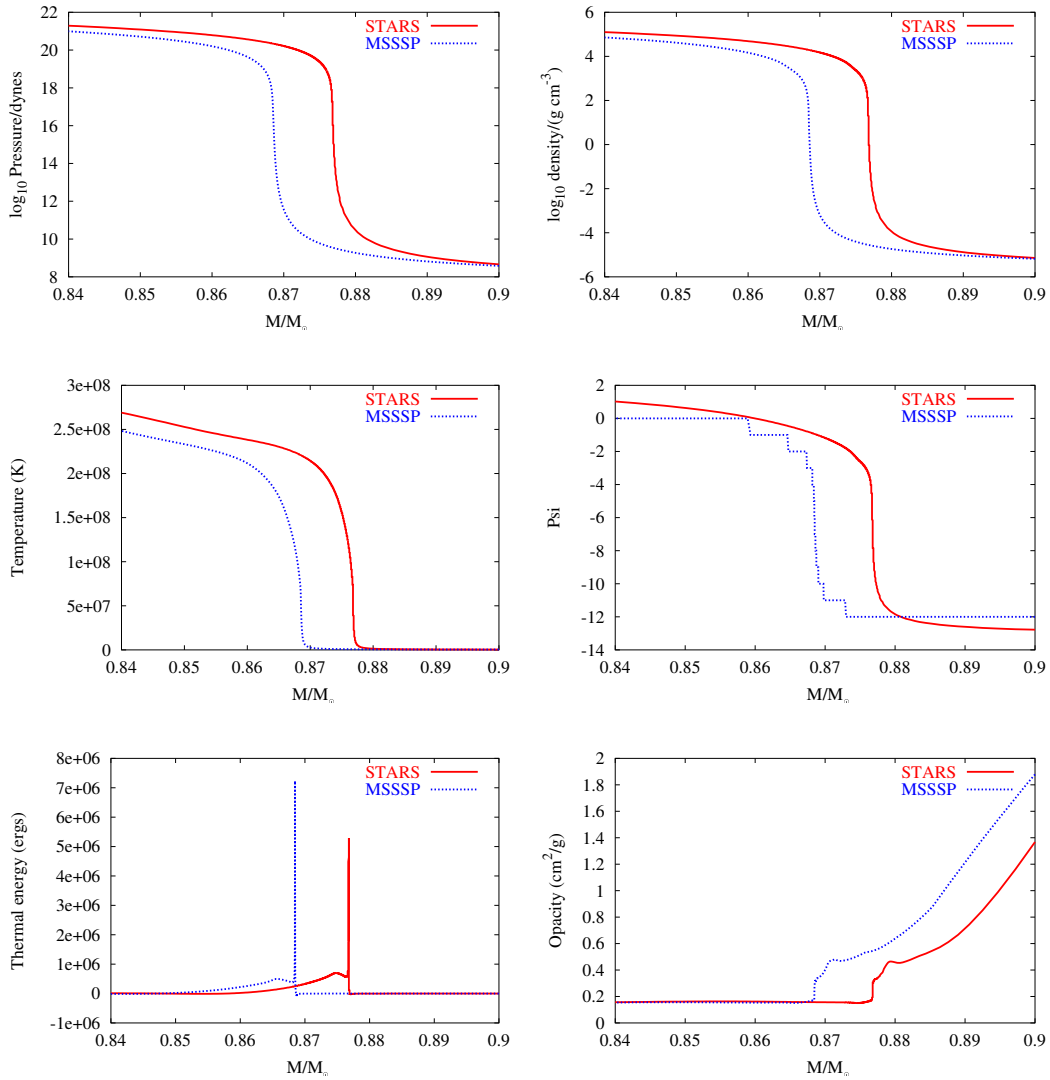

Figure 4.19: Thermodynamically important variables as a function of mass across the intershell 1000 years after the peak of the first thermal pulse of the $5\,M_{\odot}$ model. Note that the blocky profile for the degeneracy parameter ψ in the MSSSP model is due to the low accuracy that this variable is stored to in the output files.

the difference is minimal and may just reflect that the STARS model has a more massive core.

The profiles of the two models at the other two times show the same trends. In both cases, the pressure, density, ψ and thermal energy profiles are virtually identical. As with the profiles at the peak of the thermal pulse, the STARS model shows temperatures that are slightly higher than in the MSSSP model. However, there is one difference that does stand out. The opacity profile in the STARS model is noticeably higher above $0.89\,M_{\odot}$ at 500 years after the thermal pulse. By 1000 years after the pulse, the two opacity profiles are back to being virtually identical in the region being plotted. Looking at the opacity profile at greater masses (i.e. up into the envelope of the star) shows that by about $1\,M_{\odot}$ the MSSSP model has a greater opacity and that it becomes significantly greater in the outer regions of the star. While this affects the luminosity and surface temperature of the star, it is difficult to see how it would affect the intershell region and hence it cannot be used to explain the divergence of the two models.

There is no obvious explanation as to why the two models should diverge in their behaviour. This is perhaps not too surprising as the divergence is only slight and so the cause must be a subtle one. The real cause is probably hidden behind the myriad differences between the STARS and MSSSP codes. In an ideal world, the comparison would be done between two codes that were identical in all but one respect but this would require a major effort on the part of the users of one or both of the codes. Also the two codes should probably be given the same starting model as well so that any differences in behaviour can be solely attributed to something that happens on the TP-AGB. However, there are occasions in which the author has found that getting one of his own models to converge with his own code is impossible and hence the prospect of converging a model from one code with another code is somewhat daunting. More work needs to be done in this area if the differences between models produced with different codes are to be truly understood.

4.5 Summary

In this chapter, the results of calculations of TP-AGB stars of between 1 and $6\,M_\odot$ calculated at metallicities appropriate to the LMC and SMC, have been presented. These models give deeper dredge-up than has been found in previous calculations. For stars of 1 to $2\,M_\odot$ at LMC metallicity, the models show dredge up to begin at a smaller H-exhausted core mass than has been found in previous calculations.

The models presented in this chapter have been applied to the problem of the carbon star luminosity function. Details from the STARS models have been used as input parameters for a population synthesis program. In this way it is possible to produce a theoretical CSLF for stars in the LMC and SMC. It is found that the CSLF of the LMC can be reproduced using the STARS models but the SMC CSLF cannot be. It is unclear why this is.

In order to address why the STARS models give notably different results from other calculations a detailed comparison of models of metallicity $Z = 0.008$ computed using the STARS and MSSSP codes has been made. Three separate masses were examined and in each case the STARS code had a more massive core at the first thermal pulse and the thermal pulses were seen to grow in strength at a faster rate. The difference in core mass is due to evolution prior to the AGB. In the case of the $5\,M_\odot$ model, both models produced an equally intense first thermal pulse but the subsequent evolution diverged. A detailed examination of the profiles of the models at the peak of the first pulse and at 500 and 1000 years afterwards failed to show any reason for the divergence, although the core of the STARS model was seen to be slightly hotter.

Chapter 5

Nucleosynthesis on the TP-AGB

In nova fert animus mutatas dicere formas corpora.
My mind is bent to talk of substances changed into new forms.

Publius Ovidius Naso, *Metamorphoseon, Liber I*

In this chapter updates to the portion of the STARS code that deals with the evolution of minor isotopes are described. The nucleosynthesis of light isotopes in TP-AGB stars of 1.5, 3 and 5 $M_\odot$ at $Z = 0.02, 0.008$ and 0.004 is discussed.

5.1 Updating the Algorithms

Chapter 2 briefly touched upon the existence of a couple of subroutines in the STARS code that were designed to be used to study the evolution of minor isotopes. Minor isotopes are defined to be those whose abundances are too low or whose reactions liberate insufficient energy to affect the structure of the star. The main evolution code assumes that only ^{1}H, ^{4}He, ^{12}C, ^{14}N, ^{16}O and ^{20}Ne have reactions whose energy generation significantly affects the structure of the star. The minor isotopes subroutines were put into the code by Dr. Peter Eggleton in the code's early days but it would appear that they have not been touched since (other than to adjust the common blocks to make sure the code will still compile and run).

These subroutines, which hereinafter are referred to as the nucleosynthesis subroutines, comprise the two files `funcs2` and `equns2`. They are used by the code as follows. First a model is converged with the main evolution code. This gives the structure of the model at the new timestep. The details of this model are then passed into the nucleosynthesis subroutines in order to calculate what the minor isotope compositions should be at the new timestep. The subroutine `funcs2` contains the physics required to compute the changes in the compositions of the minor isotopes while `equns2` sets up the necessary difference equations. These can then be passed to `solver` and its attendant matrix-solving subroutines in order to work out the changes to the abundances of the minor isotopes.

The main evolution routines deal with equations that are complicated functions of the variables that the code computes changes to. It therefore makes sense to calculate the derivatives required by the code numerically, rather than analytically. Analytic derivatives would be better but would make it harder to implement changes in the code. The numerical derivatives are calculated by making several passes through the physics package `funcs1`, slightly changing each variable in turn and calculating the differences between each pass and an unchanged run. However as structural parameters have already been determined by the main evolution routine, the derivatives required by the nucleosynthesis subroutines only depend on the minor isotope abundances. This means that the derivatives are simple functions of the composition and can be computed analytically (and easily changed if necessary) which gives a considerable saving of computing time if many isotopes are being dealt with. The difference equation for the evolution of the composition of the element X_i is

$$\left(\frac{\sigma_{k+\frac{1}{2}}}{\delta m_{k+\frac{1}{2}}} + [-\dot{m}_{k+1}]\right)(X_{i,k+1} - X_{i,k}) - \left(\frac{\sigma_{k-\frac{1}{2}}}{\delta m_{k-\frac{1}{2}}} + [\dot{m}_k]\right)(X_{i,k} - X_{i,k-1}) - \left(\frac{X_{i,k} - X^0_{i,k}}{\Delta \mathrm{t}} + R_{X_i,k}\right)\delta m_k = 0 \tag{5.1}$$

where $X_{i,k}$ and $X^0_{i,k}$ are the abundances of element X_i at mesh point k at the present and previous timestep, Δt is the timestep, $\delta m_{k\pm\frac{1}{2}}$ are the masses contained in the zones above and below mesh point k, $R_{X_i,k}$ is the net consumption rate of X_i by nuclear reactions, and $\sigma_{k\pm\frac{1}{2}}$ are the diffusion coefficients corresponding to these zones. Square brackets indicate that the quantity

within is only to be considered if it is positive – these terms deal with the fact that the mesh may move from one timestep to the next. The derivatives of Equation 5.1 with respect to element X_j are

$$\delta_{ij}\left\{\frac{\sigma_{k+\frac{1}{2}}}{\delta m_{k+\frac{1}{2}}}+[-\dot{m}_{k+1}]\right\}=0 \tag{5.2}$$

at mesh point $k+1$,

$$\delta_{ij}\left\{-\left(\frac{\sigma_{k+\frac{1}{2}}}{\delta m_{k+\frac{1}{2}}}+[-\dot{m}_{k+1}]\right)-\left(\frac{\sigma_{k-\frac{1}{2}}}{\delta m_{k-\frac{1}{2}}}+[\dot{m}_{k}]\right)\right\} -\delta_{ij}\frac{1}{\Delta \mathrm{t}}\delta m_k+\frac{\mathrm{d}R_{X_i,k}}{\mathrm{d}X_j}\delta m_k=0 \tag{5.3}$$

at mesh point k and

$$\delta_{ij}\left\{\frac{\sigma_{k-\frac{1}{2}}}{\delta m_{k-\frac{1}{2}}}+[\dot{m}_{k}]\right\}=0 \tag{5.4}$$

at mesh point $k-1$. These quantities are all calculated within the subroutine `funcs2` and the difference equations and their derivatives are set up by `equns2`.

The original nucleosynthesis subroutines were designed to deal with the same isotopes as the main evolution code plus ^{3}He. The routines have now been expanded to include a total of 40 minor isotopes plus the six major elements used in the main evolution code. It is necessary to include these six because under some circumstances (e.g. during the formation of a ^{13}C pocket) the compositions are expected to deviate slightly from those used in the main code. These deviations are unimportant from the point of view of the structure of the star but can affect the nucleosynthesis. The new nucleosynthesis subroutines cover all the stable isotopes (plus a few important unstable ones) from deuterium up to ^{34}S plus ten elements around the iron group. These isotopes are listed in Table 5.1.

Unstable nuclei that are not included in the network are treated as if their decay were instantaneous. This approximation is fair for all light isotopes with half-lives from seconds to hours during most phases of stellar evolution. For the unstable isotopes considered in the network, the decay lifetimes are the terrestrial values given by Krane (1988).

Light isotopes
$\mathbf{^{1}H}$,*n*,^{2}H,^{3}He,$\mathbf{^{4}He}$,^{7}Li,^{7}Be,^{11}B,$\mathbf{^{12}C}$,^{13}C,
^{14}C,$\mathbf{^{14}N}$,^{15}N,$\mathbf{^{16}O}$,^{17}O,^{18}O,^{19}F,$\mathbf{^{20}Ne}$,^{21}Ne,^{22}Ne,
^{22}Na,^{23}Na,^{24}Mg,^{25}Mg,^{26}Mg,$^{26}Al^{m}$,$^{26}Al^{g}$,^{27}Al,^{28}Si,^{29}Si,
^{30}Si,^{31}P,^{32}S,^{33}S,^{34}S
Iron group isotopes
^{56}Fe,^{57}Fe,^{58}Fe,^{59}Fe,^{60}Fe
^{59}Co,^{58}Ni,^{59}Ni,^{60}Ni,^{61}Ni

Table 5.1: Isotopes included in the nucleosynthesis code. Isotopes also included in the structural part of the code are highlighted in bold. Unstable isotopes are in italics.

5.1.1 Charged Particle Reaction Rates

In order to couple the nucleosynthesis network 63 charged particle reactions are required. The rates are taken from a variety of sources and are listed in Table 5.2 (proton captures) and Table 5.3 (α captures). The rate of the reaction ^{3}He(^{3}He,2p)^{4}He is that given by Caughlan & Fowler (1988), as are the rates for carbon and oxygen burning reactions.

The nucleosynthesis routines were designed to employ the ready-to-use fits to the reaction rates from the REACLIB library (1991 updated version of Thielemann et al., 1986), updated where possible to include the latest experimental results (see Lugaro et al., 2004, for full details). For some of the rates involved in the production of ^{19}F, such as $^{15}\mathrm{N}(\alpha,\gamma)^{19}\mathrm{F}$, the rates are virtually the same as those presented in the NACRE compilation (Angulo & et al., 1999). In other cases, such as the rates $^{14}\mathrm{N}(\alpha,\gamma)^{18}\mathrm{F}$ and $^{18}\mathrm{O}(\alpha,\gamma)^{22}\mathrm{Ne}$, the rates used are updates with respect to the NACRE rates.

5.1.2 Neutron Capture Rates

A total of 45 neutron capture reactions are required for the network. The work of Bao et al. (2000) was used as the main source. Supplementary (n,γ) data are taken from Rauscher & Thielemann (2000) for captures by ^{59,60}Fe. Rates for the reaction $^{33}\mathrm{S}(\mathrm{n},\alpha)^{30}\mathrm{Si}$ were taken from Schatz et al. (1995). For the reactions $^{26}\mathrm{Al}^{g}(\mathrm{n},\mathrm{p})^{26}\mathrm{Mg}$ and $^{26}\mathrm{Al}^{g}(\mathrm{n},\alpha)^{23}\mathrm{Na}$ rates are from Koehler et al. (1997). The important reaction rate for $^{14}\mathrm{N}(\mathrm{n},\mathrm{p})^{14}\mathrm{C}$ is from Gledenov et al. (1995), which is in agreement with previous experimental (Koehler &

Reaction	Source
^{1}H(p,$\beta^{+}\nu$)^{2}H	REACLIB
^{2}H(p, γ)^{3}He	CF88
^{7}Li(p, α)^{4}He	CF88
^{7}Be(p, γ)2^{4}He	CF88
^{12}C(p, γ)^{13}N	CF88
^{13}C(p, γ)^{14}N	NACRE
^{14}C(p, γ)^{15}N	W90
^{14}N(p, γ)^{15}O	CF88
^{15}N(p, γ)^{16}O	CF88
^{15}N(p, α)^{12}C	CF88
^{16}O(p, γ)^{17}F	CF88
^{17}O(p, γ)^{18}F	L90,B95
^{18}O(p, γ)^{19}F	CF88
^{18}O(p, α)^{15}N	CF88
^{19}F(p, γ)^{20}Ne	CF88
^{19}F(p, α)^{16}O	CF88
^{21}Ne(p, γ)^{22}Na	EL95
^{22}Ne(p, γ)^{23}Na	EL95
^{22}Na(p, γ)^{23}Mg	SC95,ST96
^{23}Na(p, γ)^{24}Mg	EL95
^{23}Na(p, α)^{20}Ne	EL95
^{24}Mg(p, γ)^{25}Al	99tDC
^{25}Mg(p, γ)^{26}Al^{g}	I96
^{25}Mg(p, γ)^{26}Al^{m}	I96
^{26}Mg(p, γ)^{27}Al	I90
^{27}Al(p, γ)^{28}Si	CF88
^{27}Al(p, α)^{24}Mg	T88,C88
^{28}Si(p, γ)^{29}P	G90
^{29}Si(p, γ)^{30}P	CF88
^{30}Si(p, γ)^{31}P	CF88

Table 5.2: Proton capture reactions and the sources from which their rates were taken. Key: C88 (Champagne et al., 1988), CF88 (Caughlan & Fowler, 1988), B95 (Blackmon et al., 1995), EL95 (El Eid & Champagne, 1995), G90 (Görres et al., 1990), I90 (Iliadis et al., 1990), I96 (Iliadis et al., 1996), L90 (Landre et al., 1990), NACRE (Angulo & et al., 1999), SC95 (Schmidt et al., 1995), ST96 (Stegmüller et al., 1996), REACLIB (1991 updated version of Thielemann et al. 1986), T88 (Timmermann et al., 1988), W90 (Wiescher et al., 1990).

Reaction	Source
$^{4}\mathrm{He}(\alpha\alpha,\gamma)^{12}\mathrm{C}$	CF88
$^{7}\mathrm{Li}(\alpha,\gamma)^{11}\mathrm{B}$	CF88
$^{12}\mathrm{C}(\alpha,\gamma)^{16}\mathrm{O}$	CF88
$^{13}\mathrm{C}(\alpha,\mathrm{n})^{16}\mathrm{O}$	D95
$^{14}\mathrm{C}(\alpha,\gamma)^{18}\mathrm{O}$	JG01
$^{14}\mathrm{N}(\alpha,\gamma)^{18}\mathrm{F}$	G00
$^{15}\mathrm{N}(\alpha,\gamma)^{19}\mathrm{F}$	deO96
$^{16}\mathrm{O}(\alpha,\gamma)^{20}\mathrm{Ne}$	CF88
$^{17}\mathrm{O}(\alpha,\mathrm{n})^{20}\mathrm{Ne}$	D95
$^{18}\mathrm{O}(\alpha,\gamma)^{22}\mathrm{Ne}$	D03
$^{18}\mathrm{O}(\alpha,\mathrm{n})^{21}\mathrm{Ne}$	D95
$^{19}\mathrm{F}(\alpha,\mathrm{p})^{22}\mathrm{Ne}$	U04
$^{20}\mathrm{Ne}(\alpha,\gamma)^{24}\mathrm{Mg}$	CF88
$^{21}\mathrm{Ne}(\alpha,\gamma)^{25}\mathrm{Mg}$	CF88
$^{21}\mathrm{Ne}(\alpha,\mathrm{n})^{24}\mathrm{Mg}$	D95
$^{22}\mathrm{Ne}(\alpha,\gamma)^{26}\mathrm{Mg}$	K94
$^{22}\mathrm{Ne}(\alpha,\mathrm{n})^{25}\mathrm{Mg}$	K94
$^{23}\mathrm{Na}(\alpha,\mathrm{n})^{26}\mathrm{Al}^{g}$	CF88
$^{23}\mathrm{Na}(\alpha,\mathrm{n})^{26}\mathrm{Al}^{m}$	CF88
$^{24}\mathrm{Mg}(\alpha,\gamma)^{28}\mathrm{Si}$	CF88
$^{25}\mathrm{Mg}(\alpha,\gamma)^{29}\mathrm{Si}$	CF88
$^{25}\mathrm{Mg}(\alpha,\mathrm{n})^{28}\mathrm{Si}$	CF88
$^{25}\mathrm{Mg}(\alpha,\mathrm{p})^{28}\mathrm{Al}$	CF88
$^{26}\mathrm{Mg}(\alpha,\gamma)^{30}\mathrm{Si}$	CF88
$^{26}\mathrm{Mg}(\alpha,\mathrm{n})^{29}\mathrm{Si}$	CF88
$^{26}\mathrm{Mg}(\alpha,\mathrm{p})^{29}\mathrm{Al}$	CF88
$^{27}\mathrm{Al}(\alpha,\gamma)^{31}\mathrm{Si}$	REACLIB

Table 5.3: Reactions involving α capture and the sources from which their rates were taken. Key: CF88 (Caughlan & Fowler, 1988), D95 (Denker et al., 1995), deO96 (de Oliveira et al., 1996), G00 (Görres et al., 2000), JG01 (Jorissen & Goriely, 2001), D03 (Dababneh et al., 2003), K94 (Kaeppeler et al., 1994), REACLIB, 1991 updated version of Thielemann et al. (1986), U04 (Ugalde, 2004).

O'Brien, 1989) and theoretical (Bahcall & Fowler, 1969) estimates. This rate is approximately a factor of two higher than the rate proposed by Brehm et al. (1988) and used by Meynet & Arnould (1993, 2000). For neutron captures by ^{59}Ni reaction rates are taken from Holmes et al. (1976) and this is also the source of the rate of the reaction $^{17}\mathrm{O}(\mathrm{n},\alpha)^{14}\mathrm{N}$.

In addition to this, two neutron sinks are included to account for neutron captures by those elements not included in the network, following the method of Jorissen & Arnould (1989). The first sink is emulated by the reaction $^{34}\mathrm{S}(\mathrm{n},\gamma)^{35}\mathrm{S}$ and represents nuclei between ^{34}S and the iron group. The value of the cross-section for this sink is calculated by averaging over the contribution from all the missing elements, i.e.

$$\sigma^{\mathrm{light}} = \frac{\Sigma_{i=34}^{55} X_i \sigma_i}{\Sigma_{i=34}^{55} X_i} \tag{5.5}$$

where X_i is the abundance of isotope i and σ_i is the cross-section for neutron capture by that isotope. The second sink is emulated by the reaction $^{61}\mathrm{Ni}(\mathrm{n},\gamma)^{62}\mathrm{Ni}$ and represents captures by all the heavy elements above ^{61}Ni. The cross-section of this heavy sink is computed in a similar way to the light sink. The value used for the cross-sections of the sinks are dependent on the mass and metallicity of the star being calculated. Appropriate rates for the models computed in this section were provided by M.A. Lugaro (private communication).

The heavy sink reaction also has another important function. It can be used to give an approximate indication of how much *s*-process nucleosynthesis takes place. This is done by assuming that neutron capture by ^{61}Ni generates ^{62}Ni which then decays with an ad hoc decay rate of 1 per second. The decay of ^{62}Ni is assumed to produce ^{61}Ni and an additional particle, g. This g particle is affectionately, if unofficially, referred to as a gallino. By counting the number of gallinos produced it is possible to estimate the *s*-process nucleosynthesis that is occurring.

The introduction of neutrons into the network was found to produce numerical instability. The capture cross-sections for the neutron reactions give much faster reaction rates than the reactions involving charged particles and the code is unable to simultaneously solve for changes associated with both neutron and charged particle reactions. In order to circumvent this

problem the following strategy was adopted. The changes due to charged particle reactions are solved for first and any neutrons produced by these reactions are noted. The rates of the neutron capture reactions are calculated, but the neutrons are not yet allowed to react. Once the nucleosynthesis model has been converged and the abundances at the next timestep have been determined, the neutrons that have been produced during that timestep are then captured by the appropriate isotopes based on the relative reaction rates. In this way all the neutrons produced in one timestep are assumed to used be up. Given the strength of the neutron reactions, this is a reasonable assumption.

5.2 Light Isotope Nucleosynthesis

To investigate the nucleosynthesis of light elements in TP-AGB stars models of 1.5, 3 and 5 $M_\odot$ were calculated at three different metallicities, $Z = 0.02$, 0.008 and 0.004. In order to make the models slightly more realistic than in the previous two chapters mass loss was included in these simulations. On the RGB and E-AGB, a Reimers' type mass loss was applied with $\eta = 0.4$. At the beginning of the TP-AGB, the value of η was increased to 1. While the Reimers' mass-loss law is almost certainly not the perfect mass-loss law to apply to the TP-AGB (it does not produce a model with a superwind phase), it does provide reasonable mass loss during the early pulses and enables some comment to be made on the yields from these stars.

5.2.1 Nucleosynthesis During a Thermal Pulse

As an example of the capabilities of the nucleosynthesis subroutines and to elucidate some of the nucleosynthesis that can occur in an AGB star, the case of the Ne-Na cycle is considered. The Ne-Na cycle involves the isotopes ^{20}Ne, ^{21}Na, ^{21}Ne, ^{22}Na, ^{22}Ne and ^{23}Na (Arnould et al., 1999). The sequence of reactions is

$$^{20}\mathrm{Ne}(\mathrm{p},\gamma)^{21}\mathrm{Na}(\beta^+)^{21}\mathrm{Ne}(\mathrm{p},\gamma)^{22}\mathrm{Na}(\beta^+)^{22}\mathrm{Ne}(\mathrm{p},\gamma)^{23}\mathrm{Na}(\mathrm{p},\alpha)^{20}\mathrm{Ne} \qquad (5.6)$$

and there is some leakage into the cycle from $^{19}\mathrm{F}(\mathrm{p},\gamma)^{20}\mathrm{Ne}$ and out of the cycle via $^{23}\mathrm{Na}(\mathrm{p},\gamma)^{24}\mathrm{Mg}$.

Figure 5.1 shows profiles of the abundances of the main evolution isotopes (to aid identification of the phase of the TP cycle) and the stable isotopes involved in the Ne-Na cycle at four points of a thermal pulse cycle. These are just after TDUP, during the interpulse phase when the H-shell is moving outwards in mass, when the intershell convection zone is active and finally during TDUP after the TP. The top two panels of Figure 5.1 show the discontinuity in composition that has been left behind by TDUP – this is located at just over $0.6\,M_{\odot}$. The next pair of panels down show the point where the H-shell has moved outward in mass. As the H-burning shell moves outward it causes strong depletions in ^{19}F, ^{21}Ne, ^{22}Ne as the Ne-Na cycle favours creation of ^{23}Na at the temperatures found in the H-burning shell of such a model (Karakas & Lattanzio, 2003).

By the time the helium burning shell and the intershell convection zone become active, the H-burning shell has moved outward in mass substantially (third pair of panels in Figure 5.1). Note that small amounts of ^{21}Ne and ^{22}Ne have been produced at the mass co-ordinate of the point of re-ignition of the H-burning shell after TDUP. This is to be expected. Limited proton captures by ^{20}Ne lead to the creation of ^{21}Ne, some of which is converted to ^{22}Ne (Karakas & Lattanzio, 2003). The effect on the ^{20}Ne is unnoticeable owing to its high abundance. The effect of the intershell convection zone on the Ne-Na cycle isotopes is mostly to mixing material into the ^{21,22}Ne depleted region left by H-burning. Some α-capture may occur but it does not substantially change the intershell abundances. As TDUP occurs (bottom pair of panels, Figure 5.1) the envelope pushes into the intershell region where the material is enhanced in ^{19}F, ^{22}Ne and ^{23}Na. The envelope abundances of these elements would be expected to show enhancements as a consequence of TDUP.

5.2.2 Surface Composition Evolution

The evolution of the surface compositions of the models will now be described in relation to the various constraints from observations and measurements of isotopes in pre-solar grains.

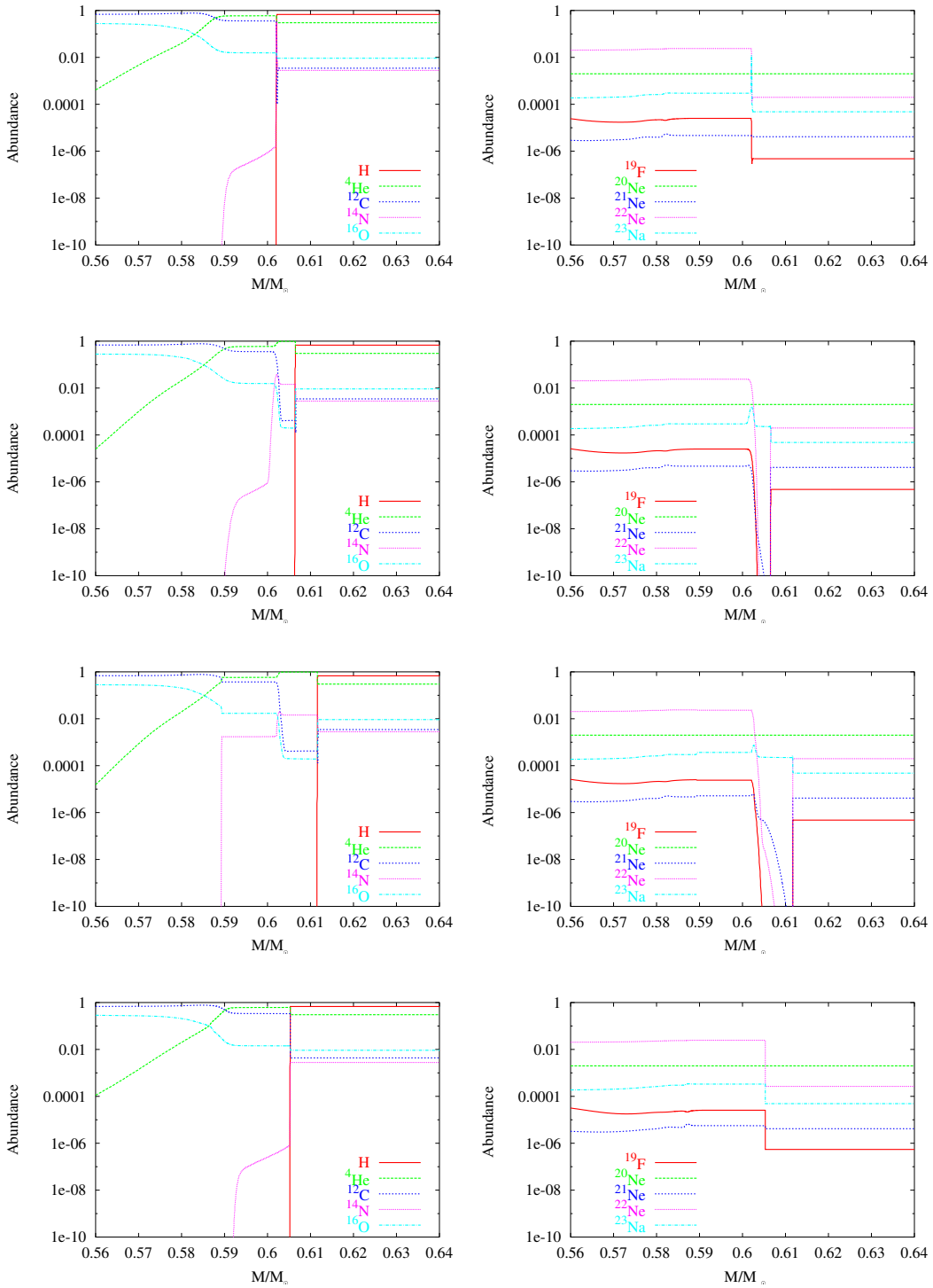

Figure 5.1: The effects of the Ne-Na cycle in the H-shell. The left hand panels show the main isotopes and help to identify the phase of the TP. The right hand panels show the corresponding abundances of the elements involved in the Ne-Na cycle. From top to bottom the phases are: post-TDUP of the previous pulse, growth of the H-exhausted core during the interpulse, part way through a TP and TDUP after the TP.

Constraints From Pre-solar Grains

The study of pre-solar grains has become a very important test of stellar models. Laboratory techniques can give measurements of isotopic ratios that are far more precise than is possible with spectroscopic measurements of stars. While there are some caveats on which type of grains are formed in which sources, they nonetheless provide a valuable tool for stellar modellers.

For the purposes of AGB stars the most important grains are silicon carbide (SiC). It is currently believed that these grains can only form in conditions where the C/O ratio exceeds unity, i.e. in carbon stars. Thus isotopic measurements from these grains offer the chance to examine in detail the surface composition of low-mass AGB stars (and also possibly that of intermediate mass AGB stars in their last few thermal pulses when HBB has shut down).

In addition to SiC grains, measurements of various kinds of oxide grains have also been made. These grains include corundum (Al_2O_3), spinel ($MgAl_2O_4$) and various types of silicate (SiO_4). These grains are believed to form in conditions where C/O is less than 1 and so offer a window on the intermediate mass AGB stars as well as the early phases of the low-mass AGB stars.

Plots of the evolution of the isotope ratios $^{12}C/^{13}C$, $^{14}N/^{15}N$, $^{16}O/^{17}O$, $^{16}O/^{18}O$, $^{25}Mg/^{24}Mg$, $^{26}Mg/^{24}Mg$ and $^{26}Al/^{27}Al$ as a function of the $^{12}C/^{16}O$ ratio are shown in Figures 5.2, 5.3 and 5.4. They are grouped together by metallicity in order to show the differences in behaviour between stars of different mass. In the case of Figure 5.2 the $1.5\,M_\odot$ model is represented by a single point because no TDUP occurred before the model sequence was terminated (owing to numerical instabilities). The last panel of this figure shows a decline in the $^{26}Al/^{27}Al$ ratio because ^{26}Al is an unstable isotope and decays to ^{26}Mg during the course of the evolution.

In the case of the 1.5 and $3\,M_\odot$ models the $^{12}C/^{13}C$ ratios rise with the C/O ratio. This is to be expected because TDUP brings ^{12}C-rich material into the envelope. The different metallicities show the same rate of increase in the $^{12}C/^{13}C$ ratio. For the $5\,M_\odot$ models, HBB is seen to deplete the star of carbon-12, reducing the C/O ratio below that with which it entered the TP-AGB. The $^{12}C/^{13}C$ ratio is also seen to decrease and in each case reaches the CNO equilibrium value of around 4. Measurements of mainstream SiC

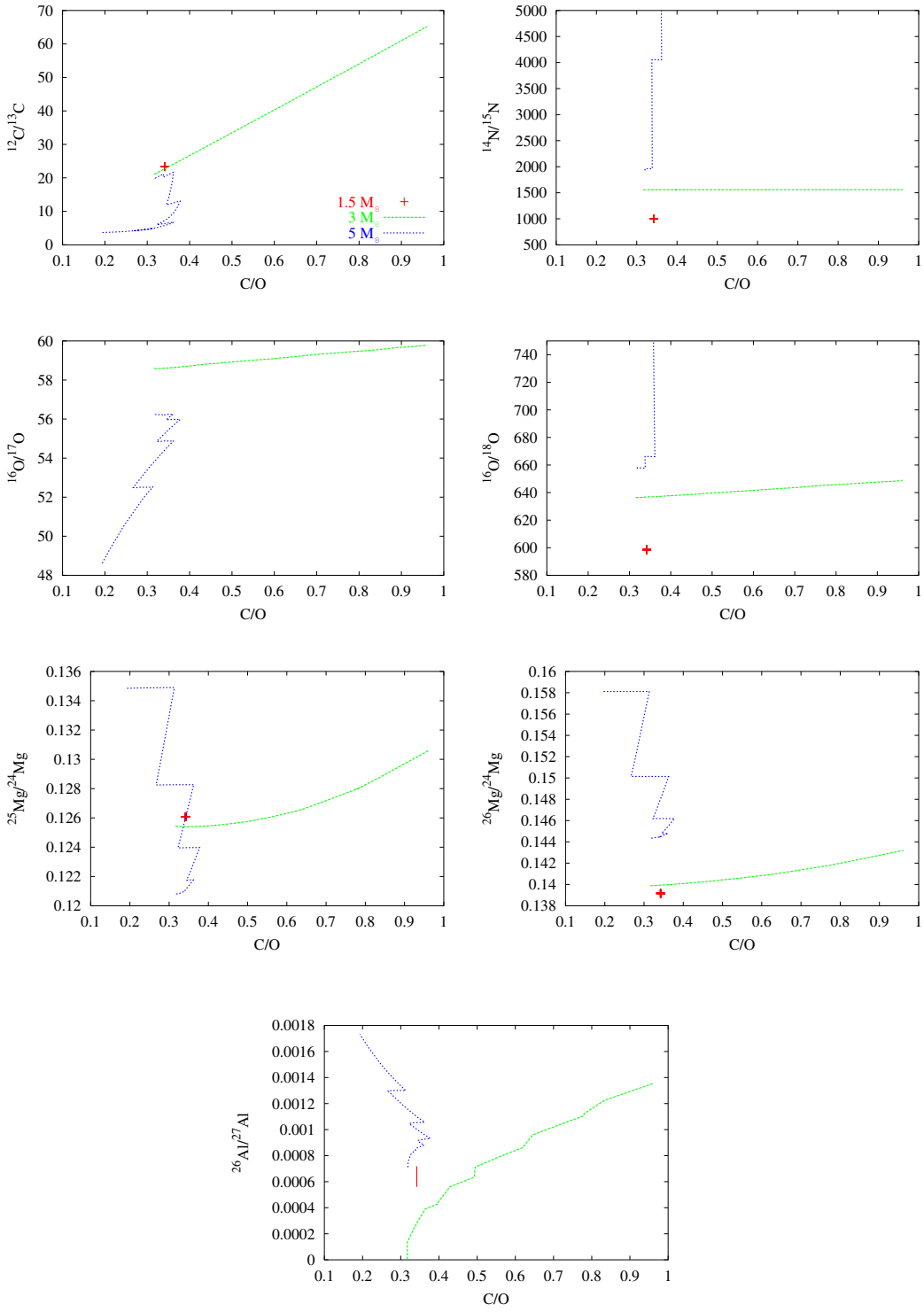

Figure 5.2: Evolution of various isotope ratios as a function of the $^{12}C/^{16}O$ ratio for stars of $Z = 0.02$. The $1.5\,M_\odot$ model is depicted in red and in most cases is just a single point because no dredge-up was obtained in the model. A decline in the $^{26}Al/^{27}Al$ ratio is observed because ^{26}Al is an unstable element. The $3\,M_\odot$ model is in green and the $5\,M_\odot$ model is in blue. All tracks begin with a C/O ratio of around 0.3.

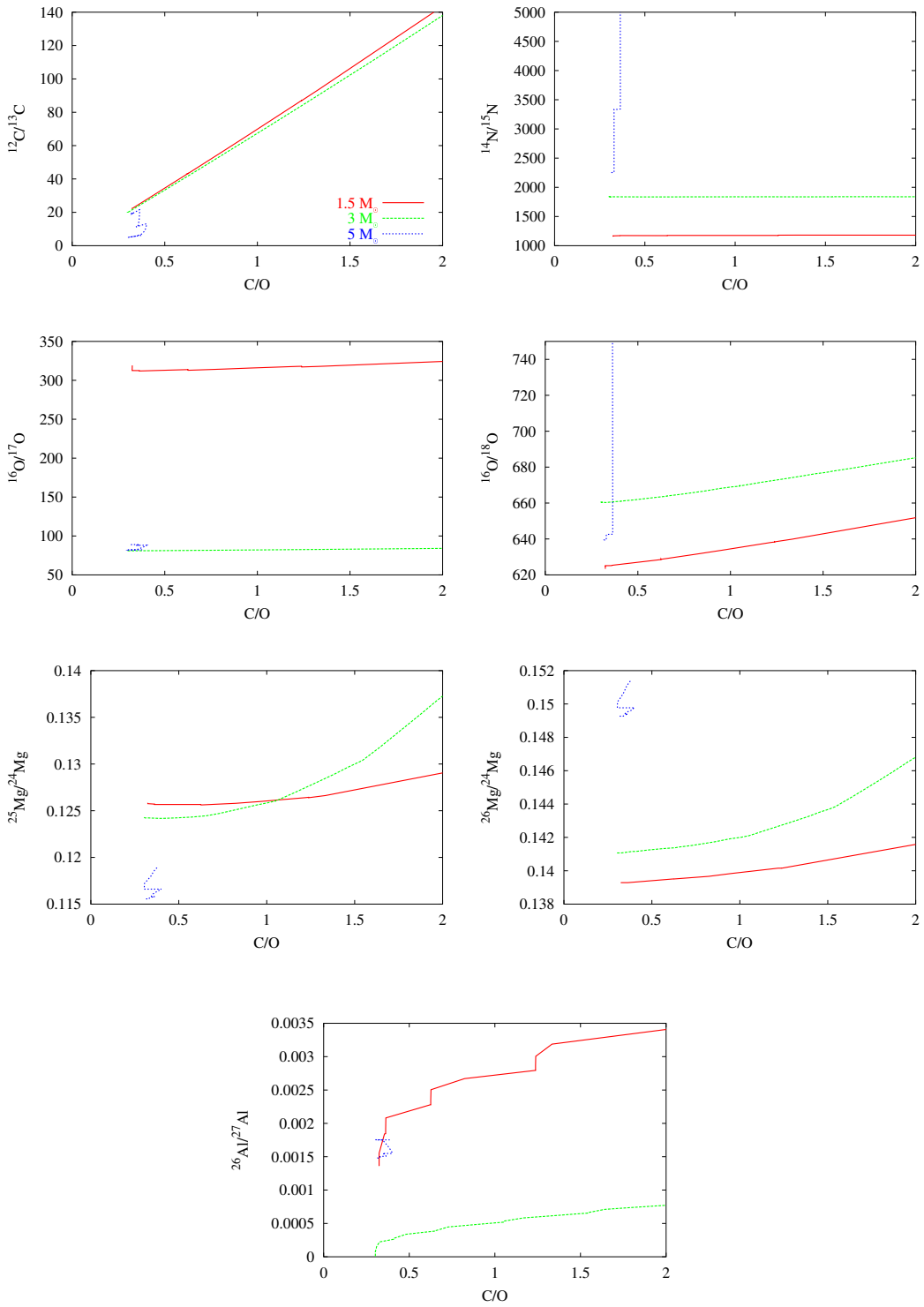

Figure 5.3: Evolution of various isotope ratios as a function of the $^{12}C/^{16}O$ ratio for stars of $Z = 0.008$. The $1.5\,M_\odot$ model is depicted in red, the $3\,M_\odot$ model is in green and the $5\,M_\odot$ model is in blue. All tracks begin with a C/O ratio of around 0.3

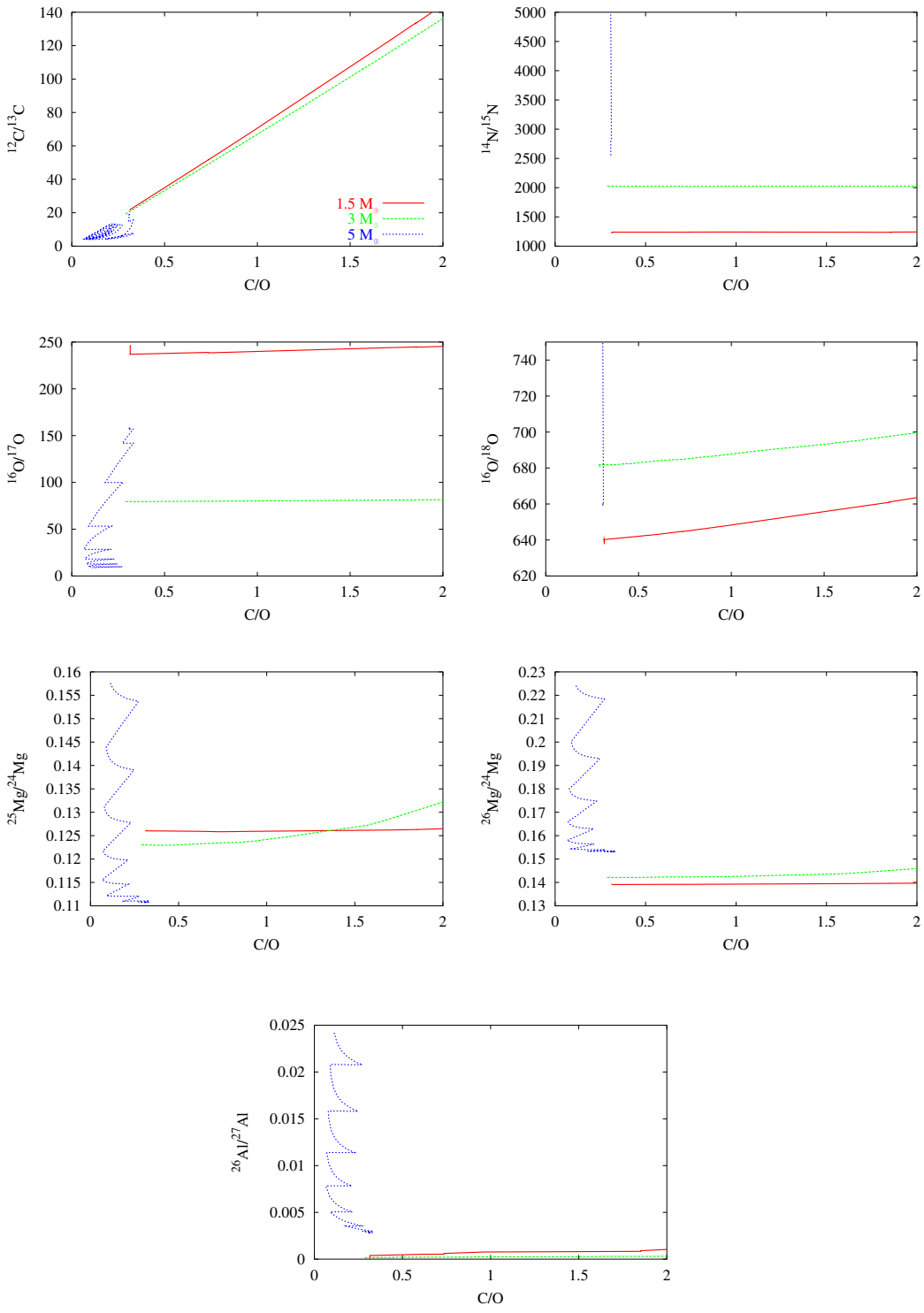

Figure 5.4: Evolution of various isotope ratios as a function of the $^{12}C/^{16}O$ ratio for stars of $Z = 0.004$. The $1.5\,M_\odot$ model is depicted in red, the $3\,M_\odot$ model is in green and the $5\,M_\odot$ model is in blue. All tracks begin with a C/O ratio of around 0.3

grains show $^{12}C/^{13}C$ ratios from 10 to 100. Assuming that these grains form at C/O$>$ 1 then the models provide ratios around the upper end of this range with $^{12}C/^{13}C$ ratios of around 60 when C/O is around unity. There seems to be little variation with mass (at least among the low-mass stars) and metallicity. The models therefore seem unable to account for the lower $^{12}C/^{13}C$ ratios observed in SiC grains. However, a model such as the $4\,M_{\odot}$ $Z = 0.02$ presented in Chapter 3 which starts to undergo HBB just after it becomes a carbon star may be able to provide these lower ratios. The CNO cycle has an equilibrium $^{12}C/^{13}C$ ratio of around 4 and so its action will lower the ratio. Another possibility is that some extra mixing mechanism is active in these stars. This would mix envelope material to hotter temperatures allowing greater CNO cycling and lowering the $^{12}C/^{13}C$ ratio.

The $^{14}N/^{15}N$ ratios predicted by the models are also in agreement with measurements of pre-solar SiC grains. These predict ratios of between 200 and 20000. It seems that at lower metallicities the $^{14}N/^{15}N$ ratio becomes higher at the TP-AGB. Along the TP-AGB there is little variation in the ratio for the 1.5 and $3\,M_{\odot}$ models. The $5\,M_{\odot}$ models all show rapid enhancements in the $^{14}N/^{15}N$ ratio which is to be expected because these objects undergo HBB, i.e. CNO cycling at the base of their envelopes.

Information on oxygen isotopic ratios comes, unsurprisingly, from the oxide rich grains which are presumed to have formed in an environment where C/O$<$1. The $^{16}O/^{17}O$ and $^{16}O/^{18}O$ ratios in a large sample of corundum grains have been measured by Nittler et al. (1997). They find $^{16}O/^{17}O$ ratios of between 350 and 3600 and $^{16}O/^{18}O$ ratios of between 165 and over 5000. In addition, recent measurements of spinel grains by Zinner et al. (2004) have yielded $^{16}O/^{17}O$ ratios of between 500 and 5000, together with $^{16}O/^{18}O$ ratios of between 350 and 20000. The models presented in this chapter are all consistent with the measured $^{16}O/^{18}O$ ratios. In the case of the low-mass models there is a slight elevation in the ratio as ^{16}O is present in the ashes of He burning that are brought to the surface during TDUP. The high mass models display massive enhancements in the $^{16}O/^{18}O$ ratio because HBB destroys ^{18}O.

The $^{16}O/^{17}O$ ratios prove more problematic. The models are all consistently lower that the lowest grain measurements. The change in this ratio occurs primarily at first dredge-up when material that is ^{17}O rich is brought

to the surface (Boothroyd et al., 1994). In low-mass stars the effects of third dredge-up on the $^{16}O/^{17}O$ ratios are limited. A slight increase in the ratio occurs because ^{16}O is brought to the surface by TDUP. In the intermediate-mass stars HBB can create ^{17}O at the expense of ^{16}O and so the $^{16}O/^{17}O$ ratio drops (Boothroyd et al., 1994). This is exactly the behaviour that is seen in these models although the actual value of the ratio obtained does not fit the measurements. This is not surprising because there is a large uncertainty in the $^{17}O(p,\gamma)^{18}F$ reaction rate and many different simulations predict very different $^{16}O/^{17}O$ ratios (Nittler et al., 1997). This rate needs to be varied within the simulations in order to determine if it can produce ratios closer to the observed values. However such a sequence of runs would be time-consuming given the current status of the code and has not yet been attempted.

On the TP-AGB magnesium isotopes can be produced in two regions of the star the helium-rich intershell and the hydrogen-burning shell. At temperatures above around 3.5×10^8 K (which may be reached during the thermal pulses) the reaction $^{22}Ne(\alpha,n)^{25}Mg$ can occur (a possible source of neutrons for the *s*-process) but this temperature is not reached in stars of around one solar mass. Note that for all metallicities, the $1.5\,M_\odot$ models show virtually no change in their magnesium ratios. The $3\,M_\odot$ models show slight enhancements in both of the heavy Mg isotopes. In the H-burning shell, the Mg-Al cycle is expected to be active at temperatures of around 3×10^7 K and will deplete ^{25}Mg and produce ^{26}Al (Arnould et al., 1999). While this temperature is reached in both the 1.5 and $3\,M_\odot$ models the effects are limited and only slight depletions would be expected in the $1.5\,M_\odot$ models. The production of magnesium in the $3\,M_\odot$ models swamps the effects of the H-burning shell. In the $5\,M_\odot$ models the effects of both production sites are clearly visible. When TDUP occurs and the C/O ratio is temporarily enhanced both magnesium isotope ratios are enhanced, reflecting the dredging up of material from the intershell. Increases in both ratios are again observed as the C/O ratio is reduced owing to the action of HBB during the interpulse phase. The Mg-Al cycle is active during this phase and both ^{25}Mg and ^{26}Mg are produced.

Isotopic ratios for magnesium have been measured in both carbon-rich and oxygen-rich grains. In SiC and corundum the ^{26}Mg contribution is dominated by the decay of ^{26}Al due to high aluminium to magnesium ratios (Zin-

ner et al., 2004). These grains are generally used to infer $^{26}Al/^{27}Al$ ratios and give rather imprecise measurements of $^{25}Mg/^{24}Mg$ owing to low magnesium concentrations. However, magnesium-rich spinel grains afford a much more precise look at both the $^{25}Mg/^{24}Mg$ and $^{26}Mg/^{24}Mg$ ratios. Zinner et al. (2004) measured the magnesium ratios in 23 spinel grains. Excluding the exceptional grain OC2 they found that the $^{25}Mg/^{24}Mg$ ratio was between 0.118 and 0.151 while the $^{26}Mg/^{24}Mg$ ratio was between 0.143 and 0.226. The models presented in this section are all capable of producing magnesium ratios within these ranges.

Finally, the $^{26}Al/^{27}Al$ ratios also fit the measured ratios from pre-solar grains. Measurements of oxide grains give ratios in the range 10^{-4} to around 0.02 (Nittler et al., 1997), while in SiC the range is narrower[1], being roughly $1 - 4 \times 10^{-3}$ (Amari et al., 2000). ^{26}Al is produced in the H-burning shell as described above. In the case of low-mass stars, it only reaches the surface when TDUP occurs and so an increase in the $^{26}Al/^{27}Al$ ratio is correlated with a rise in the C/O ratio. For the intermediate-mass models, the effects of HBB and the Mg-Al cycle can clearly be seen. As the C/O ratio is decreased during the interpulse period, the $^{26}Al/^{27}Al$ rises while it is constant as TDUP takes place.

Fluorine

The production site of ^{19}F has been a major puzzle for nucleosynthesis for a long time. It was predicted by Goriely et al. (1989) that ^{19}F should be manufactured in asymptotic giant branch stars. The sequence of reactions that produces ^{19}F is

$$^{14}N(\alpha,\gamma)^{18}F(\beta^+)^{18}O(p,\alpha)^{15}N(\alpha,\gamma)^{19}F. \tag{5.7}$$

Protons are provided by $^{14}N(n,p)^{14}C$ if a source of neutrons exists, such as the $^{13}C(\alpha,n)^{16}O$ reaction. Other sites and mechanisms for the Galactic production of fluorine have been proposed. The neutrino process operating during type-II supernovae can produce fluorine (Woosley & Weaver, 1995). Fluorine can also be synthesized during core He-burning (via the pathway given above) and ejected via the strong winds of Wolf-Rayet stars (Meynet &

[1]This excludes those SiC grains of type X which are believed to come from supernovae.

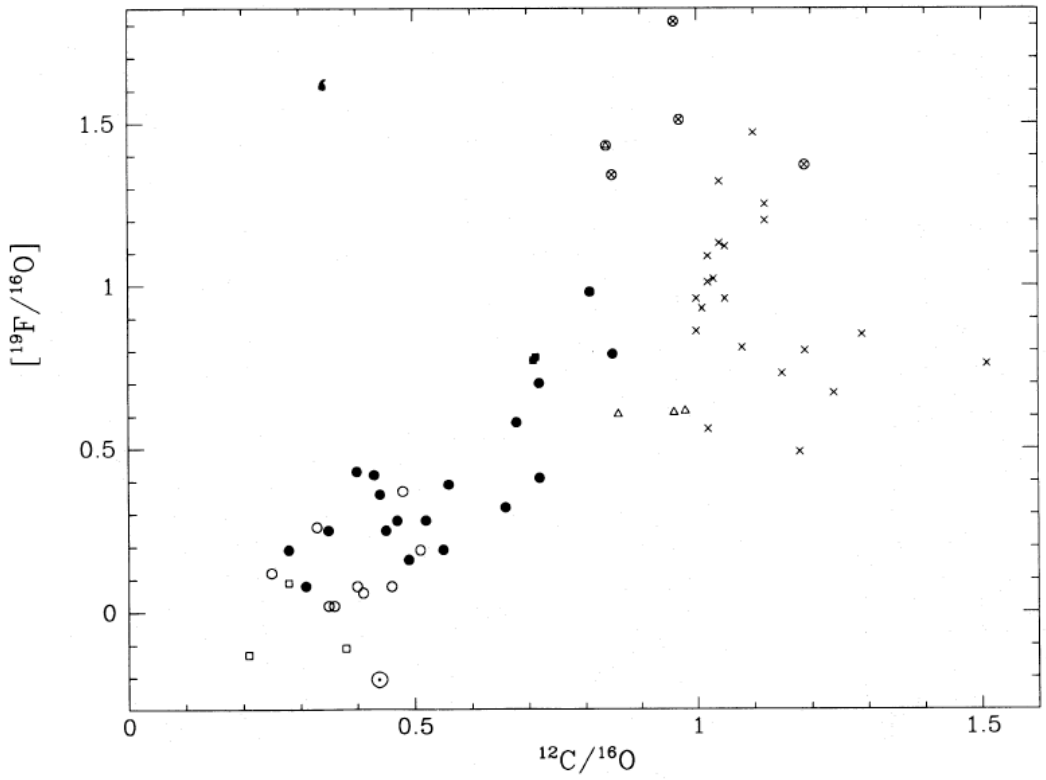

Figure 5.5: Observed ^{19}F abundances in AGB stars (Figure 6 from Jorissen et al., 1992). Open squares are K stars; filled squares are Ba star; open circles are M stars; filled circles are S stars; circles with crosses are SC stars; crosses are N stars and triangles are J stars. Note that $[^{19}\mathrm{F}/^{16}\mathrm{O}]$ is with respect to the fluorine abundance in K giants, not the solar abundance.

Arnould, 1993, 2000). It appears that the contributions of asymptotic giant branch and WR stars must be included in the computation of the chemical evolution of the Galaxy to account for the observations of fluorine in the Milky Way (Renda et al., 2004).

Currently the only observationally confirmed site for fluorine production is in AGB stars (Jorissen et al., 1992). Figure 5.5 shows the observed ^{19}F abundance with respect to the C/O ratio (Figure 6 from Jorissen et al., 1992). There is a strong correlation of ^{19}F with C/O ratio. This is to be expected because ^{19}F is formed in the helium rich intershell and can only reach the surface by the action of TDUP. Figures 5.6, 5.7 and 5.8 show evolution of the surface fluorine abundance in the nine models generated with the STARS code. These figures show that, at a fixed mass, more fluorine is produced

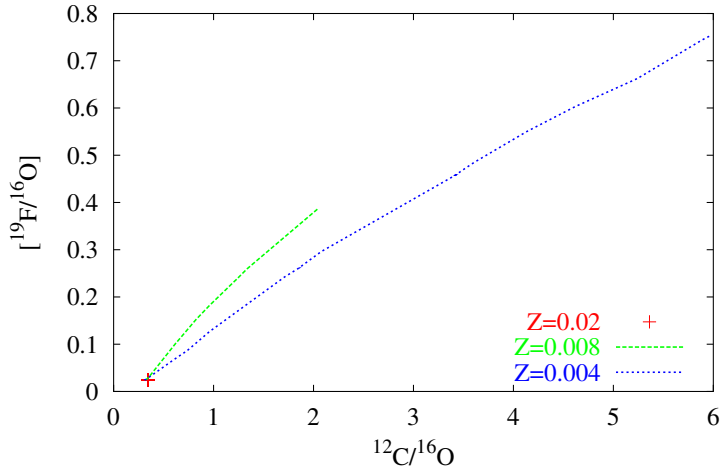

Figure 5.6: Fluorine-19 abundance as a function of $^{12}C/^{16}O$ for the $1.5\,M_{\odot}$ models. The $Z = 0.02$ is represented by a single point as no TDUP was obtained from this model.

at higher metallicities owing to the fact that the chain that produces ^{19}F starts from ^{14}N which is a secondary isotope. The lower metallicity tracks also appear flatter as a single TDUP event leads to a greater C/O ratio due to the lower oxygen abundance.

The $5\,M_{\odot}$ models show completely different behaviour from the lower mass ones. Initially their C/O ratios increase due to the occurrence of TDUP but HBB quickly sets in (usually after as little as 2 TPs with TDUP) and the C/O ratio is steadily depleted. As this happens, there is also a depletion in the fluorine abundance. While ^{19}F is still being produced in the intershell region and to a lesser degree by proton captures involving ^{18}O in the H-burning shell, it is depleted by $^{19}F(p,\gamma)^{20}Ne$ in the hydrogen burning shell.

Note that none of the models presented here are able to reproduce the observed fluorine abundances. What could be the reason for this? Some of the discrepancy could be accounted for by uncertainties in the reaction rates. Lugaro et al. (2004) studied the effects of reaction rate uncertainties on fluorine production using models from the MSSSP code. They found that the yield could be affected by as much as 50% for models of around $3\,M_{\odot}$. Other possibilities include the fact that the STARS code does not produce a ^{13}C pocket which could provide the mechanism to generate additional protons (via neutron production and subsequent capture by ^{14}N) required by

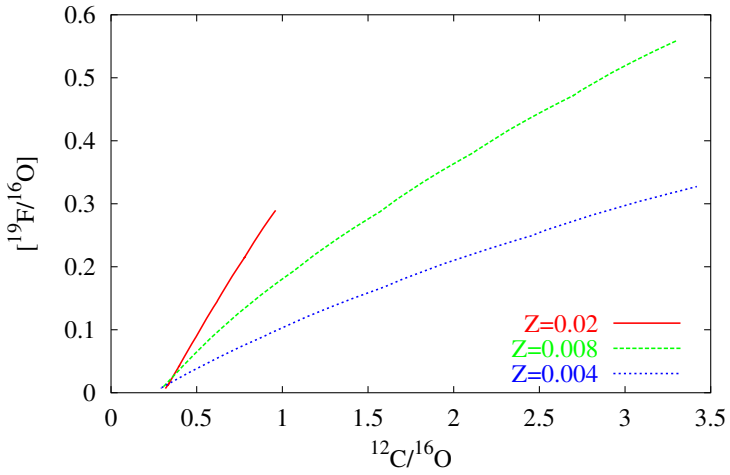

Figure 5.7: Fluorine-19 abundance as a function of $^{12}C/^{16}O$ for the $3\,M_{\odot}$ models.

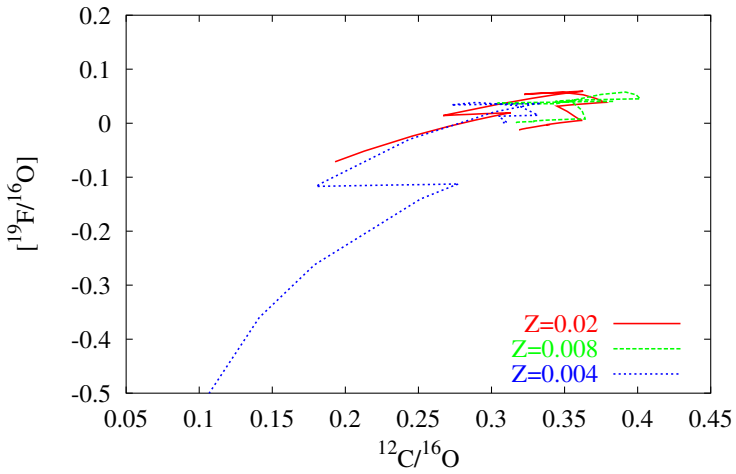

Figure 5.8: Fluorine-19 abundance as a function of $^{12}C/^{16}O$ for the $5\,M_{\odot}$ models. Note that fluorine becomes depleted in these models due to the reaction $^{19}F(p,\gamma)^{20}Ne$ occurring in the H-burning shell.

the reaction path. Additional protons could also be mixed into the inter-shell region by extra mixing processes (convective overshooting, rotational mixing, internal gravity waves). Lugaro et al. (2004) also suggest that some cool-bottom processing (i.e. extra mixing process) might deplete the carbon abundance slightly without affecting the fluorine. This solution is perhaps less desirable for the STARS code. The LMC carbon star luminosity function can be reproduced with the STARS models. Any adjustment to the carbon abundance may disrupt the fit to this observation.

Lithium

Lithium is an element whose origins are poorly understood. It is expected to be produced in AGB stars of intermediate mass. In these stars a process known as the Cameron-Fowler mechanism is expected to operate (Sackmann & Boothroyd, 1992). This mechanism involves the production of ^{7}Be by the reaction $^{3}\mathrm{He}(\alpha,\gamma)^{7}\mathrm{Be}$ in a region deep in a stellar interior where there is convection outward to cooler regions (Cameron & Fowler, 1971). The beryllium can then decay by electron capture to form lithium-7 in cooler regions where the reaction $^{7}\mathrm{Li}(\mathrm{p},\alpha)^{4}\mathrm{He}$ is not rapid enough to destroy the lithium. In order to produce ^{7}Be temperatures of around 10^{7} K are required. Temperatures of 10^{7} K are reached in the H-burning shells of AGB stars, and in the case of intermediate-mass stars, the convective envelope extends down as far as this shell and there is hot-bottom burning. Thus the Cameron-Fowler mechanism is expected to operate in intermediate mass TP-AGB stars.

Figure 5.9 shows the evolution of the surface lithium abundance as a function of the star's mass. The lithium abundance is expressed as

$$\log \epsilon(^{7}\mathrm{Li}) = \log \frac{N(^{7}\mathrm{Li})}{N(^{1}\mathrm{H})} + 12 \tag{5.8}$$

where N is the number density of that element. Initially the lithium abundance drops as the envelope delves into layers that are hot enough to deplete ^{7}Li by proton captures but not hot enough to allow the production of ^{7}Be. This initial drop happens at a lower total stellar mass at lower metallicity because TDUP occurs sooner at lower metallicity. As TDUP deepens and the temperature at the base of the convective envelope becomes hotter

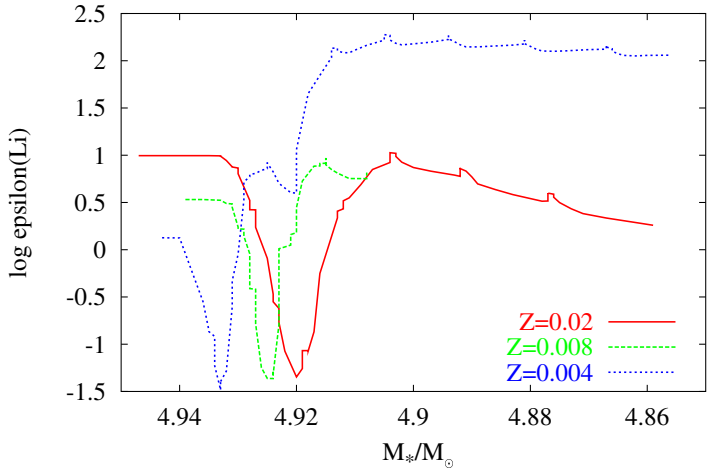

Figure 5.9: Plot of the evolution of $\log \epsilon(^7\mathrm{Li})$ (see main text for the definition) at the surface of the star as a function of the star's mass at that time. The initial mass of each star was $5\,\mathrm{M}_\odot$.

^{7}Be can be produced and this rapidly decays to ^{7}Li. While the $Z = 0.02$ and $Z = 0.008$ models produce similar amounts of lithium, the $Z = 0.004$ produces much more, reaching $\log \epsilon(^7\mathrm{Li}) \approx 2.2$. These results do not agree with those of Travaglio et al. (2001) whose models were computed with the MSSSP and its post-processing code. They found that their $5\,\mathrm{M}_\odot$ models of $Z = 0.02, 0.008$ and 0.004 all produced a peak lithium abundance of $\log \epsilon(^7\mathrm{Li}) \approx 4$. However, they note that lithium production is sensitive to the mass loss rate used and their models are evolved with the Vassiliadis & Wood (1993) formalism. Another possibility is that the mixing in the STARS code is not fast enough to allow all the ^{7}Be that is formed to be moved to cooler regions before it can react with the present protons.

The models compare reasonably well to observations though there are some discrepancies. Smith et al. (1995) surveyed 112 red giants in the LMC and SMC. In both populations, they observed lithium abundances of $\log \epsilon(^7\mathrm{Li}) \approx 1.0 - 4.0$. The luminosity of these objects was consistent with the luminosity of intermediate-mass AGB stars undergoing HBB. While the lower abundances are consistent with the models presented here, the upper ones cannot be reproduced. Again, this may point to a problem with some of the physics in the STARS code.

5.3 The ^{13}C Pocket: a Warning on Numerical Diffusion

The nucleosynthesis subroutines make it possible to investigate the formation of a carbon-13 pocket in the intershell region of AGB stars. It is believed that such a pocket must occur in order to provide a neutron source, the reaction $^{13}\mathrm{C}(\alpha,\mathrm{n})^{16}\mathrm{O}$ in low-mass AGB stars. A pocket forms if small quantities of protons are mixed into the carbon-rich intershell at the end of third dredge-up. However, the physical mechanism for such mixing has yet to be established.

The $Z = 0.02$ $3\,\mathrm{M}_{\odot}$ model was used to look at the formation of a ^{13}C pocket in the STARS models. The episode of TDUP immediately after the 12^{th} thermal pulse was used because, by this point, TDUP is well established in the model. The left hand panels of Figure 5.10 show the evolution of the mass profiles of hydrogen, ^{12}C, ^{13}C and ^{14}N towards the end of the episode of TDUP. The top panel is taken from just before the end of TDUP. As expected the composition profiles show a sharp discontinuity as the envelope, of one composition, is pushing downward into the intershell region (the lower mass region in the plots) which has an entirely different composition. In the second panel down, the discontinuity is seen to have become softer and there is a steep but smooth transition in the abundance profiles from the intershell to the envelope. This means that there are now small quantities of protons present in the ^{12}C-rich regions. These protons are captured by the ^{12}C and a pocket of ^{13}C is formed (third panel down on the left hand side of Figure 5.10). In fact, protons are present in sufficient quantities that the ^{13}C also captures protons to form a substantial pocket of ^{14}N, as can be seen in the bottom left-hand panel of Figure 5.10.

The formation of a ^{13}C-pocket within the model is disturbing: it is generally believed that there should be no mixing of protons into the ^{12}C-rich intershell if only standard mixing (i.e. only in those regions where $\bigtriangledown_{\mathrm{r}} > \bigtriangledown_{\mathrm{ad}}$) is applied. So why do protons end up in the intershell region? The answer is numerical diffusion. Suppose a profile with a sharp discontinuity is set up over a series of mesh points as depicted by the solid line in Figure 5.11, with the black circles representing the location of the mesh points. If the mesh points move inward in mass, as indicated, to the locations marked by

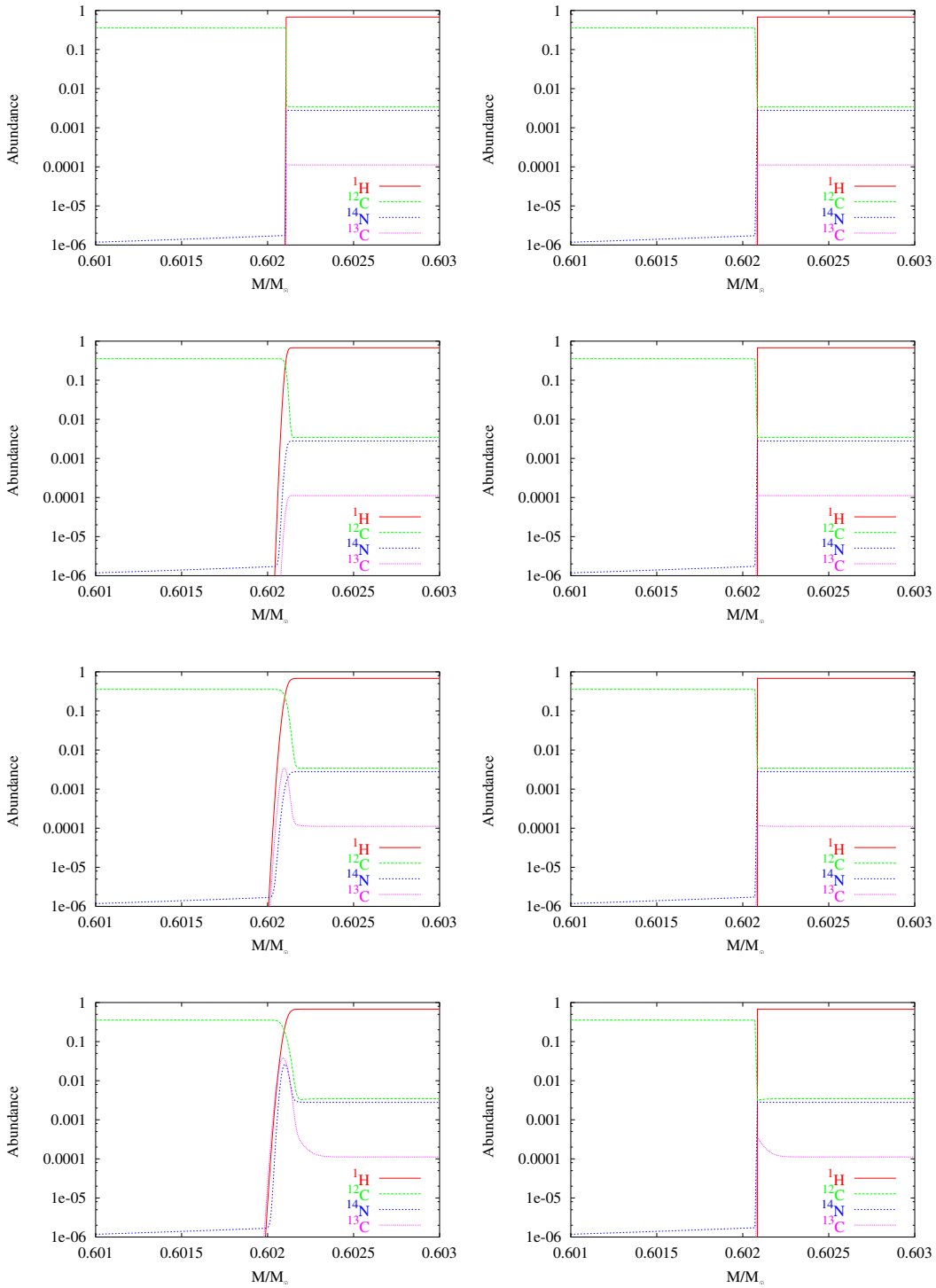

Figure 5.10: Evolution of the mass profiles of elements related to the formation of a ^{13}C pocket. The panels on the left are calculated with the fully adaptive mesh while those on the right are calculated with the 500 outermost mesh points fixed in mass from just before the end of TDUP. Note the movement of protons into the ^{12}C-rich intershell in the left hand panels and the subsequent formation of a ^{13}C-rich region. The profiles in both columns are taken at approximately similar times.

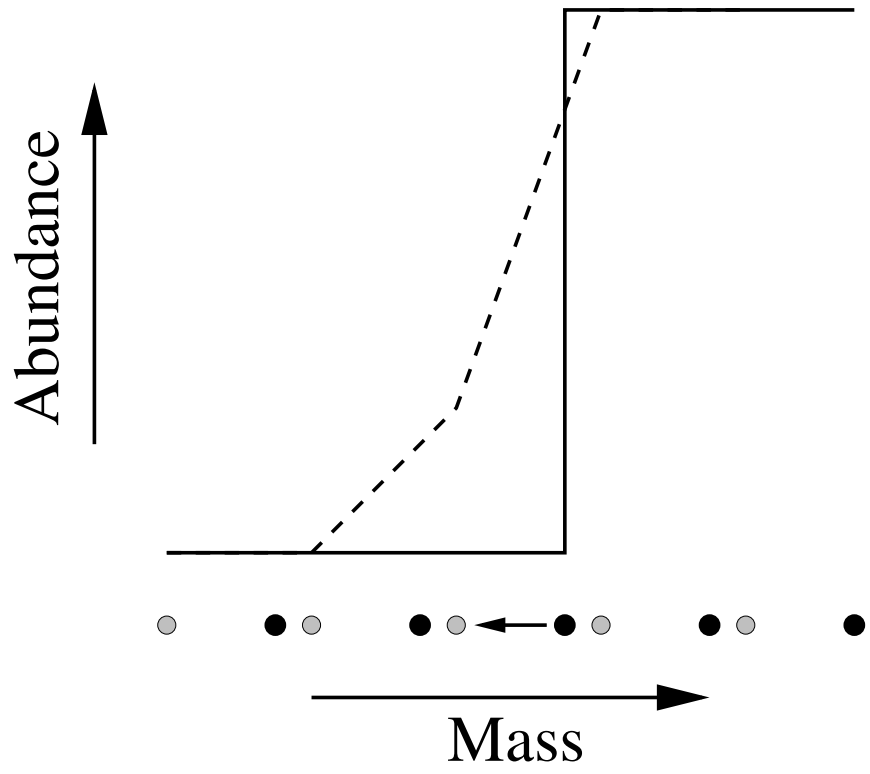

Figure 5.11: A schematic depiction of why numerical diffusion occurs. A sharp abundance profile (solid line) is set up over a few mesh points (black dots). If the mesh points then move in mass to the positions indicated by the grey circles, the abundance profile is modified to that indicated by the dashed line.

the grey circles, the profile is modified to that indicated by the dashed line. This is because when a mesh point moves the code works out the value of the abundance (or whatever the quantity being considered is) at the new location from the values from the old mesh point locations surrounding the new one. This inevitably leads to the sharp profile being smeared out. It is an unfortunate and very much undesirable consequence of using an adaptive mesh.

The only way to prevent numerical diffusion is to prevent the movement of the mesh points. This can be achieved using the viscous mesh. Instead of fixing the mass location of the innermost mesh points, the outer ones can be fixed instead, so that none of the mesh points in the envelope (and part of the intershell) are able to move. However, as numerical diffusion only becomes

a serious issue once TDUP has finished[2] the outer mesh points need only be fixed when the end of TDUP is approached. This retains the maximum resolution possible in the interface between the envelope and the intershell so that TDUP can be accurately calculated (see the discussion in Straniero et al., 1997, regarding the need for high spatial resolution).

From the same initial model as the previous run, the $3\,M_{\odot}$ model was evolved through TDUP and part of the interpulse period. This time the 500 outermost mesh points were fixed just before the end of TDUP. The profiles of the ^{1}H, ^{12}C, ^{13}C and ^{14}N are shown on the right hand panels of Figure 5.10. As with the original run, TDUP initially gives a sharp discontinuity in the abundance profiles. TDUP also proceeds to the same depth as it did in the original run so the resolution must be comparable in both calculations. The sharp discontinuity in the abundance profiles is retained throughout the interpulse unlike in the original run. There is no mixing of protons into the carbon-rich intershell and so no ^{13}C pocket is formed. This shows that the pocket obtained in the original run was indeed the result of a numerical, rather than a physical effect. With this established, and now knowing that the numerical diffusion can be suppressed by locking the mesh it is also possible to investigate additional mixing mechanisms (e.g. rotational mixing) to see if they are able to produce a ^{13}C pocket. This investigation is to be carried out in the future.

5.4 Summary

The minor isotope evolution subroutines of the STARS code have been extensively updated. These subroutines have been used to investigate the nucleosynthesis of light elements during the TP-AGB. Nine models have been produced at three masses across three metallicities and mass-loss has been included. The surface abundances of the models have been compared to known observational constraints.

The models do a very good job of reproducing the known constraints on AGB stars from pre-solar grains. Most of the isotopic ratios are well matched by the models though there are problems with the $^{16}O/^{17}O$ ratio. These may be due to uncertainties in the reaction rates. The models presented are unable

[2]Prior to this the actual physical changes swamp the effects of numerical diffusion.

to reproduce the observed abundances of fluorine in AGB stars. This may be due to the absence of a ^{13}C pocket and/or additional mixing processes. The intermediate-mass models are able to reproduce some of the observations of lithium abundance in AGB stars though they are not able to account for the most extreme lithium enrichment. This suggests there is a problem with the physics in the STARS code as other codes are able to give sufficiently high lithium abundances.

The nucleosynthesis routines have also been applied to make a preliminary assessment of whether the STARS code can be used to investigate the formation of a ^{13}C pocket. It was found that the code produces such a pocket for numerical, rather than physical, reasons owing to the motion of its mesh points. This behaviour is undesirable and it was found that it could be suppressed with the viscous mesh applied to the outermost mesh points. The STARS code is therefore suitable for use to investigate the formation of a carbon-13 pocket.

Chapter 6

Post-AGB Stars

In this chapter, the evolution of a star as it leaves the TP-AGB is discussed. In the course of attempting to produce post-AGB models, a new mode of behaviour not reported in the literature was found. It was determined to be an artifact caused by numerical diffusion. A model of a post-AGB object undergoing a late thermal pulse has also been computed and TDUP is found to occur after the pulse without convective overshooting in contrast to many other simulations.

6.1 The End of the TP-AGB

The TP-AGB is finally brought to an end when mass loss strips the last remnants of the envelope from the star. As this happens the star moves to hotter temperatures at constant luminosity and eventually moves on to the white dwarf cooling track. Simulations of this phase of evolution have been done by several authors (e.g. Schönberner 1979;Wood & Faulkner 1986;Vassiliadis & Wood 1994). Particular interest has gone into the production of hydrogen deficient models in an attempt to explain the origin of objects like those of the PG 1159 class (Blöcker, 2001).

The fate of a star as it leaves the TP-AGB depends on the phase of the thermal pulse cycle at which the last remnants of the envelope are removed (i.e. when the envelope mass drops as low as $10^{-2}\,M_{\odot}$). If the hydrogen burning shell is inactive when the envelope is removed then the object proceeds straight to the white dwarf cooling track, becoming a hydrogen-rich white dwarf. This requires the object to leave the AGB straight after the

occurrence of a thermal pulse.

It is possible for a thermal pulse to occur after the object has left the TP-AGB. In such cases, sufficient helium has been produced by hydrogen-burning that as the object contracts the helium can heat up and ignite. If the star was close to the end of its thermal pulse cycle (i.e. in the interpulse phase) when the envelope mass is reduced to around $10^{-4}\,\mathrm{M}_{\odot}$ then the pulse occurs as the object is crossing the HR-diagram to the white dwarf cooling track. This is known as a late thermal pulse (LTP). Owing to the hydrogen burning shell still being active at this time, the intershell convection zone is inhibited from penetrating into the hydrogen envelope by the existence of an entropy barrier, in the same way as it is on the TP-AGB (Iben, 1976). If TDUP were to occur following this pulse, the tiny envelope would be significantly enriched in carbon and depleted in hydrogen. However standard evolutionary calculations (i.e. those not including convective overshooting) have not produced TDUP to date (Blöcker & Schönberner, 1997).

If mass loss is sufficiently strong it is possible for the object to reach the white dwarf cooling track before the helium ignites. If helium ignition occurs on the white dwarf cooling track a very late thermal pulse (VLTP) is the result. In this case the hydrogen burning shell is extinguished and there is no barrier to the intershell convection zone. The intershell convection zone may penetrate into the hydrogen rich envelope and this can result in a significant depletion of hydrogen and the potential for interesting nucleosynthesis. The first such model was produced by Iben & MacDonald (1995).

Both types of pulse cause the envelope to expand once again, briefly returning the star to the AGB – the so-called born again scenario. The VLTP scenario has recently received much attention in the literature (Herwig 2002; Lawlor & MacDonald 2003; Althaus et al. 2005) because VLTPs are believed to explain the behaviour of objects like FG Sagittae (Herbig & Boyarchuk, 1968) and Sakurai's Object (V4334 Sgr) (Duerbeck & Benetti, 1996).

6.2 Producing a Post-AGB Model

The $Z = 0.008$ $1.5\,\mathrm{M}_{\odot}$ model begun in the previous chapter was used to create a post-AGB object by continuing its evolution, with the same evolutionary parameters. A total of 10 thermal pulses are evolved through before the star

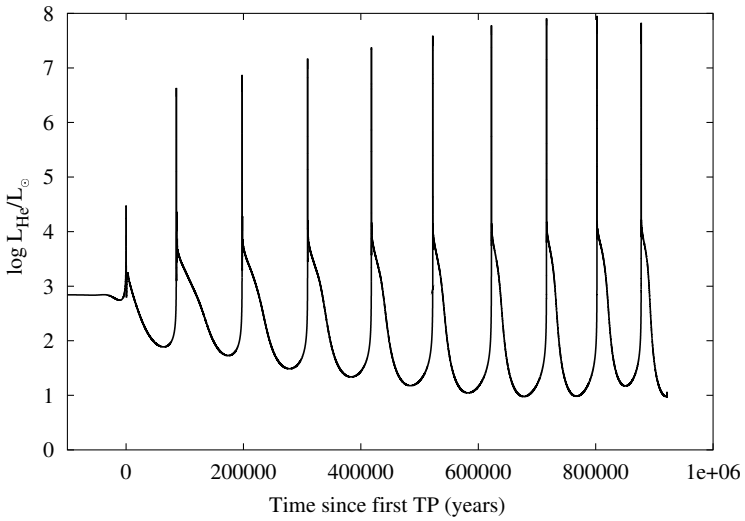

Figure 6.1: The evolution of the helium luminosity with time since the first thermal pulse. The plot ends just as the star leaves the TP-AGB.

loses enough of its envelope that it leaves the TP-AGB. The evolution of the helium luminosity with time since the first thermal pulse (TP) is shown in Figure 6.1. Third dredge-up (TDUP) is found to occur from the fourth pulse. In the last three pulses, when the envelope mass is low, numerical instabilities occur as the envelope tries to encroach into the H-exhausted core and begin the process of TDUP. In order to overcome these problems it has been necessary to turn off mixing by convection. This is done by allowing the model to run until the numerical problems become too severe (hence allowing some TDUP to occur) and then restarting the model with the convective mixing in the envelope switched off. Once the model reaches the interpulse phase the convective mixing is turned back on.

This certainly introduces an error in the composition of the envelope – it reduces the amount of carbon and other products of He-burning from the intershell that are seen at the surface. However, the efficiency of TDUP is expected to fall with a reduction in envelope mass (see e.g. Straniero et al., 2003) and hence the envelope composition may not be that different from what it would be if full TDUP were included. In order to test whether the subsequent behaviour depended on the carbon abundance of the model, the abundance of carbon throughout the envelope was enhanced by 10%. The behaviour was identical to the unenhanced case.

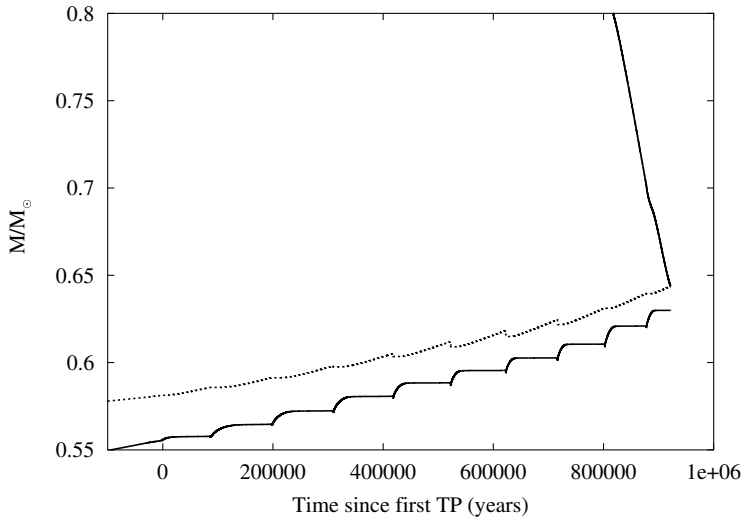

Figure 6.2: Plot of the evolution of the star's mass (upper solid line), H-exhausted core mass (dotted line) and He-exhausted core mass (lower solid line) as a function of time since the first thermal pulse. Element exhausted core masses are defined to be the mass at which the mass fraction for that element drops below 0.3.

In the interpulse phase following the 10^{th} pulse the mass of the star is finally reduced to just $0.6482\,\mathrm{M}_\odot$ and the star leaves the TP-AGB. At this point the H-exhausted core mass is $0.6432\,\mathrm{M}_\odot$ and the He-exhausted core mass is $0.6299\,\mathrm{M}_\odot$. A plot of the evolution of the star's total mass and the mass of the H- and He-exhausted cores as a function of time since the first thermal pulse is shown in Figure 6.2.

The star continues to lose mass and when its total mass is $0.6440\,\mathrm{M}_\odot$ a new phase of behaviour sets in. The luminosity of the star begins to rise and the surface temperature increases by nearly an order of magnitude. When the surface temperature reaches around 65,000 K the luminosity falls and the star's surface temperature begins to drop. Both the luminosity and surface temperature slowly return to close to their original values and the cycle repeats again. The timescale to complete one of these loops is extremely short – from the luminosity maximum in the first loop to the maximum in the next takes just 30 yrs. A plot of the star's evolutionary track in the HR-diagram is shown in Figure 6.3 for the first three such loops.

This cyclic behaviour is persistent and the evolution through over 100 repetitions has been calculated with Reimers mass-loss with $\eta = 1$ still ap-

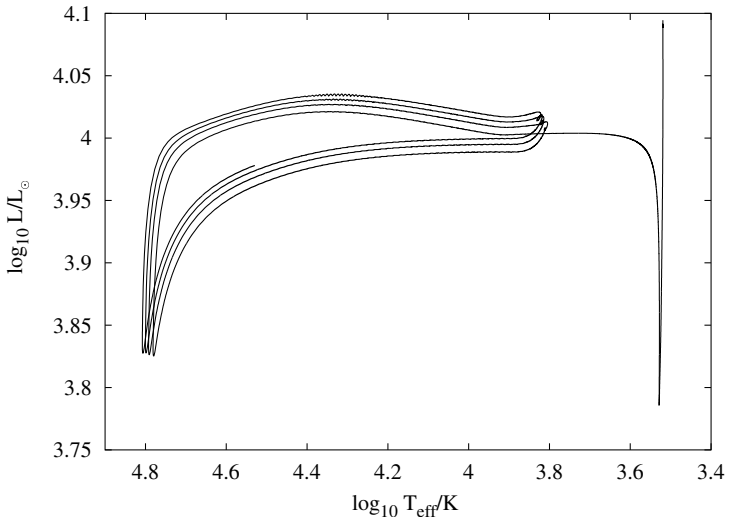

Figure 6.3: Hertzsprung-Russell diagram showing 3 loops following the star's transition off the TP-AGB.

plied. The evolution of luminosity with time is shown in Figure 6.4. The time taken to complete one loop is seen to decrease with time and the maximum luminosity reached in the loop increases with time as well. The variation of the surface luminosity seems to be caused by CNO cycling in the thin layer of hydrogen left on the surface of the star. When the loops start the temperature in the H-burning shell reaches over 6×10^7 K permitting CNO cycle reactions to take place. The surface abundance of CNO elements is also seen to change during the occurrence of the loops, with nitrogen being enhanced at the expense of carbon (see Figure 6.5).

This cyclic phenomenon does not appear to have been described in the literature. Is it really a consequence of the physics used by the evolution code or a numerical artifact? The phenomenon displays similar characteristics to the thermal pulses seen on the TP-AGB and it appears that it may be a Schwarzschild-Härm instability (Schwarzschild & Härm, 1965), i.e. a thermal instability. It is therefore necessary to test whether the shell is expected to be thermally unstable. To do this the criterion developed by Yoon, Langer & van der Sluys (2004) which is an extension of the original analysis by Schwarzschild & Härm (1965) is used.

To determine whether the H-shell is thermally unstable two quantities

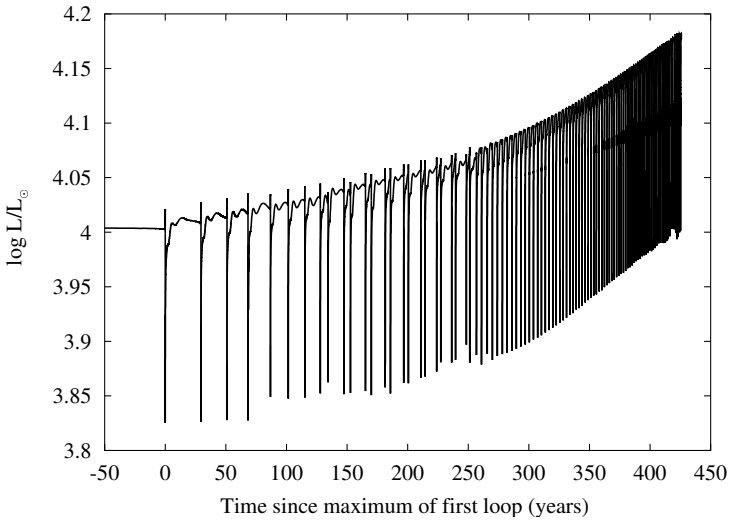

Figure 6.4: Plot of the evolution of the star's luminosity with time. Note that the period of the loops decreases with time.

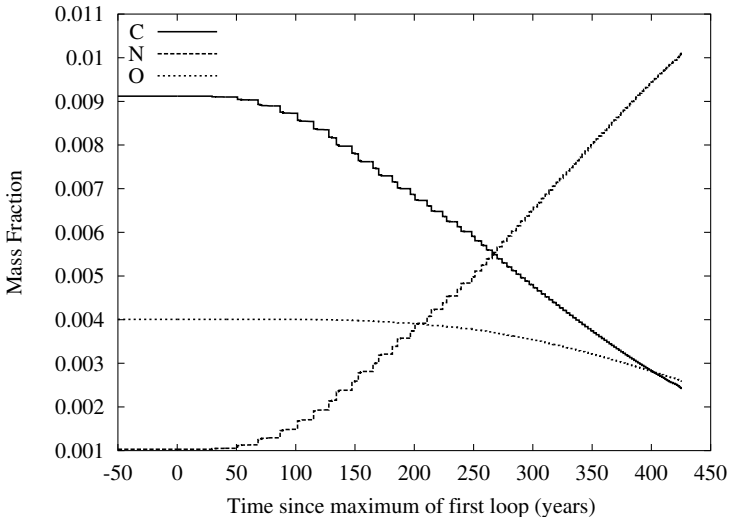

Figure 6.5: The evolution of the CNO elements at the surface of the star. Carbon (solid line) and oxygen (dotted line) are slowly being depleted as the nitrogen (dashed line) is enhanced. This is a clear signature of the CNO-cycle being active.

(equations 6 and 12 of Yoon et al., 2004) need to be evaluated. These are

$$c^* = c_{\rm P}\left(1 - \bigtriangledown_{\rm ad}\frac{\alpha_s\alpha_T}{\alpha_s\alpha_P - 1}\right) \tag{6.1}$$

and

$$\sigma = \frac{\nu - 4 + \kappa_T + \frac{\alpha_T}{\alpha_{\rm s}\alpha_P - 1}(\lambda + \alpha_{\rm s} + \kappa_P)}{c^*/c_{\rm P}}, \tag{6.2}$$

where

$$\begin{aligned}
\alpha_P &= \left(\frac{\partial \ln \rho}{\partial \ln P}\right)_T, \\
\alpha_T &= -\left(\frac{\partial \ln \rho}{\partial \ln T}\right)_P, \\
\alpha_{\rm s} &= \frac{4}{3}(3D/r_{\rm s} - 3(D/r_{\rm s})^2 + (D/r_{\rm s})^3), \\
\kappa_T &= \left(\frac{\partial \ln \kappa}{\partial \ln T}\right)_\rho, \\
\kappa_\rho &= \left(\frac{\partial \ln \kappa}{\partial \ln \rho}\right)_T, \\
\nu &= \left(\frac{\partial \ln \epsilon_{\rm N}}{\partial \ln T}\right)_\rho \text{ and} \\
\lambda &= \left(\frac{\partial \ln \epsilon_{\rm N}}{\partial \ln \rho}\right)_T,
\end{aligned}$$

with D being the width of the shell and $r_{\rm s}$ the radius of its upper boundary. The nuclear energy generation rate is denoted by $\epsilon_{\rm N}$. For a shell to be thermally unstable both c^* and σ must be greater than zero. The quantity c^* is the gravothermal specific heat and must be positive if the deposition of heat into the shell is to raise its temperature.

As the shell is believed to be burning hydrogen via the CNO-cycle only the $^{12}{\rm C(p,\gamma)}$ reaction is considered in the nuclear energy generation rate. If this is done $\nu \approx 12$ and evaluation of σ yields a value of around 8, with $c^* > 0$. For comparison, on the TP-AGB the value of σ is below zero throughout becoming no greater than -2. Typical values for the important variables on the TP-AGB and during the H-shell instability are shown in Table 6.1.

The instability analysis seems to indicate that the model does indeed have a thermally unstable hydrogen burning shell. However, there is a worrying problem: the change in the surface abundance of the model. There is no

Parameter	During TP-AGB	During H-shell instability
σ	-2.85	8.31
κ_T	-6.95	-2.88
κ_ρ	0.24	0.0329
$\alpha_{\rm s}$	0.0236	1.16
α_P	1.12	1.48
α_T	1.55	1.52
ν	8.51	12.64

Table 6.1: Typical values of the components of σ on the TP-AGB and when the H-shell instability occurs.

convection in the model that could connect the surface with the hydrogen burning shell. So how is it that the surface abundances can be changing? The obvious answer is that there is numerical diffusion occuring in the model which is dragging material that should have remained deeper within the star to the surface (and vice versa). To test this hypothesis the viscous mesh can be applied. If the mesh is fixed from the surface to below the hydrogen burning shell (a total of less than 300 mesh points) then numerical diffusion cannot occur.

Owing to the fact that mass loss is occuring and that the mass of each mesh point is small the mesh cannot be fully locked. If this was to be done the surface mesh point would have less mass that the next-to-surface point, which is clearly undesirable. Instead the mesh can be made viscous but not fully fixed using $\psi = 0.9$. This will reduce the amount of mesh movement and hence the amount of numerical diffusion. The results of this simulation run are shown in Figure 6.6. The model makes a direct transition to the white dwarf cooling track and no periodic behaviour is detected. Increasing the spatial and temporal resolution with which the model is evolved has no effect and the cyclic phenomenon cannot be recovered. It therefore appears that the phenomenon is indeed due to the occurrence of numerical diffusion.

Only one point remains to be explained: why does the instability criterion define the shell as being unstable if the phenomenon is a numerical artifact? This question cannot be answered to the author's satisfaction. The solution may lay in the definition of the thickness of the burning shell. Yoon et al. (2004) define the edges of the burning shell as being the points at which the energy generation rate is 2×10^{-3} times the peak energy generation rate.

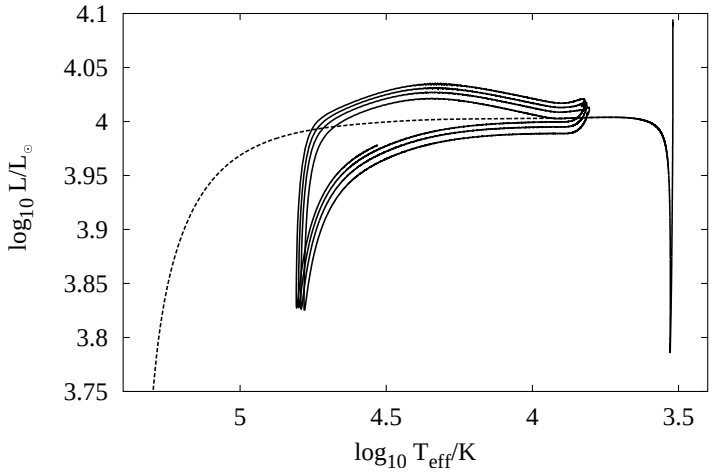

Figure 6.6: HR diagram showing the evolution of the model with the viscous mesh applied to the 300 outermost mesh points (dotted line). No periodic behaviour is detected. The solid line shows the original behaviour for comparison.

The algorithm employed in the STARS code gives a width that is consistent with the Yoon et al. (2004) definition. However, if the definition of the width of the shell is changed slightly so that the shell is thinner, the gravothermal specific heat capacity becomes negative and the model should be considered stable.

6.3 Modelling a Late Thermal Pulse

In order to produce a LTP model the object must be made to leave the TP-AGB at exactly the right point. The hydrogen-burning shell must have already created a substantial amount of helium and that helium must be about ready to ignite as the star leaves the TP-AGB. The point at which the star leaves the TP-AGB can, to some extent, be controlled by varying the parameter η in the Reimers' mass-loss formula. A late thermal pulse model was created from the same model run as above, i.e. a star initially of $1.5\,\mathrm{M}_\odot$ and metallicity $Z = 0.008$, evolved along the TP-AGB with Reimers' mass-loss with $\eta = 1$. A starting model was taken from when the helium luminosity drops below $10^4\,\mathrm{L}_\odot$ (roughly where the interpulse would begin)

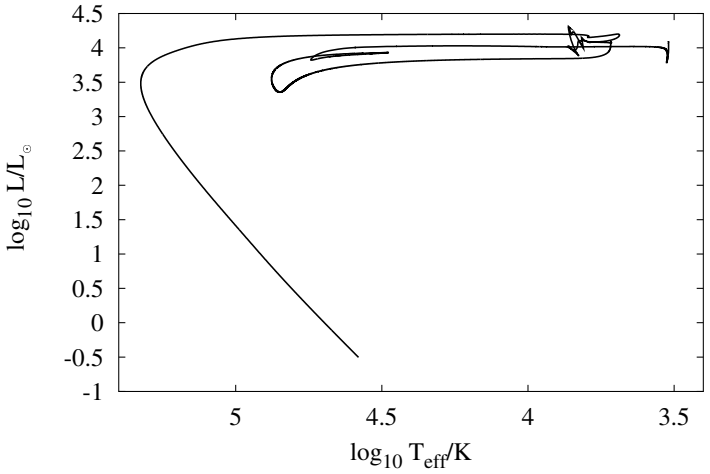

Figure 6.7: Hertzsprung-Russell diagram showing the evolution of a late thermal pulse.

after the tenth pulse. Trial-and-error variation of η was used to alter the mass loss in order to get the star to leave the TP-AGB at the desired point with $\eta = 0.4875$ being found to give the required behaviour.

The pulse reaches a peak helium luminosity of $\log L_{\mathrm{He}}/\,\mathrm{L}_{\odot} = 8.035$ similar to the values that it had reached towards the end of the TP-AGB. As the pulse reaches its peak the star makes a very rapid transition to the blue, reaching a surface temperature of around 63,000 K. The evolution across the HR-diagram is shown in Figure 6.7. The luminosity then drops before rising again as the star moves back to the red, becoming a giant again. At this point, some difficulty is encountered with the model and it is necessary to turn off the mass loss in order to guarantee convergence. This should not affect the final outcome of the model greatly as very little envelope is left by this stage.

Figure 6.8 shows the evolution of the surface CNO element abundances with model number. As the star recovers from the late thermal pulse an episode of third dredge-up occurs with the surface carbon abundance being enhanced by an order of magnitude. Oxygen is also enhanced whilst nitrogen is depleted. This episode of dredge-up mixes the remaining amount of hydrogen in the envelope over a greater range in mass and so the surface abundance of hydrogen drops from 0.691 to just 0.0493. At the same time

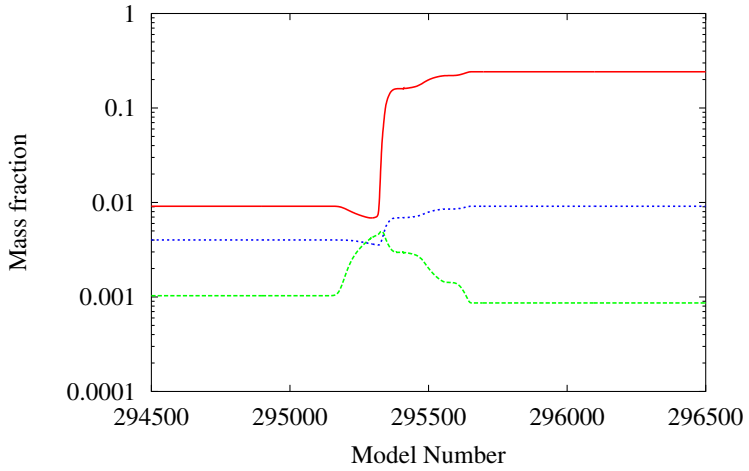

Figure 6.8: Evolution of the surface CNO element abundances with model number after the late thermal pulse. The enhancement of carbon (red) and oxygen (blue) and the depletion of nitrogen (green) are characteristic of third dredge-up. Model number is used in order to show the changes in the abundances more clearly. Note the dip in the carbon abundance as material from the H-burning shell is dredged up before that from the intershell.

the helium abundance rises from 0.291 to 0.661.

Blöcker (2001) investigated the formation of PG 1159 stars and the Wolf-Rayet central stars of planetary nebula. He found that with the inclusion of convective overshooting on the pulse-driven intershell convection zone, TDUP could occur after a late thermal pulse. Prior to this LTPs had only been considered in relation to their mass loss as possible routes to the formation of hydrogen deficient objects. Blöcker's model (of mass $0.625\,M_{\odot}$, about $0.02\,M_{\odot}$ lighter than the STARS model) produced an object with a final surface abundance by mass with the proportions (H,He,C,O)=(3,45,38,12). The model produced with the STARS code gives final surface abundances with proportions (5,66,24,<1). The work of Dreizler & Heber (1998) gives the surface abundance, in mass fraction, of non-pulsating PG 1159 stars with the proportions (He,C,O)=(65,28,7) and (40,43,16) for pulsating PG 1159 stars. While both models contain too much hydrogen, the STARS model gives reasonable agreement with the non-pulsating case (although it has far too little oxygen) while Blöcker's models gives good agreement with the pulsating case.

Once again, the STARS code has been shown to give TDUP where other

codes have not found it and have had to resort to the inclusion of extra-mixing mechanisms. The issue may be one of pulse strength as a stronger pulse tends to give more dredge-up. This was found to be the case by Herwig & Austin (2004) who varied the strength of the triple-α rate and were thereby able to obtain deeper dredge-up. Unfortunately, no information on the strength of the LTP in Blöcker's model is available and so it is not possible to make a comparison. This issue needs to be investigated further.

6.4 Summary

In this chapter a brief examination of the behaviour of stars as they leave the TP-AGB has been conducted. Numerical diffusion was shown to cause periodic behaviour as the star crossed to the white dwarf cooling track. This was suppressed using the viscous mesh. A model undergoing a late thermal pulse was also described and its surface abundances were shown to be in reasonable agreement with non-pulsating PG 1159 stars.

Chapter 7

Summary and Future Directions

登鸛雀樓

王之渙

白日依山盡,
黃河入海流;
欲窮千里目,
更上一層樓。

Climbing the Heron Pavilion

Wang Zhihuan

The white sun sets behind the mountain,
The yellow river flows to the sea;
Wishing to go as far as eyes can see,
I climb another level.

7.1 Evolution

The early attempts by Pols & Tout (2001) to make fully simultaneous calculations of TP-AGB evolution managed only a few pulses for a $5\,M_{\odot}$ model of metallicity $Z = 0.02$. This work has built substantially upon the foundations provided by these authors. With a viscous mesh technique to enhance

the numerical stability of the code, a total of 198 pulses across 8 different masses at $Z = 0.02$ were calculated, with a further 105 pulses calculated over 7 different masses at $Z = 0.008$ and another 65 over 7 different masses at $Z = 0.004$.

Unfortunately, this work has not been quite as successful as the author would have liked. First, the code requires a certain degree of baby-sitting. The early pulses of a sequence, which are usually weaker than the later ones, can usually be evolved without any difficulty. However, the stronger pulses prove more demanding and in general the code breaks down at least once a pulse. This is undesirable – ideally the code would run through the entire TP-AGB without any intervention from the user. There is still some work to be done in terms of improving the numerical stability of the code. In the intermediate-mass stars the main problem seems to be in dealing with hot-bottom burning owing to the occurrence of numerical diffusion. Hydrogen is dragged down into hotter regions by the movement of the mesh and burns violently causing difficulties with convergence. This issue needs to be resolved if the evolution of these objects is to be followed further. In the low-mass stars the main problem seems to occur near the peak of the thermal pulses but the cause is unclear.

In addition to resolving problems with numerical stability and getting the code to run continuously, the models in chapters 3 and 4 were evolved without mass loss. This is clearly not physical as we see the effects of mass loss. While there is some debate as to what the morally superior mass-loss law[1] is, it is clear that models of TP-AGB evolution should include some form of mass loss. The models presented in chapter 5 represent a first step to achieving this and highlight some of the problems that come with mass loss. It is noted that the models involving mass loss could not be evolved through as many thermal pulses as those without, suggesting that mass loss may make models more numerically unstable. This issue will need to be addressed if models that are more physically realistic are to be generated. In addition, there appears to be an issue with TDUP at low envelope masses which generally leads to the model failing to converge. It is also unclear why this is and it is very important to address this problem. TDUP is currently believed to be substantially reduced if the envelope mass is very low but if

[1]Thanks to John Lattanzio for this phrase.

TDUP does occur it will substantially affect the envelope composition.

The models presented in chapter 4 are the first fully simultaneous calculations of TP-AGB stars of metallicity other than solar. The LMC models give more efficient third dredge-up at lower core mass than previous calculations. Using these models as input for a population synthesis code it has been possible to reproduce the carbon star luminosity function of the LMC for the first time. Unfortunately, the SMC CSLF cannot be reproduced using the models from this work. The reason for this is unclear and needs to be investigated.

The comparison of models computed using different codes is an interesting one. In an attempt to understand why the STARS models are able to reproduce the LMC CSLF whereas the models of other codes cannot, a detailed comparison of models computed using the STARS and MSSSP codes was undertaken. No obvious reason for the difference was found. Further study of this problem is necessary and it would be useful to increase the number of codes involved in the study. By making detailed comparisons of many different codes it is hoped that the reasons why their models show different behaviour can be ascertained. In addition to a comparison of codes it would also be useful to investigate certain numerical effects. For example, the STARS code currently uses an arithmetic mean in order to compute the mixing coefficients required by the diffusion equation. This is not the only possible choice and the effect of other choices on particularly the amount of TDUP should be considered. Another important issue is that of numerical diffusion. In chapter 5 it was noted that numerical diffusion, owing to the motion of the adaptive mesh, caused the formation of a ^{13}C-pocket. Does numerical diffusion affect other processes on the TP-AGB? How much numerical diffusion can be expected to occur during particular phases of the TP cycle and, if it is significant, can anything be done to reduce it? These are questions that should be answered in order to increase the confidence that can be held in the models.

Chapter 6 presented the first post-AGB star models computed using the STARS code. The loop phenomenon demonstrates the need to be wary of numerical diffusion and suggests that it may be necessary to use the viscous mesh on the outermost mesh points of models going through this phase. A more thorough study of the phenomena of late and very late thermal pulses

needs to be undertaken. This should include the effects of the efficiency of mixing on the occurrence of TDUP in the case of the LTP models and on H-ingestion by the intershell convection zone in the case of the very late thermal pulse models.

This work has only examined evolution at three relatively high metallicities. With the recent increase in spectroscopic observations of low metallicity stars it would be interesting to examine the evolution of TP-AGB stars of low metallicity. Recent work in this area has been done by Herwig (2004a,b). He found some interesting behaviour not seen at higher metallicities including hot dredge-up (Herwig, 2004a). Hot dredge-up occurs when TDUP pushes into regions that are hot enough to burn protons via the CNO cycle. This results in some of the carbon that is dredged up being processed into nitrogen resulting in surface enhancements of both these elements. Low metallicity models should be made with the STARS code in order to see whether this effect is also observed. It is conceivable that in such a situation the coupling of structure, burning and mixing may be important.

The modifications to the STARS code made in this work also open up the possibility of studying the Super-AGB (S-AGB) stars. These are stars that are more massive than the intermediate mass stars and are capable of igniting carbon in their cores prior to entering the TP-AGB (Garcia-Berro & Iben, 1994). The fate of these stars is uncertain making them fruitful objects to study. One of three things could happen to an S-AGB star:

- Formation of a massive white dwarf. This would occur if the entire envelope is removed during the TP-AGB and requires that the star experience very strong mass loss and/or TDUP to inhibit the growth of the core.

- Carbon detonation. If sufficient carbon remains unburnt in the core after the initial episode of carbon burning then conditions in the core may become right for explosive carbon burning to occur. This would produce a detonation akin to a type Ia supernova.

- Core collapse. If TDUP does not occur or is shallow, or the stellar winds are weak, then the core of an S-AGB star could grow enough to reach the Chandrasekhar mass, producing a type II supernova.

These objects pose some significant computational challenges. The ignition of carbon under degenerate conditions is problematic and in addition it is necessary to follow the propagation of the carbon flame very carefully (Garcia-Berro et al., 1997).

7.2 Nucleosynthesis

In chapter 5 the details of a major overhaul of the nucleosynthesis subroutines of the STARS code have been described. These subroutines have been used to examine the nucleosynthesis of minor isotopes during the TP-AGB. The models produced were found to be consistent with constraints provided by pre-solar grains, though problems were found with reproducing the measured $^{16}O/^{17}O$ ratio. Comparison of the surface abundances of fluorine and lithium with observations was only partially successful. All the models considered produced too little fluorine to match the observations. In the case of lithium the models were unable to reproduce the most lithium-abundant stars. The reason for these deficiencies should be investigated.

Owing to the computational demands of using the nucleosynthesis subroutines it was only possible to generate a small grid of nine models. A much larger grid should be computed comprising the same masses as presented in chapters 3 and 4. This would ideally extend over a greater range in metallicity than has been considered in this work. Such a grid would be useful for population synthesis calculations and Galactic chemical evolution because the yields from TP-AGB stars could be computed. Ideally, the yields would be calculated for various different mass-loss laws to give some idea of the uncertainty associated with the ignorance of the mechanism for mass loss in AGB stars. The code is not currently at a state where such a study would be feasible. A large amount of user intervention is required to evolve through many of the pulses and the end of the TP-AGB has only been reached in a couple of cases so it is currently impossible to compute full yields from the code. In addition, the computer time required to produce such models may be prohibitively long.

The nucleosynthesis subroutines open up the possibility of studying the formation of a ^{13}C-pocket. This would involve the inclusion of extra-mixing mechanisms such as rotation, convective overshooting and internal gravity

waves. The STARS code already has convective overshooting included as an option but it is different from the formalism employed by e.g. Herwig (2000). Inclusion of the physics of internal gravity waves in either the formalism of Garcia Lopez & Spruit (1991) or that of Montalbán & Schatzman (2000) should be straight-forward as they only require information to be inserted into `funcs1`. Inclusion of rotational mixing (e.g. Zahn, 1992) would be more problematic because it requires the addition of angular momentum as a variable and therefore also an equation for its transport. However, all these mechanisms should eventually be included in the STARS code as the origin of the ^{13}C-pocket is still one of the great unsolved problems of TP-AGB evolution.

Closely related to the study of the ^{13}C pocket is the study of the *s*-process elements. These were not considered in the nucleosynthesis chapter. A wealth of information on these elements is available both from pre-solar grains and spectroscopic observations which could potentially be useful to constrain models of TP-AGB evolution. Currently there is no means in the STARS code to study the *s*-process and this deficiency should be dealt with. There are two possible approaches. First, the physical conditions in the intershell region and the details of TDUP could be recorded and used as input for a post-processing code (e.g. that of Gallino et al., 1998). Alternatively subroutines for calculating the *s*-process within the STARS code could be developed. These would take a similar form to the nucleosynthesis subroutines described in chapter 5. This is perhaps not the best approach. To study the *s*-process properly it is necessary to consider elements between nickel and lead, each element having many isotopes. The code would therefore need to be able to invert a large sparse matrix very quickly and this may prove difficult.

Bibliography

Alexander D. R., Ferguson J. W., 1994, ApJ, 437, 879

Althaus L. G., Serenelli A. M., Panei J. A., Córsico A. H., García-Berro E., Scóccola C. G., 2005, A&A, 435, 631

Amari S., Zinner E., Lewis R. S., 2000, Meteoritics and Planetary Science, 35, 997

Anders E., Grevesse N., 1989, Geo.Cosmo.Acta, 53, 197

Angulo C., et al. 1999, Nuclear Physics A, 656, 3

Arnould M., Goriely S., Jorissen A., 1999, A&A, 347, 572

Bahcall N. A., Fowler W. A., 1969, ApJ, 157, 659

Bao Z. Y., Beer H., Käppeler F., Voss F., Wisshak K., Rauscher T., 2000, Atomic Data and Nuclear Data Tables, 76, 70

Bernatowicz T., Fraundorf G., Ming T., Anders E., Wopenka B., Zinner E., Fraundorf P., 1987, Nature, 330, 728

Blöcker T., 2001, Ap.S.S., 275, 1

Blackmon J. C., Champagne A. E., Hofstee M. A., Smith M. S., Downing R. G., Lamaze G. P., 1995, Phys. Rev. Lett., 74, 2642

Blöcker T., 1995, A&A, 297, 727

Blöcker T., Schönberner D., 1997, A&A, 324, 991

Böhm-Vitense E., 1958, Zeitschrift fur Astrophysics, 46, 108

Boothroyd A. I., Sackmann I. J., 1988, ApJ, 328, 671

Boothroyd A. I., Sackmann I.-J., Wasserburg G., 1995, ApJ. Lett., 442, L21

Boothroyd A. I., Sackmann I.-J., Wasserburg G. J., 1994, ApJ.Lett., 430, L77

Bowen G. H., 1988, ApJ, 329, 299

Brehm K., Becker H. W., Rolfs C., et al. 1988, Z. Phys., 330, 167

Cameron A. G. W., Fowler W. A., 1971, ApJ, 164, 111

Caughlan G. R., Fowler W. A., 1988, Atomic Data and Nuclear Data Tables, 40, 283

Champagne A. E., Cella C. H., Kouzes R. T., Lowry M. M., Magnus P. V., Smith M. S., Mao Z. Q., 1988, Nuclear Physics A, 487, 433

Chieffi A., Straniero O., 1989, ApJS., 71, 47

Clayton D. D., 1983, Principles of Stellar Evolution and Nucleosynthesis. The University of Chigaco Press

Cook K. H., Aaronson M., 1989, AJ., 97, 923

Dababneh S., Heil M., Käppeler F., Görres J., Wiescher M., Reifarth R., Leiste H., 2003, Phys. Rev. C., 68, 025801

de Oliveira F., Coc A., Aguer P., Angulo C., Bogaert G., Kiener J., Lefebvre A., Tatischeff V., Thibaud J.-P., Fortier S., Maison J. M., Rosier L., Rotbard G., Vernotte J., Arnould M., Jorissen A., Mowlavi N., 1996, Nuclear Physics A, 597, 231

Denissenkov P. A., Tout C. A., 2003, MNRAS, 340, 722

Denker A., Drotleff H. W., Grosse M., Knee H., Kunz R., Mayer A., Seidel R., Soiné M., Wöohr A., Wolf G., Hammer J. W., 1995, in Busso M., Raiteri C. M., Gallino R., eds, AIP Conf. Proc. 327: Nuclei in the Cosmos III . p. 255ff

Dreizler S., Heber U., 1998, A&A, 334, 618

Duerbeck H. W., Benetti S., 1996, ApJ.Lett, 468, L111

Eggleton P. P., 1971, MNRAS, 151, 351

Eggleton P. P., 1972, MNRAS, 156, 361

Eggleton P. P., Faulkner J., Flannery B. P., 1973, A&A, 23, 325

El Eid M. F., Champagne A. E., 1995, ApJ, 451, 298

Forestini M., Goriely S., Jorissen A., Arnould M., 1992, A&A, 261, 157

Freytag B., Ludwig H. G., Steffen M., 1996, A&A, 313, 497

Frost C. A., Cannon R. C., Lattanzio J. C., Wood P. R., Forestini M., 1998, A&A, 332, L17

Frost C. A., Lattanzio J. C., 1996, ApJ, 473, 383

Görres J., Arlandini C., Giesen U., Heil M., Käppeler F., Leiste H., Stech E., Wiescher M., 2000, Phys. Rev. C, 62, 055801

Görres J., Graff S., Wiescher M., Azuma R. E., Barnes C. A., Becker H. W., T. R. W., 1990, Nuclear Physics A, 517, 329

Gallino R., Arlandini C., Busso M., Lugaro M., Travaglio C., Straniero O., Chieffi A., Limongi M., 1998, ApJ, 497, 388

Garcia-Berro E., Iben I., 1994, ApJ, 434, 306

Garcia-Berro E., Ritossa C., Iben I. J., 1997, ApJ, 485, 765

Garcia Lopez R. J., Spruit H. C., 1991, ApJ, 377, 268

Gledenov Y. M., Salatski V. I., Sedyshev P. V., Sedysheva M. V., Koehler P. E., Vesna V. A., Okunev I. S., 1995, in Busso M., Raiteri C. M., Gallino R., eds, AIP Conf. Proc. 327: Nuclei in the Cosmos III . p. 173ff

Goriely S., Jorissen A., Arnould M., 1989, in Proc. 5th Workshop on Nuclear Astrophysics . p. 60

Groenewegen M., 2004, ArXiv Astrophysics e-prints

Han Z., Podsiadlowski P., Eggleton P. P., 1994, MNRAS, 270, 121

Harries T. J., Hilditch R. W., Howarth I. D., 2003, MNRAS, 339, 157

Henyey L. G., Wilets L., Böhm K. H., Lelevier R., Levee R. D., 1959, ApJ, 129, 628

Herbig G. H., Boyarchuk A. A., 1968, ApJ, 153, 397

Herwig F., 2000, A&A, 360, 952

Herwig F., 2002, Ap.S.S., 279, 103

Herwig F., 2004a, ApJ, 605, 425

Herwig F., 2004b, ApJS., 155, 651

Herwig F., Austin S. M., 2004, ApJ. Lett., 613, L73

Holmes J. A., Woosley S. E., Fowler W. A., Zimmerman B. A., 1976, Atomic Data and Nuclear Data Tables, 18, 305ff

Huss G. R., Hutcheon I. D., Wasserburg G. J., Stone J., 1992, in Lunar and Planetary Science Conference Presolar (?) corundum in the Orgueil meteorite. pp 29–33

Iben I., 1975, ApJ, 196, 525

Iben I., 1976, ApJ, 208, 165

Iben I., 1981, ApJ, 246, 278

Iben I., MacDonald J., 1995, LNP, 443, 48

Iben I., Renzini A., 1982a, ApJ. Lett., 263, L23

Iben I., Renzini A., 1982b, ApJ. Lett., 259, L79

Iliadis C., Buchmann L., Endt P. M., Herndl H., Wiescher M., 1996, Phys. Rev. C, 53, 475

Iliadis C., Schange T., Rolfs C., Schröder U., Somorjai E., Trautvetter H. P., Wolke K., Endt P. M., Kikstra S. W., Champagne A. E., Arnould M., Paulus G., 1990, Nuclear Physics A, 512, 509

Itoh N., Adachi T., Nakagawa M., Munataka H., 1989, ApJ, 339, 354

Itoh N., Kohyama Y., 1983, ApJ, 275, 858

Itoh N., Mitake S., Iyetomi H., Ichimaru S., 1983, ApJ, 273, 774

Itoh N., Mutoh H., Hikita A., Kohyama Y., 1992, ApJ, 395, 622

Izzard R. G., Tout C. A., 2004, MNRAS, 350, L1

Izzard R. G., Tout C. A., Karakas A. I., Pols O. R., 2004, MNRAS, 350, 407

Jorissen A., Arnould M., 1989, A&A, 221, 161

Jorissen A., Goriely S., 2001, Nuclear Physics A, 688, 508

Jorissen A., Smith V. V., Lambert D. L., 1992, A&A, 261, 164

Kaeppeler F., Wiescher M., Giesen U., Goerres J., Baraffe I., El Eid M., Raiteri C. M., Busso M., Gallino R., Limongi M., Chieffi A., 1994, ApJ, 437, 396

Karakas A. I., Lattanzio J. C., 2003, Publications of the Astronomical Society of Australia, 20, 279

Karakas A. I., Lattanzio J. C., Pols O. R., 2002, Pub. Astron. Soc. Aust., 19, 515

Keenan P. C., Boeshaar P. C., 1980, ApJS., 43, 379

Kippenhahn R., Weigert A., 1990, Stellar Structure and Evolution. Stellar Structure and Evolution, XVI, 468 pp. 192 figs.. Springer-Verlag Berlin Heidelberg New York. Also Astronomy and Astrophysics Library

Koehler P. E., Kavanagh R. W., Vogelaar R. B., Gledenov Y. M., Popov Y. P., 1997, Phys. Rev. C, 56, 1138

Koehler P. E., O'Brien H. A., 1989, Phys. Rev. C., 39, 1655

Krane K. S., 1988, Introductory Nuclear Physics. John Wiley & Sons

Kroupa P., Tout C. A., Gilmore G., 1993, MNRAS, 262, 545

Landre V., Prantzos N., Aguer P., Bogaert G., Lefebvre A., Thibaud J. P., 1990, A&A, 240, 85

Langer N., Heger A., Wellstein S., Herwig F., 1999, A&A, 346, L37

Lattanzio J., Wood P., 2004, Asymptotic Giant Branch Stars. Springer-Verlag, pp 23–104

Lattanzio J. C., 1989, ApJ, 344, L25

Lawlor T. M., MacDonald J., 2003, ApJ, 583, 913

Lebzelter T., Hron J., 2003, A&A, 411, 533

Lewis R. S., Amari S., Anders E., 1990, Nature, 348, 293

Lewis R. S., Ming T., Wacker J. F., Anders E., Steel E., 1987, Nature, 326, 160

Lugaro M., Davis A. M., Gallino R., Pellin M. J., Straniero O., Käppeler F., 2003, ApJ, 593, 486

Lugaro M., Ugalde C., Karakas A. I., Görres J., Wiescher M., Lattanzio J. C., Cannon R. C., 2004, ApJ, 615, 934

Marigo P., Girardi L., Bressan A., 1999, A&A, 344, 123

Merrill P., 1952, Science, 115, 484

Meynet G., Arnould M., 1993, in Kaeppeler F., Wisshak K., eds, Nuclei in the Cosmos II . pp 487–492

Meynet G., Arnould M., 2000, A&A, 355, 176

Montalbán J., Schatzman E., 2000, A&A, 354, 943

Mowlavi N., 1999, A&A, 344, 617

Munataka H., Kohyama Y., Itoh N., 1987, ApJ, 316, 708

Nittler L. R., Alexander C. M. O., Gao X., Walker R. M., Zinner E., 1997, ApJ, 483, 475

Ostlie D. A., Carroll B. W., 1996, An Introduction to Modern Stellar Astrophysics. Addison Wesley

Ott U., Begemann F., 1990, ApJ. Lett., 353, L57

Paczyński B., 1977, ApJ, 214, 812

Pols O. R., Tout C. A., 2001, Mem. S. A. It., 72, 299

Pols O. R., Tout C. A., Eggleton P. P., Han Z., 1995, MNRAS, 274, 964

Rauscher T., Thielemann F., 2000, Atomic Data and Nuclear Data Tables, 75, 1

Reimers D., 1975, Circumstellar envelopes and mass loss of red giant stars. Problems in stellar atmospheres and envelopes, pp 229–256

Renda A., Fenner Y., Gibson B. K., Karakas A. I., Lattanzio J. C., Campbell S., Chieffi A., Cunha K., Smith V. V., 2004, MNRAS, 354, 575

Renzini A., 1981, in ASSL Vol. 88: Physical Processes in Red Giants Red giants as precursors of planetary nebulae. pp 431–446

Rogers F. J., Iglesias C. A., 1992, ApJS, 79, 507

Sackmann I.-J., 1980, ApJ, 235, 554

Sackmann I.-J., Boothroyd A. I., 1992, ApJ Lett., 392, L71

Sanders R. H., 1967, ApJ, 150, 971

Schatz H., Jaag S., Linker G., Steininger R., Käppeler F., Koehler P. E., Graff S. M., Wiescher M., 1995, Phys. Rev. C, 51, 379

Schmidt S., Rolfs C., Schulte W. H., Trautvetter H. P., Kavanagh R. W., Hategan C., Faber S., Valnion B. D., Graw G., 1995, Nuclear Physics A, 591, 227

Schönberner D., 1979, A&A, 79, 108

Schwarzschild M., Härm R., 1965, ApJ, 142, 855

Schwarzschild M., Härm R., 1967, ApJ, 150, 961

Smith R. L., Sackmann I.-J., Despain K. H., 1973, in Explosive Nucleosynthesis Nucleosynthesis in Red Giants. p. 168ff

Smith V. V., Plez B., Lambert D. L., Lubowich D. A., 1995, ApJ, 441, 735

Srinivasan B., Anders E., 1978, Science, 201, 51

Stegmüller F., Rolfs C., Schmidt S., Schulte W. H., Trautvetter H. P., Kavanagh R. W., 1996, Nuclear Physics A, 601, 168

Straniero O., Chieffi A., Limongi M., Busso M., Gallino R., Arlandini C., 1997, ApJ, 478, 332

Straniero O., Domínguez I., Cristallo S., Gallino R., 2003, Pub. Astron. Soc. Aust., 20, 389

Straniero O., Domínguez I., Imbriani G., Piersanti L., 2003, ApJ, 583, 878

Straniero O., Limongi M., Chieffi A., Dominguez I., Busso M., Gallino R., 2000, Mem. S. A. It., 71, 719

Sweigart A. V., 1974, ApJ, 189, 289

Thielemann F., Truran J. W., Arnould M., 1986, in Advances in Nuclear Astrophysics Thermonuclear reaction rates from statistical model calculations. pp 525–540

Timmermann R., Becker H. W., Rolfs C., Schröder U., Trautvetter H. P., 1988, Nuclear Physics A, 477, 105

Travaglio C., Randich S., Galli D., Lattanzio J., Elliott L. M., Forestini M., Ferrini F., 2001, ApJ, 559, 909

Ugalde C., 2004, PhD thesis, University of Notre Dame

Ulrich R. K., Scalo J. M., 1972, ApJ. Lett., 176, L37

Van Eck S., Jorissen A., Udry S., Mayor M., Pernier B., 1998, A&A, 329, 971

Vassiliadis E., Wood P. R., 1993, ApJ, 413, 641

Vassiliadis E., Wood P. R., 1994, ApJS., 92, 125

Ventura P., 2004, Mem.S.A.It., 75, 654

Weigert A., 1966, Zeitschrift fur Astrophysics, 64, 395

Wiescher M., Gorres J., Thielemann F., 1990, ApJ, 363, 340

Wood P. R., 1981, in Iben I., ed., Physical Processes in Red Giant Stars . p. 135

Wood P. R., Faulkner D. J., 1986, ApJ, 307, 659

Wood P. R., Zarro D. M., 1981, ApJ, 247, 247

Woosley S. E., Weaver T. A., 1995, ApJS, 101, 181

Yoon S.-C., Langer N., van der Sluys M., 2004, A&A, 425, 207

Zahn J.-P., 1992, A&A, 265, 115

Zinner E., Amari S., Lewis R. S., 1991, ApJ. Lett., 382, L47

Zinner E., Nittler L. R., Hoppe P., Gallino R., Lewis R. S., 2004, in Lunar and Planetary Institute Conference Abstracts Oxygen and Magnesium Isotopic Ratios of Presolar Spinel Grains. pp 1337–1338

Appendix A

Derivation of Gravothermal Specific Heat Capacity and Thermal Stability Criterion

A.1 The Gravothermal Specific Heat Capacity

Consider a shell source of geometrical thickness D, with lower boundary at r_0 and upper boundary at $r_\mathrm{s} = r_0 + D$. The mass of the shell is given by $\Delta M_\mathrm{s} = \int_{r_0}^{r_\mathrm{s}} 4\pi r^2 \rho \, \mathrm{d}r$ and assuming the density is constant

$$\Delta M_\mathrm{s} = \frac{4}{3}\pi(r_\mathrm{s}^3 - r_0^3)\rho. \tag{A.1}$$

As $r_\mathrm{s} = r_0 + D$ and assuming that the lower boundary of the shell remains fixed then on perturbation $\delta r_\mathrm{s} = \delta D$. If the mass in the shell remains fixed then perturbing equation A.1 yields

$$0 = [(r_0 + D)^3 - r_0^3]\delta\rho + 3(r_0 + D)^2\rho\delta D. \tag{A.2}$$

Rewriting this in terms of r_s gives

$$[r_\mathrm{s}^3 - (r_\mathrm{s} - D)^3]\delta\rho = -3r_\mathrm{s}^2\rho\delta r_\mathrm{s} \tag{A.3}$$

$$\Rightarrow \frac{\delta\rho}{\rho} = -\frac{3}{3D/r_\mathrm{s} - 3(D/r_\mathrm{s})^2 + (D/r_\mathrm{s})^3}\frac{\delta r_\mathrm{s}}{r_\mathrm{s}}, \tag{A.4}$$

which is equation 1 of Yoon et al. (2004). Assuming the shell expands/contracts homologously[1] we have $\delta P/P = -4\delta r_{\rm s}/r_{\rm s}$ which gives

$$\frac{\delta P}{P} = \alpha_{\rm s}\frac{\delta\rho}{\rho}, \tag{A.5}$$

where $\alpha_{\rm s}$ is as given in equation 1.8.

To derive the equation for the gravothermal specific heat capacity, we start from the 1st law of thermodynamics

$$\begin{aligned} {\rm d}q &= {\rm d}u + P{\rm d}v & \text{(A.6)}\\ &= \left(\frac{\partial u}{\partial T}\right)_v {\rm d}T + T\left(\frac{\partial P}{\partial T}\right)_v {\rm d}v, & \text{(A.7)}\end{aligned}$$

where we have used $\left(\frac{\partial u}{\partial v}\right)_T = T\left(\frac{\partial P}{\partial T}\right)_v - P$, which is the 1st law of thermodynamics combined with a Maxwell relation. By definition

$$\left(\frac{\partial P}{\partial T}\right)_v = \frac{P\alpha_T}{T\alpha_P}, \tag{A.8}$$

with α_P and α_T as defined by equations 1.9 and 1.10. Inserting this into equation A.7 and using ${\rm d}v = -{\rm d}\rho/\rho^2$ we obtain

$${\rm d}q = c_v{\rm d}T - \frac{P\alpha_T}{\rho\alpha_P}\frac{{\rm d}\rho}{\rho} \tag{A.9}$$

as $(\partial u/\partial T) = c_v$ by definition. Using the relation ${\rm d}\rho/\rho = \alpha_P{\rm d}P/P - \alpha_T{\rm d}T/T$ in the above we obtain

$${\rm d}q = \left(c_v + \frac{P\alpha_T^2}{\rho T\alpha_P}\right){\rm d}T - \frac{\alpha_T}{\rho}{\rm d}P. \tag{A.10}$$

The term in brackets is c_P and so we obtain

$${\rm d}q = c_P\left(1 - \frac{\alpha_T}{c_P\rho}\frac{{\rm d}P}{{\rm d}T}\right){\rm d}T. \tag{A.11}$$

But $\bigtriangledown_{\rm ad} = (\partial\ln P/\partial\ln T)_S = P\alpha_T/T\rho c_P$, and using ${\rm d}\rho/\rho = \alpha_P{\rm d}P/P -$

[1]This assumption, while it may seem plausible, is hard to justify and the author finds himself unable to do so.

$\alpha_T \mathrm{d}T/T$ and equation A.5 we obtain

$$\mathrm{d}q = c_P \left(1 - \bigtriangledown_{\mathrm{ad}} \frac{\alpha_{\mathrm{s}} \alpha_T}{\alpha_{\mathrm{s}} \alpha_P - 1}\right) \mathrm{d}T, \tag{A.12}$$

where comparison of the right-hand side with that of equation 1.6 gives the expression for c^*, the gravothermal specific heat capacity.

A.2 The Thermal Stability Criterion

To derive equations 1.15 and 1.16 in section 1.2 we start from equation 1.14, namely

$$\delta L_{r_{\mathrm{s}}} = \Delta M_{\mathrm{s}} \delta \epsilon_N - \Delta M_{\mathrm{s}} \frac{\mathrm{d}\delta q}{\mathrm{d}t}. \tag{A.13}$$

Dividing this by equation 1.13 and recalling that $L_{r_{\mathrm{s}}} \gg L_{r_0}$ and given $L_N \gg L_g$ we have

$$\frac{\delta L_{r_{\mathrm{s}}}}{L_{r_{\mathrm{s}}}} = \frac{\delta \epsilon_N}{\epsilon_N} - \frac{\Delta M_{\mathrm{s}}}{L_{r_{\mathrm{s}}}} \frac{\mathrm{d}\delta q}{\mathrm{d}t}, \tag{A.14}$$

where we have used $L_N \approx \epsilon_N \Delta M_{\mathrm{s}}$. But

$$\frac{\delta \epsilon_N}{\epsilon_N} = \left(\frac{\partial \ln \epsilon_N}{\partial \ln T}\right)_\rho \frac{\delta T}{T} + \left(\frac{\partial \ln \epsilon_N}{\partial \ln \rho}\right)_T \frac{\delta \rho}{\rho} \tag{A.15}$$

$$= \left(\nu + \frac{\lambda \alpha_T}{\alpha_{\mathrm{s}} \alpha_P - 1}\right) \frac{\delta T}{T}, \tag{A.16}$$

where we have used

$$\frac{\delta \rho}{\rho} = \frac{\alpha_T}{\alpha_{\mathrm{s}} \alpha_P - 1} \frac{\delta T}{T} \tag{A.17}$$

and the definitions $\nu = (\partial \ln \epsilon_N / \partial \ln T)_\rho$ and $\lambda = (\partial \ln \epsilon_N / \partial \ln \rho)_T$. Next we perturb the equation for the radiative transfer of heat at r_{s}, i.e.

$$\frac{\partial T}{\partial M_{r_{\mathrm{s}}}} = -\frac{3}{64\pi^2 ac} \frac{\kappa L_{r_{\mathrm{s}}}}{r_{\mathrm{s}}^4 T^3} \tag{A.18}$$

which yields

$$\frac{\delta L_{r_{\mathrm{s}}}}{L_{r_{\mathrm{s}}}} = -\frac{\delta \kappa}{\kappa} + 4\frac{\delta r_{\mathrm{s}}}{r_{\mathrm{s}}} + 3\frac{\delta T}{T} + \frac{\delta(\partial T/\partial M_{r_{\mathrm{s}}})}{(\partial T/\partial M_{r_{\mathrm{s}}})} \tag{A.19}$$

The last term is just $\delta T/T$. But

$$\frac{\delta r_{\mathrm{s}}}{r_{\mathrm{s}}} = -\frac{\alpha_s}{4} \frac{\delta \rho}{\rho}$$

$$= -\frac{\alpha_{\rm s}\alpha_T}{\alpha_{\rm s}\alpha_P - 1} \tag{A.20}$$

and

$$\begin{aligned} \frac{\delta\kappa}{\kappa} &= \left(\frac{\partial \ln\kappa}{\partial \ln T}\right)_\rho \frac{\delta T}{T} + \left(\frac{\partial \ln\kappa}{\partial \ln\rho}\right)_T \frac{\delta\rho}{\rho} \\ &= \left(\kappa_T + \frac{\kappa_\rho\alpha_T}{\alpha_{\rm s}\alpha_P - 1}\right)\frac{\delta T}{T}, \end{aligned} \tag{A.21}$$

where $\kappa_T = (\partial \ln\kappa/\partial \ln T)_\rho$ and $\kappa_\rho = (\partial \ln\kappa/\partial \ln\rho)_T$. Inserting all this into equation A.19 yields

$$\frac{\delta L_{r_{\rm s}}}{L_{r_{\rm s}}} = \left[4 - \kappa_T - \frac{\alpha_T}{\alpha_{\rm s}\alpha_P - 1}(\alpha_{\rm s} + \kappa_\rho)\right]\frac{\delta T}{T}. \tag{A.22}$$

Inserting this into equation A.14, along with equation A.16 gives

$$\frac{\Delta M_{\rm s}}{L_{r_{\rm s}}}\frac{{\rm d}\delta q}{{\rm d}t} = \left[\nu - 4 + \kappa_T + \frac{\alpha_T}{\alpha_{\rm s}\alpha_P - 1}(\lambda + \alpha_{\rm s} + \kappa_\rho)\right]\frac{\delta T}{T}. \tag{A.23}$$

Now $\delta q = c^*\delta T$ and defining $\theta = \delta T/T$ and $\tau_{\rm th} = \Delta M_{\rm s} T c_p/L_{r_{\rm s}}$ so the above equation becomes

$$\tau_{\rm th}\dot{\theta} = \sigma\theta, \tag{A.24}$$

which is equation 1.15, where

$$\sigma = \frac{\nu - 4 - \kappa_T + \frac{\alpha_T}{\alpha_{\rm s}\alpha_P - 1}(\lambda + \alpha_s + \kappa_P)}{c^*/c_P}, \tag{A.25}$$

as given in equation 1.16.

Appendix B

Details of the Solar Metallicity Models

This appendix presents a more detailed look at the models of solar metallicity.

TP	$M_{\rm H}$ ($M_\odot$)	$\tau_{\rm ip}$ (10^4 yr)	log ($L_{\rm He}^{\rm max}/L_\odot$)	$\Delta M_{\rm H}$ ($M_\odot$)	$\Delta M_{\rm DUP}$ ($M_\odot$)	λ	C/O
1	0.54015	...	5.28923	0.00355	...	...	0.316
2	0.54367	6.96	4.53870	0.00154	...	...	0.316
3	0.54519	8.82	5.88073	0.00346	...	...	0.316
4	0.54863	9.49	5.56585	0.00315	...	...	0.316
5	0.55176	11.2	6.53988	0.00555	...	...	0.316
6	0.55729	11.6	6.46257	0.00538	...	...	0.316

Table B.1: Details of the $1\,M_\odot$ model. The data are TP – the thermal pulse number, $M_{\rm H}$ – the hydrogen free core mass, $\tau_{\rm ip}$ – the interpulse period, $L_{\rm He}^{\rm max}$ – the peak luminosity from helium burning, $\Delta M_{\rm H}$ – the hydrogen free core mass growth during the interpulse, $\Delta M_{\rm DUP}$ – the mass of material dredged up, λ – the dredge-up efficiency parameter and C/O – the surface carbon-to-oxygen ratio by number.

TP	M_H ($M_\odot$)	τ_{ip} (10^4 yr)	log ($L_{He}^{max}/L_\odot$)	ΔM_H ($M_\odot$)	ΔM_{DUP} ($M_\odot$)	λ	C/O
1	0.55666	...	4.48155	0.00278	...	...	0.315
2	0.55943	4.82	4.85986	0.00159	...	...	0.315
3	0.56101	6.26	5.41023	0.00241	...	...	0.315
4	0.56340	8.09	5.99830	0.00375	...	...	0.315
5	0.56713	9.15	6.31095	0.00468	...	...	0.315
6	0.57180	9.56	6.62407	0.00556	...	...	0.315
7	0.57734	9.48	6.79679	0.00604	...	...	0.315
8	0.58335	9.15	6.93533	0.00641	...	...	0.315
9	0.58960	8.78	7.05152	0.00675	0.00073	0.108	0.337
10	0.59562	8.44	7.20161	0.00720	0.00159	0.221	0.402
11	0.60123	8.18	7.38089	0.00771	0.00262	0.340	0.518
12	0.60632	7.96	7.54158	0.00824	0.00352	0.427	0.672
13	0.61104	7.73	7.67271	0.00869	0.00352	0.427	0.844

Table B.2: Details of the $1.5\,M_\odot$ model. The columns are the same as in Table B.1.

TP	M_H ($M_\odot$)	τ_{ip} (10^4 yr)	log ($L_{He}^{max}/L_\odot$)	ΔM_H ($M_\odot$)	ΔM_{DUP} ($M_\odot$)	λ	C/O
1	0.56786	...	5.77015	0.00326	...	...	0.318
2	0.57110	9.20	6.56244	0.00496	...	...	0.318
3	0.57605	9.91	6.76071	0.00574	...	...	0.318
4	0.58174	9.53	6.93065	0.00628	0.00065	0.104	0.326
5	0.58737	9.10	7.08565	0.00684	0.00166	0.243	0.367
6	0.59255	8.83	7.26906	0.00755	0.00289	0.383	0.447
7	0.59721	8.68	7.46319	0.00830	0.00412	0.496	0.563
8	0.60139	8.58	7.64903	0.00904	0.00531	0.587	0.708
9	0.60512	8.49	7.81940	0.00973	0.00637	0.655	0.874
10	0.60848	8.37	7.97563	0.01033	0.00726	0.703	1.056
11	0.61155	8.22	8.11090	0.01081	0.00796	0.736	1.245
12	0.61440	8.03	8.21348	0.01117	0.00846	0.757	1.437
13	0.61711	7.80	8.30040	0.01141	0.00883	0.774	1.631
14	0.61969	7.55	8.36701	0.01157	0.00908	0.785	1.824
15	0.62218	7.29	8.41515	0.01163	0.00920	0.791	2.015
16	0.62461	7.01	8.44952	0.01160	0.00920	0.791	2.200

Table B.3: Details of the $2\,M_\odot$ model. The columns are the same as in Table B.1.

TP	$M_{\rm H}$ ($M_\odot$)	$\tau_{\rm ip}$ (10^4 yr)	log ($L_{\rm He}^{\rm max}/L_\odot$)	$\Delta M_{\rm H}$ ($M_\odot$)	$\Delta M_{\rm DUP}$ ($M_\odot$)	λ	C/O
1	0.56351	...	4.35813	0.00267	...	...	0.318
2	0.56618	4.29	4.82547	0.00150	...	...	0.318
3	0.56767	5.80	5.41396	0.00234	...	...	0.318
4	0.56999	7.77	6.09662	0.00384	...	...	0.318
5	0.57381	8.87	6.42628	0.00482	...	...	0.318
6	0.57862	9.17	6.70970	0.00567	...	...	0.318
7	0.58421	9.02	6.88355	0.00617	0.00095	0.154	0.329
8	0.58943	8.80	7.09839	0.00695	0.00243	0.350	0.369
9	0.59395	8.78	7.33534	0.00793	0.00408	0.514	0.439
10	0.59780	8.89	7.59374	0.00900	0.00586	0.651	0.538
11	0.60094	9.07	7.49979	0.0101	0.00751	0.741	0.658
12	0.60357	9.24	7.62277	0.0112	0.00897	0.801	0.793
13	0.60580	9.34	7.58352	0.0122	0.0102	0.837	0.936
14	0.60778	9.37	7.92539	0.0129	0.0111	0.863	1.084
15	0.60955	9.33	8.02578	0.0135	0.0119	0.884	1.237
16	0.61112	9.25	8.64986	0.0140	0.0125	0.893	1.392
17	0.61261	8.97	8.69738	0.0140	0.0126	0.896	1.544
18	0.61408	8.72	8.73807	0.0141	0.0127	0.900	1.694
19	0.61549	8.49	8.77433	0.0141	0.0128	0.901	1.841
20	0.61688	8.25	8.79855	0.0141	0.0128	0.901	1.986

Table B.4: Details of the $3\,M_\odot$ model. The columns are the same as in Table B.1.

TP	M_H ($M_\odot$)	τ_{ip} (10^4 yr)	log ($L_{He}^{max}/L_\odot$)	ΔM_H ($M_\odot$)	ΔM_{DUP} ($M_\odot$)	λ	C/O
1	0.75332	...	4.75474	0.00200	...	...	0.319
2	0.75532	1.12	5.73430	0.00167	...	...	0.319
3	0.75698	1.41	6.31530	0.00222	0.00102	0.459	0.325
4	0.75818	1.60	6.85351	0.00301	0.00247	0.821	0.350
5	0.75872	1.84	7.35368	0.00398	0.00383	0.962	0.395
6	0.75887	2.10	7.82506	0.00499	0.00509	1.020	0.455
7	0.75877	2.35	8.24029	0.00596	0.00612	1.027	0.525
8	0.75861	2.56	8.59679	0.00683	0.00706	1.034	0.604
9	0.75838	2.75	8.89998	0.00762	0.00788	1.034	0.689
10	0.75812	2.89	9.13510	0.00827	0.00853	1.031	0.779
11	0.75786	3.00	9.33649	0.00886	0.00907	1.024	0.870
12	0.75765	3.04	9.46512	0.00922	0.00939	1.018	0.960
13	0.75748	3.03	9.53362	0.00939	0.00941	1.002	1.038
14	0.75746	2.97	9.56552	0.00940	0.00938	0.998	1.105
15	0.75748	2.91	9.57415	0.00934	0.00924	0.989	1.156
16	0.75758	2.84	9.57873	0.00920	0.00909	0.988	1.193
17	0.75769	2.78	9.58078	0.00909	0.00897	0.987	1.217
18	0.75781	2.73	9.58034	0.00900	0.00886	0.984	1.229
19	0.75795	2.69	9.57146	0.00892	0.00875	0.981	1.228
20	0.75812	2.63	9.56450	0.00882	0.00864	0.980	1.218
21	0.75830	2.59	9.55836	0.00874	0.00856	0.979	1.199

Table B.5: Details of the $4\,M_\odot$ model. The columns are the same as in Table B.1.

TP	$M_{\rm H}$ ($M_\odot$)	$\tau_{\rm ip}$ (10^4 yr)	log ($L_{\rm He}^{\rm max}/L_\odot$)	$\Delta M_{\rm H}$ ($M_\odot$)	$\Delta M_{\rm DUP}$ ($M_\odot$)	λ	C/O
1	0.83723	...	5.58461	0.00122	0.00010	0.082	0.321
2	0.83835	0.60	6.31654	0.00151	0.00107	0.709	0.326
3	0.83879	0.68	6.62647	0.00206	0.00188	0.913	0.340
4	0.83897	0.78	7.33847	0.00263	0.00260	0.989	0.348
5	0.83900	0.88	7.77935	0.00318	0.00329	1.035	0.328
6	0.83889	1.00	8.18597	0.00374	0.00392	1.048	0.277
7	0.83871	1.12	8.54076	0.00430	0.00450	1.047	0.207
8	0.83851	1.23	8.81693	0.00478	0.00493	1.031	0.139
9	0.83836	1.30	8.75116	0.00513	0.00521	1.016	0.092
10	0.83828	1.33	9.12846	0.00534	0.00532	0.996	0.069
11	0.83830	1.34	9.20431	0.00541	0.00536	0.991	0.062
12	0.83835	1.34	9.25091	0.00544	0.00534	0.982	0.062
13	0.83845	1.33	9.28176	0.00542	0.00531	0.980	0.063
14	0.83856	1.32	9.30913	0.00540	0.00528	0.978	0.065
15	0.83868	1.31	9.32451	0.00537	0.00524	0.976	0.068
16	0.83881	1.29	9.33374	0.00534	0.00521	0.976	0.070
17	0.83894	1.28	9.34200	0.00531	0.00516	0.972	0.073
18	0.83909	1.27	9.34833	0.00527	0.00514	0.975	0.075
19	0.83922	1.26	9.35482	0.00526	0.00511	0.971	0.078
20	0.83937	1.25	9.35649	0.00523	0.00509	0.973	0.081
21	0.83951	1.23	9.35407	0.00520	0.00505	0.971	0.084
22	0.83966	1.22	9.34385	0.00515	0.00501	0.973	0.086
23	0.83980	1.21	9.34588	0.00514	0.00498	0.969	0.089
24	0.83996	1.20	9.34909	0.00511	0.00498	0.975	0.092
25	0.84009	1.20	9.35486	0.00512	0.00497	0.971	0.095
26	0.84024	1.19	9.35479	0.00510	0.00495	0.971	0.097
27	0.84039	1.18	9.35090	0.00507	0.00491	0.968	0.100
28	0.84055	1.17	9.34841	0.00505	0.00489	0.968	0.103
29	0.84071	1.17	9.34439	0.00502	0.00486	0.968	0.106
30	0.84087	1.16	9.34249	0.00500	0.00484	0.968	0.109

Table B.6: Details of the first 30 pulses of the $5\,M_\odot$ model. The columns are the same as in Table B.1.

TP	M_H ($M_\odot$)	τ_{ip} (10^4 yr)	log ($L_{He}^{max}/L_\odot$)	ΔM_H ($M_\odot$)	ΔM_{DUP} ($M_\odot$)	λ	C/O
31	0.84103	1.15	9.34112	0.00498	0.00483	0.970	0.111
32	0.84118	1.14	9.33743	0.00497	0.00480	0.966	0.114
33	0.84135	1.14	9.33489	0.00495	0.00479	0.968	0.117
34	0.84151	1.13	9.33128	0.00493	0.00477	0.968	0.120
35	0.84167	1.12	9.32951	0.00492	0.00476	0.967	0.123
36	0.84183	1.11	9.32641	0.00490	0.00474	0.967	0.126
37	0.84199	1.11	9.32387	0.00489	0.00472	0.965	0.128
38	0.84216	1.10	9.32071	0.00487	0.00471	0.967	0.131
39	0.84232	1.09	9.31891	0.00486	0.00469	0.965	0.134
40	0.84249	1.09	9.31441	0.00484	0.00469	0.969	0.137
41	0.84264	1.08	9.31442	0.00484	0.00467	0.965	0.140
42	0.84281	1.08	9.31069	0.00482	0.00465	0.965	0.142
43	0.84298	1.07	9.30811	0.00480	0.00464	0.967	0.145
44	0.84314	1.06	9.30308	0.00479	0.00462	0.965	0.148
45	0.84331	1.06	9.29623	0.00477	0.00460	0.964	0.151
46	0.84348	1.05	9.29482	0.00475	0.00459	0.966	0.154
47	0.84364	1.05	9.29455	0.00475	0.00458	0.964	0.156
48	0.84381	1.04	9.28618	0.00474	0.00456	0.962	0.159
49	0.84399	1.03	9.28338	0.00471	0.00455	0.966	0.162
50	0.84415	1.03	9.27808	0.00471	0.00452	0.960	0.165
51	0.84434	1.02	9.26995	0.00468	0.00451	0.964	0.168
52	0.84451	1.02	9.26802	0.00467	0.00449	0.961	0.170
53	0.84469	1.01	9.26136	0.00466	0.00447	0.959	0.173
54	0.84488	1.00	9.25669	0.00463	0.00446	0.963	0.176
55	0.84505	1.00	9.25424	0.00463	0.00445	0.961	0.179
56	0.84523	0.99	9.25090	0.00463	0.00445	0.961	0.181
57	0.84541	0.99	9.24914	0.00462	0.00443	0.959	0.184
58	0.84560	0.98	9.24521	0.00460	0.00442	0.961	0.187
59	0.84578	0.98	9.24026	0.00459	0.00440	0.959	0.190
60	0.84597	0.97	9.23823	0.00458	0.00440	0.961	0.192

Table B.7: Details of the second 30 pulses of the $5\,M_\odot$ model. The columns are the same as in Table B.1.

TP	$M_{\rm H}$ ($M_\odot$)	$\tau_{\rm ip}$ (10^4 yr)	log ($L_{\rm He}^{\rm max}/L_\odot$)	$\Delta M_{\rm H}$ ($M_\odot$)	$\Delta M_{\rm DUP}$ ($M_\odot$)	λ	C/O
1	0.89346	...	4.14817	0.00167	...	...	0.320
2	0.89513	0.24	4.95582	0.00070	...	...	0.320
3	0.89583	0.28	5.33637	0.00082	...	...	0.319
4	0.89665	0.31	5.53298	0.00093	0.00030	0.323	0.311
5	0.89728	0.33	6.10408	0.00114	0.00071	0.623	0.291
6	0.89771	0.37	6.56976	0.00141	0.00118	0.837	0.254
7	0.89794	0.42	7.01432	0.00170	0.00164	0.965	0.202
8	0.89800	0.48	7.45015	0.00205	0.00210	1.024	0.142
9	0.89795	0.55	7.86994	0.00245	0.00252	1.029	0.091
10	0.89788	0.63	8.23066	0.00281	0.00291	1.036	0.063
11	0.89778	0.69	8.51270	0.00315	0.00318	1.010	0.054
12	0.89775	0.73	8.70330	0.00337	0.00333	0.988	0.052
13	0.89779	0.76	8.84406	0.00351	0.00342	0.974	0.052
14	0.89788	0.79	8.95947	0.00360	0.00355	0.986	0.055
15	0.89793	0.74	9.01585	0.00361	0.00347	0.961	0.057
16	0.89807	0.74	9.05273	0.00356	0.00346	0.972	0.059
17	0.89817	0.75	9.09009	0.00357	0.00345	0.966	0.062
18	0.89829	0.74	9.11072	0.00354	0.00343	0.969	0.064
19	0.89840	0.74	9.13517	0.00354	0.00342	0.966	0.067
20	0.89852	0.73	9.15073	0.00351	0.00341	0.972	0.069

Table B.8: Details of the first 20 pulses of the 6 $M_\odot$ model. The columns are the same as in Table B.1.

TP	M_H ($M_\odot$)	τ_{ip} (10^4 yr)	log ($L_{He}^{max}/L_\odot$)	ΔM_H ($M_\odot$)	ΔM_{DUP} ($M_\odot$)	λ	C/O
21	0.89862	0.73	9.05670	0.00351	0.00339	0.966	0.071
22	0.89874	0.72	9.16440	0.00348	0.00337	0.968	0.074
23	0.89885	0.71	9.17105	0.00346	0.00336	0.971	0.076
24	0.89895	0.72	9.17874	0.00347	0.00335	0.965	0.078
25	0.89907	0.71	9.18051	0.00345	0.00339	0.983	0.081
26	0.89913	0.72	9.20458	0.00349	0.00340	0.974	0.083
27	0.89922	0.72	9.21410	0.00350	0.00340	0.971	0.086
28	0.89932	0.72	9.21844	0.00349	0.00339	0.971	0.088
29	0.89942	0.72	9.12852	0.00348	0.00338	0.971	0.090
30	0.89952	0.71	9.22097	0.00347	0.00338	0.974	0.093
31	0.89961	0.71	9.22994	0.00347	0.00337	0.971	0.095
32	0.89971	0.71	9.22432	0.00346	0.00336	0.971	0.098
33	0.89981	0.70	9.22443	0.00344	0.00334	0.971	0.100
34	0.89991	0.70	9.22248	0.00343	0.00333	0.971	0.103
35	0.90001	0.70	9.22253	0.00343	0.00333	0.971	0.105
36	0.90011	0.69	9.12995	0.00342	0.00332	0.971	0.108
37	0.90021	0.69	9.22142	0.00341	0.00331	0.971	0.110
38	0.90031	0.69	9.22200	0.00340	0.00330	0.971	0.113
39	0.90041	0.68	9.21998	0.00340	0.00329	0.968	0.115
40	0.90052	0.68	9.21815	0.00338	0.00330	0.976	0.118

Table B.9: Details of the second 20 pulses of the 6 $M_\odot$ model. The columns are the same as in Table B.1.

TP	$M_{\rm H}$ ($M_\odot$)	$\tau_{\rm ip}$ (10^4 yr)	log ($L_{\rm He}^{\rm max}/L_\odot$)	$\Delta M_{\rm H}$ ($M_\odot$)	$\Delta M_{\rm DUP}$ ($M_\odot$)	λ	C/O
1	0.99440	...	4.16770	0.00030	...	...	0.287
2	0.99470	0.10	4.71606	0.00045	...	...	0.260
3	0.99513	0.12	5.04937	0.00048	0.00018	0.375	0.229
4	0.99543	0.12	5.26627	0.00056	0.00039	0.696	0.194
5	0.99560	0.14	5.44382	0.00069	0.00060	0.870	0.157
6	0.99569	0.17	6.72365	0.00086	0.00079	0.919	0.123
7	0.99576	0.19	7.01860	0.00102	0.00094	0.922	0.095
8	0.99584	0.22	7.42977	0.00118	0.00113	0.958	0.076
9	0.99589	0.25	7.74868	0.00135	0.00130	0.963	0.064
10	0.99594	0.27	8.02857	0.00151	0.00141	0.934	0.059
11	0.99604	0.29	8.26324	0.00159	0.00155	0.975	0.058
12	0.99608	0.30	8.49702	0.00170	0.00172	1.012	0.058
13	0.99606	0.33	8.69651	0.00184	0.00175	0.951	0.059
14	0.99615	0.32	8.77714	0.00182	0.00183	1.005	0.061
15	0.99614	0.33	8.86045	0.00186	0.00185	0.995	0.063
16	0.99615	0.33	8.90296	0.00187	0.00182	0.973	0.065
17	0.99620	0.32	8.91540	0.00184	0.00185	1.005	0.067
18	0.99619	0.32	8.94352	0.00186	0.00186	1.000	0.069
19	0.99619	0.32	8.95981	0.00186	0.00185	0.995	0.071
20	0.99620	0.32	8.96395	0.00184	0.00183	0.995	0.073
21	0.99621	0.32	8.97152	0.00183	0.00183	1.000	0.074
22	0.99621	0.32	8.97534	0.00183	0.00174	0.951	0.076

Table B.10: Details of the $7\,M_\odot$ model. The columns are the same as in Table B.1.

Appendix C

Details of the LMC Metallicity Models

This appendix presents a more detailed look at the models of metallicity $Z = 0.008$.

TP	$M_{\rm H}$ ($M_\odot$)	$\tau_{\rm ip}$ (10^4 yr)	log ($L_{\rm He}^{\rm max}/L_\odot$)	$\Delta M_{\rm H}$ ($M_\odot$)	$\Delta M_{\rm DUP}$ ($M_\odot$)	λ	C/O
1	0.54803	...	5.78714	0.00412	...	...	0.377
2	0.55213	8.57	4.85558	0.00171	...	...	0.377
3	0.55382	12.66	6.81462	0.00588	...	...	0.376
4	0.55968	14.53	6.77974	0.00595	...	...	0.376
5	0.56561	13.72	7.04511	0.00704	...	...	0.376
6	0.57262	13.09	7.19552	0.00749	...	...	0.387
7	0.57981	12.38	7.32393	0.00801	0.00135	0.169	0.669
8	0.58647	11.63	7.49694	0.00868	0.00241	0.278	1.199

Table C.1: Details of the $1\,M_\odot$ model. The data are TP – the thermal pulse number, $M_{\rm H}$ – the hydrogen free core mass, $\tau_{\rm ip}$ – the interpulse period, $L_{\rm He}^{\rm max}$ – the peak luminosity from helium burning, $\Delta M_{\rm H}$ – the hydrogen free core mass growth during the interpulse, $\Delta M_{\rm DUP}$ – the mass of material dredged up, λ – the dredge-up efficiency parameter and C/O – the surface carbon-to-oxygen ratio by number.

TP	M_H ($M_\odot$)	τ_{ip} (10^4 yr)	log ($L_{He}^{max}/L_\odot$)	ΔM_H ($M_\odot$)	ΔM_{DUP} ($M_\odot$)	λ	C/O
1	0.56610	...	4.83119	0.00519	...	...	0.324
2	0.57129	13.52	6.95453	0.00615	...	...	0.324
3	0.57735	12.74	7.17958	0.00700	0.00147	0.210	0.438
4	0.58288	12.05	7.37811	0.00803	0.00306	0.381	0.740
5	0.58785	11.56	7.59024	0.00905	0.00465	0.514	1.213
6	0.59225	11.16	7.77483	0.00999	0.00588	0.589	1.763
7	0.59636	10.76	7.95930	0.01072	0.00704	0.657	2.354
8	0.60004	10.35	8.09785	0.01133	0.00779	0.688	2.928
9	0.60358	9.95	8.21257	0.01180	0.00869	0.736	3.497
10	0.60669	9.51	8.29678	0.01212	0.00904	0.746	4.017
11	0.60977	9.01	8.35664	0.01221	0.00917	0.751	4.488
12	0.61281	8.50	8.39208	0.01215	0.00914	0.752	4.913
13	0.61582	7.99	8.41192	0.01199	0.00898	0.749	5.296
14	0.61883	7.50	8.41773	0.01176	0.00874	0.743	5.641
15	0.62185	7.04	8.41151	0.01148	0.00841	0.733	5.953
16	0.62492	6.60	8.40012	0.01117	0.00809	0.724	6.235
17	0.62800	6.19	8.38109	0.01084	0.00771	0.711	6.491
18	0.63113	5.81	8.35469	0.01050	0.00732	0.697	6.724
19	0.63431	5.45	8.32794	0.01015	0.00693	0.683	6.936
20	0.63753	5.13	8.29946	0.00982	0.00656	0.668	7.130

Table C.2: Details of the first 20 pulses of the 1.5 $M_\odot$ model. The columns are the same as in Table C.1.

TP	$M_{\rm H}$ ($M_\odot$)	$\tau_{\rm ip}$ (10^4 yr)	log ($L_{\rm He}^{\rm max}/L_\odot$)	$\Delta M_{\rm H}$ ($M_\odot$)	$\Delta M_{\rm DUP}$ ($M_\odot$)	λ	C/O
21	0.64079	4.83	8.27223	0.00949	0.00622	0.655	7.308
22	0.64406	4.56	8.17745	0.00919	0.00587	0.639	7.472
23	0.64738	4.31	8.16317	0.00889	0.00556	0.625	7.623
24	0.65071	4.08	8.10760	0.00861	0.00526	0.611	7.764
25	0.65406	3.80	8.09660	0.00818	0.00476	0.582	7.889
26	0.65748	3.63	8.09675	0.00798	0.00455	0.570	8.008
27	0.66091	3.46	8.09665	0.00778	0.00435	0.559	8.120
28	0.66434	3.30	8.09409	0.00758	0.00414	0.546	8.225
29	0.66778	3.15	8.09207	0.00737	0.00395	0.536	8.324
30	0.67120	3.01	8.08798	0.00719	0.00377	0.524	8.418
31	0.67462	2.88	8.08220	0.00700	0.00357	0.510	8.506
32	0.67805	2.75	8.08098	0.00681	0.00340	0.499	8.590
33	0.68146	2.64	8.07953	0.00665	0.00324	0.487	8.669
34	0.68487	2.53	8.07628	0.00649	0.00310	0.478	8.744
35	0.68826	2.43	8.08056	0.00633	0.00294	0.464	8.816
36	0.69165	2.33	8.07977	0.00618	0.00282	0.456	8.884
37	0.69501	2.24	8.08000	0.00605	0.00269	0.445	8.950
38	0.69837	2.15	8.08108	0.00590	0.00257	0.436	9.012
39	0.70170	2.07	8.08528	0.00578	0.00247	0.427	9.071
40	0.70501	2.00	8.08831	0.00566	0.00236	0.417	9.129

Table C.3: Details of the second 20 pulses of the 1.5 $M_\odot$ model. The columns are the same as in Table C.1.

TP	M_H ($M_\odot$)	τ_{ip} (10^4 yr)	log ($L_{He}^{max}/L_\odot$)	ΔM_H ($M_\odot$)	ΔM_{DUP} ($M_\odot$)	λ	C/O
1	0.56419	...	6.84938	0.01451	...	...	0.303
2	0.57866	12.78	7.08613	0.00644	0.00133	0.207	0.355
3	0.58377	11.98	7.33522	0.00764	0.00342	0.448	0.562
4	0.58799	11.66	7.58411	0.00899	0.00540	0.601	0.920
5	0.59158	11.55	7.50271	0.01030	0.00725	0.704	1.385
6	0.59463	11.48	7.42487	0.01151	0.00886	0.770	1.901
7	0.59728	11.36	7.38281	0.01251	0.01015	0.811	2.427
8	0.59964	11.16	8.40036	0.01328	0.01116	0.840	2.945
9	0.60176	10.87	8.50780	0.01383	0.01173	0.848	3.433
10	0.60386	10.48	8.58935	0.01409	0.01207	0.857	3.894
11	0.60588	10.09	8.64703	0.01427	0.01225	0.858	4.327
12	0.60790	9.65	8.69038	0.01427	0.01233	0.864	4.738
13	0.60984	9.23	8.71014	0.01421	0.01251	0.880	5.120
14	0.61154	8.82	8.72091	0.01410	0.01235	0.876	5.465

Table C.4: Details of the $2\,M_\odot$ model. The columns are the same as in Table C.1.

TP	M_H ($M_\odot$)	τ_{ip} (10^4 yr)	log ($L_{He}^{max}/L_\odot$)	ΔM_H ($M_\odot$)	ΔM_{DUP} ($M_\odot$)	λ	C/O
1	0.63039	...	6.49293	0.01110	...	...	0.302
2	0.64135	5.93	7.08140	0.00500	0.00288	0.576	0.387
3	0.64347	6.32	7.51294	0.00676	0.00555	0.821	0.605
4	0.64468	6.91	7.48296	0.00864	0.00809	0.936	0.937
5	0.64523	7.53	7.53573	0.01052	0.01027	0.976	1.332
6	0.64548	8.04	8.63257	0.01218	0.01208	0.992	1.751
7	0.64558	8.43	8.88031	0.01358	0.01208	0.992	2.168

Table C.5: Details of the $3\,M_\odot$ model. The columns are the same as in Table C.1.

TP	M_H ($M_\odot$)	τ_{ip} (10^4 yr)	log ($L_{He}^{max}/L_\odot$)	ΔM_H ($M_\odot$)	ΔM_{DUP} ($M_\odot$)	λ	C/O
1	0.81403	...	4.95989	0.00273	...	...	0.306
2	0.81676	0.75	5.86113	0.00135	0.00050	0.370	0.310
3	0.81761	0.91	6.49452	0.00187	0.00167	0.893	0.349
4	0.81781	1.09	7.09311	0.00263	0.00276	1.049	0.433
5	0.81768	1.27	7.63451	0.00342	0.00375	1.096	0.555
6	0.81735	1.45	8.12812	0.00422	0.00464	1.100	0.699
7	0.81693	1.62	8.56014	0.00502	0.00546	1.088	0.780
8	0.81649	1.78	8.90906	0.00575	0.00611	1.063	0.706
9	0.81613	1.90	9.15581	0.00633	0.00652	1.030	0.538

Table C.6: Details of the $4\,M_\odot$ model. The columns are the same as in Table C.1.

TP	M_H ($M_\odot$)	τ_{ip} (10^4 yr)	log ($L_{He}^{max}/L_\odot$)	ΔM_H ($M_\odot$)	ΔM_{DUP} ($M_\odot$)	λ	C/O
1	0.87293	...	4.14393	0.00000	...	...	0.313
2	0.87293	2.08	5.15585	0.00309	...	...	0.313
3	0.87602	0.41	5.67881	0.00098	0.00033	0.337	0.314
4	0.87667	0.46	6.22055	0.00127	0.00100	0.787	0.328
5	0.87694	0.51	6.73890	0.00168	0.00164	0.976	0.322
6	0.87698	0.58	7.22688	0.00209	0.00221	1.057	0.252
7	0.87686	0.68	7.70803	0.00258	0.00280	1.085	0.143
8	0.87664	0.79	8.15053	0.00312	0.00334	1.071	0.077
9	0.87642	0.89	8.51251	0.00358	0.00376	1.050	0.063
10	0.87624	0.97	8.77354	0.00394	0.00405	1.028	0.065
11	0.87613	1.02	8.94464	0.00419	0.00417	0.995	0.070
12	0.87615	1.04	9.07818	0.00431	0.00430	0.998	0.076
13	0.87616	1.05	9.17313	0.00439	0.00433	0.986	0.083
14	0.87622	1.05	9.23337	0.00439	0.00433	0.986	0.091
15	0.87628	1.02	9.26370	0.00437	0.00433	0.991	0.098
16	0.87632	1.03	9.29625	0.00438	0.00429	0.979	0.106
17	0.87641	1.00	9.31505	0.00432	0.00428	0.991	0.113

Table C.7: Details of the $5\,M_\odot$ model. The columns are the same as in Table C.1.

TP	$M_{\rm H}$ ($M_\odot$)	$\tau_{\rm ip}$ (10^4 yr)	log ($L_{\rm He}^{\rm max}/L_\odot$)	$\Delta M_{\rm H}$ ($M_\odot$)	$\Delta M_{\rm DUP}$ ($M_\odot$)	λ	C/O
1	0.95462	...	4.70162	0.00181	...	...	0.296
2	0.95643	0.16	5.11913	0.00053	...	...	0.263
3	0.95696	0.17	5.45018	0.00060	0.00016	0.267	0.211
4	0.95740	0.19	5.86281	0.00071	0.00049	0.690	0.148
5	0.95762	0.21	6.33273	0.00088	0.00081	0.920	0.094
6	0.95769	0.25	6.81847	0.00112	0.00123	1.098	0.064
7	0.95758	0.33	7.35535	0.00151	0.00149	0.987	0.059
8	0.95760	0.34	7.62715	0.00167	0.00168	1.006	0.059
9	0.95759	0.39	7.98463	0.00191	0.00187	0.979	0.062
10	0.95763	0.42	8.26238	0.00207	0.00203	0.981	0.066

Table C.8: Details of the $6\,M_\odot$ model. The columns are the same as in Table C.1.

Appendix D

Details of the SMC Metallicity Models

This appendix presents a more detailed look at the models of metallicity $Z = 0.004$.

TP	$M_{\rm H}$ ($\rm M_\odot$)	$\tau_{\rm ip}$ (10^4 yr)	log ($\rm L_{He}^{max}/L_\odot$)	$\Delta M_{\rm H}$ ($\rm M_\odot$)	$\Delta M_{\rm DUP}$ ($\rm M_\odot$)	λ	C/O
1	0.56326	...	6.23517	0.00399	...	...	0.367
2	0.56723	14.59	6.97912	0.00624	...	...	0.367
3	0.57345	14.62	7.18632	0.00709	...	...	0.367
4	0.58048	13.68	7.35656	0.00780	0.00099	0.127	0.693

Table D.1: Details of the $1\,\rm M_\odot$ model. The data are TP – the thermal pulse number, $M_{\rm H}$ – the hydrogen free core mass, $\tau_{\rm ip}$ – the interpulse period, $\rm L_{He}^{max}$ – the peak luminosity from helium burning, $\Delta M_{\rm H}$ – the hydrogen free core mass growth during the interpulse, $\Delta M_{\rm DUP}$ – the mass of material dredged up, λ– the dredge-up efficiency parameter and C/O – the surface carbon-to-oxygen ratio by number.

TP	M_H ($M_\odot$)	τ_{ip} (10^4 yr)	log ($L_{He}^{max}/L_\odot$)	ΔM_H ($M_\odot$)	ΔM_{DUP} ($M_\odot$)	λ	C/O
1	0.57680	...	4.35102	0.00335	...	...	0.313
2	0.58014	6.71	5.94993	0.00294	...	...	0.313
3	0.58306	11.24	6.85897	0.00546	...	...	0.313
4	0.58849	11.92	7.13006	0.00646	0.00127	0.197	0.498
5	0.59368	11.51	7.40005	0.00773	0.00330	0.427	1.141
6	0.59811	11.13	7.66406	0.00903	0.00520	0.576	2.122
7	0.60194	10.79	7.57158	0.01018	0.00676	0.664	3.209
8	0.60536	10.46	7.54065	0.01112	0.00793	0.713	4.256
9	0.60855	10.09	8.25227	0.01180	0.00885	0.750	5.224
10	0.61150	9.68	8.27388	0.01226	0.00942	0.768	6.100
11	0.61434	9.20	8.44884	0.01248	0.00966	0.774	6.886
12	0.61716	8.66	8.49126	0.01244	0.00966	0.774	7.596

Table D.2: Details of the $1.5\,M_\odot$ model. The columns are the same as in Table D.1.

TP	M_H ($M_\odot$)	τ_{ip} (10^4 yr)	log ($L_{He}^{max}/L_\odot$)	ΔM_H ($M_\odot$)	ΔM_{DUP} ($M_\odot$)	λ	C/O
1	0.60032	...	6.47451	0.00244	...	...	0.290
2	0.60275	9.04	6.98190	0.00557	0.00117	0.210	0.374
3	0.60715	9.13	7.28519	0.00684	0.00336	0.491	0.769
4	0.61063	9.13	7.60773	0.00829	0.00565	0.682	1.488
5	0.61327	9.40	7.52308	0.00986	0.00779	0.790	2.404
6	0.61534	9.66	8.20353	0.01133	0.00958	0.846	3.366
7	0.61709	9.82	8.43709	0.01258	0.01108	0.881	4.305
8	0.61859	9.84	8.62304	0.01355	0.01219	0.900	5.191
9	0.61995	9.72	8.76118	0.01422	0.01293	0.909	6.013
10	0.62124	9.49	8.85653	0.01461	0.01339	0.916	6.767
11	0.62246	9.11	8.89618	0.01464	0.01331	0.909	7.445

Table D.3: Details of the $2\,M_\odot$ model. The columns are the same as in Table D.1.

TP	M_H ($M_\odot$)	τ_{ip} (10^4 yr)	log ($L_{He}^{max}/L_\odot$)	ΔM_H ($M_\odot$)	ΔM_{DUP} ($M_\odot$)	λ	C/O
1	0.71385	...	5.46870	0.00037	...	...	0.288
2	0.71421	2.51	6.57327	0.00279	0.00167	0.599	0.368
3	0.71533	2.99	7.11435	0.00401	0.00375	0.935	0.648
4	0.71559	3.47	7.65046	0.00553	0.00572	1.034	1.122
5	0.71540	3.98	8.13777	0.00708	0.00741	1.047	1.709
6	0.71507	4.41	8.56119	0.00850	0.00891	1.048	2.354
7	0.71466	4.78	8.50240	0.00979	0.01020	1.042	3.021
8	0.71425	5.11	9.22757	0.01101	0.01140	1.035	3.699
9	0.71386	5.28	9.43031	0.01183	0.01140	1.035	4.359

Table D.4: Details of the $3\,M_\odot$ model. The columns are the same as in Table D.1.

TP	M_H ($M_\odot$)	τ_{ip} (10^4 yr)	log ($L_{He}^{max}/L_\odot$)	ΔM_H ($M_\odot$)	ΔM_{DUP} ($M_\odot$)	λ	C/O
1	0.83004	...	5.04250	0.00162	...	...	0.302
2	0.83166	0.66	5.75606	0.00121	0.00042	0.347	0.306
3	0.83245	0.78	6.34611	0.00163	0.00138	0.847	0.368
4	0.83270	0.91	6.65654	0.00225	0.00231	1.027	0.508
5	0.83264	1.05	7.41039	0.00288	0.00309	1.073	0.711
6	0.83243	1.18	7.31972	0.00351	0.00385	1.097	0.943
7	0.83209	1.32	7.23935	0.00419	0.00451	1.076	0.980
8	0.83177	1.44	7.16595	0.00482	0.00512	1.062	0.733

Table D.5: Details of the $4\,M_\odot$ model. The columns are the same as in Table D.1.

TP	M_H ($M_\odot$)	τ_{ip} (10^4 yr)	log ($L_{He}^{max}/L_\odot$)	ΔM_H ($M_\odot$)	ΔM_{DUP} ($M_\odot$)	λ	C/O
1	0.90159	...	4.99690	0.00133	...	...	0.304
2	0.90292	0.30	5.48545	0.00079	0.00019	0.241	0.304
3	0.90352	0.33	5.93746	0.00097	0.00065	0.670	0.304
4	0.90384	0.36	6.40131	0.00123	0.00112	0.911	0.257
5	0.90395	0.40	6.48791	0.00152	0.00160	1.053	0.155
6	0.90387	0.48	6.56577	0.00191	0.00204	1.068	0.083
7	0.90374	0.56	6.67817	0.00232	0.00245	1.056	0.069
8	0.90361	0.64	6.68474	0.00267	0.00283	1.060	0.073
9	0.90345	0.71	6.69246	0.00302	0.00308	1.020	0.082
10	0.90339	0.76	6.69539	0.00325	0.00333	1.025	0.093
11	0.90331	0.80	6.68890	0.00347	0.00348	1.003	0.106
12	0.90330	0.82	6.69067	0.00357	0.00357	1.000	0.120
13	0.90330	0.83	6.69423	0.00361	0.00360	0.997	0.134
14	0.90331	0.83	6.69620	0.00362	0.00363	1.003	0.149

Table D.6: Details of the $5\,M_\odot$ model. The columns are the same as in Table D.1.

TP	M_H ($M_\odot$)	τ_{ip} (10^4 yr)	log ($L_{He}^{max}/L_\odot$)	ΔM_H ($M_\odot$)	ΔM_{DUP} ($M_\odot$)	λ	C/O
1	0.97297	...	4.48529	0.00041	...	...	0.282
2	0.97338	0.13	4.92864	0.00045	...	...	0.235
3	0.97383	0.14	5.20952	0.00050	0.00003	0.060	0.173
4	0.97430	0.15	5.54286	0.00056	0.00026	0.464	0.112
5	0.97460	0.16	5.91876	0.00066	0.00059	0.894	0.073
6	0.97467	0.20	6.40889	0.00087	0.00083	0.954	0.064
7	0.97471	0.20	6.36585	0.00107	0.00094	0.879	0.062

Table D.7: Details of the $6\,M_\odot$ model. The columns are the same as in Table D.1.